STRUCTURAL DESIGN AND ITS IMPACT ON THERMAL

EFFICIENCY AND CORROSION OF ALL ALUMINUM

MICROCHANNEL HEAT EXCHANGERS

Hossain Ahmed, B.S., M.S.

Dissertation Prepared for the Degree of

DOCTOR OF PHILOSOPHY

UNIVERSITY OF NORTH TEXAS

July 2023

APPROVED:

Seifollah Nasrazadani, Major Professor
Hamid Sadat, Co-Major Professor
Huseyin Bostanci, Committee Member
Xiaohua Li, Committee Member
Sundeep Mukherjee, Committee Member
Herman Shen, Chair of the Department of
    Mechanical Engineering
Paul S. Krueger, Dean of the College of
    Engineering
Victor Prybutok, Dean of the Toulouse
    Graduate School

Ahmed, Hossain. *Structural Design and Its Impact on Thermal Efficiency and Corrosion of All Aluminum Microchannel Heat Exchangers*. Doctor of Philosophy (Mechanical Engineering), July 2023, 82 pp., 8 tables, 45 figures, 119 numbered references.

In this study, high-fidelity conjugate heat transfer simulations are used to model a micro-channel heat exchanger (MCHE) in a crossflow to study its thermal-hydraulic performance. This study considers three different microchannels (internal flow) geometries (circular, triangular, and square) with louver-shaped fins. The local flow field showed a strong coupling between the microchannel flow, solid domain, and crossflow. The flow separation and wake regions formed near MCHE resulted in a large variation in the velocity field and temperature in the crossflow. The wake region had a significant spanwise variation due to its interaction with fins, which also causes variations in the thermal boundary layer. The heat conduction in the solid structure provided a non-uniform temperature field with a higher temperature near the microchannel and a slightly lower temperature near the surface exposed to the crossflow. The microchannel flow analysis showed that the internal geometry affects the pressure drop, which is highest for the triangular MCHE and lowest for the circular MCHE. However, the microchannel flow temperature change was relatively similar for all microchannels. Results showed that for the same volume of the microchannel, the circular shape microchannel has a higher performance index value than the triangular and square shapes. This study also considers three different fin (external flow/crossflow) geometries (louver, step, and saw) with the same tube and circular shape microchannel and identifies the corrosion hot spot. Crossflow shows higher temperatures near the boundary layer of the tube, which results in higher corrosion rates. A predicted flow field also identifies crevices between fins and tube surfaces as critical corrosion hot spots often associated with low-velocity regions. Electrochemical impedance spectroscopy (EIS) analysis was done on AA3102 (Alloy used in the circular channel and louver fin) alloy in corrosive environments containing low and high

concentrations of the combination of sodium chloride and ammonium sulfate. Electrolytes used in this research have pH values ranging from 4.0 to 5.8, closer to nearly neutral environments encountered in many atmospheres. EIS results are presented, including Rsol, Rpore, and Rct of AA3102 with very thin arc evaporated porous Zinc film on AA 3102 along with their equivalent circuit.

ACKNOWLEDGMENT

TABLE OF CONTENTS

LIST OF TABLES

LIST OF FIGURES

CHAPTER 1

INTRODUCTION

Micro-channel heat exchangers have attracted much attention during the late twentieth century. The main reason is the possibility of reducing the heat exchangers' size, weight, and cost compared to the round copper tube and plate-fin (RTPF) heat exchangers. Also, new applications where objects of small size need to be cooled, such as electronics or micro-mechanical devices, require heat exchangers with miniature channels. Microchannel heat sinks were developed in 1980 to solve the problem of high heat dissipation in semiconductor chips that limited high-performance computing. Later, microchannel heat exchangers (MCHEs) began to get more and more attention from scholars and researchers in various industries, for example, automobile, aerospace, power generation, and chemical processing. For decades, round copper tube and plate-fin (RTPF) heat exchangers have been widely used in automobiles and HVAC systems. This heat exchanger has a header plate, copper tubes, and aluminum fins. The header plates on two ends of the heat exchanger are galvanized steel attached to copper tubes stacked on the aluminum fins. According to a survey from SAPA, the price range of copper in USD/ton from 1998 to 2008 is shown to have increased significantly, almost thrice as much as aluminum. The need for more efficient heat exchangers, with lighter weight and lower cost, has been the primary concern in automotive and HVAC&R. In automobile industries, lightweight heat exchangers are desired.

1.1   Microchannels

Microchannels can be fabricated using various tools and processes, including surface micromachining, bulk micromachining, molding, embossing, laser techniques, and conventional machining micro-cutters. Silicon or aluminum-based microchannels of different cross-sections in microsystems such as micro-heat sinks, micro-biochips, micro-reactors, and micro-nozzles. Many studies have focused on transport phenomena in microchannels, e.g., [1–

5]. Microchannels are also used as gas delivery systems and heat exchangers in fuel cell technologies. Microchannels offer high surface area per volume ratios, high heat transfer coefficients, and low thermal resistance [6].

Typically, microchannels can be defined as channels whose dimensions are less than 1mm and greater than 1μm. Above 1mm, the flow exhibits the same behavior as macroscopic flow. Below 1μm, the flow is characterized as nanoscopic. Nowadays, most microchannels fall into the range of 40μm to 400μm.

1.2   All Aluminum Heat Exchanger

All aluminum heat exchangers have been used in the HVAC and automobile industry for balanced, comprehensive weldability, lightweight, mechanical properties, formability, low refrigerant charge, competitive raw material costs, and general corrosion resistance; 3000 series aluminum alloys are the structural materials of choice. All aluminum heat exchanger materials were used intentionally to resolve galvanic corrosion in conventional round tube-fin heat exchangers using dissimilar metals. It is worth mentioning that respective diversities of designated 3000 series aluminum alloys for the combination of multiple ports extruded (MPE) tubes, high frequency (HF) welded headers, and louvered fins are expected to follow the desired sequence of chemical reactivity for each component, thereby optimizing corrosion resistance. In addition, the brazed assembly technique is used to manufacture microchannel heat exchangers where the contact between the tubes and fins of a traditional fined tube heat exchanger is mechanical.

In contrast, the microchannel heat exchanger's manufacture involves brazing, which provides the metallurgical bond between tubes and fins, eliminates contact resistance, and ensures higher heat transfer. Micro heat exchangers that benefit from their high surface area to volume ratios will play an essential role in many fields where thermal issues are becoming a more critical problem to deal with than in the past. The primary benefit of using MCHEs in

2

HVAC is efficiency. Many smaller tubes provide more surface area for refrigerant-to-wall contact than larger tubes in the same space. A larger surface area improves heat transfer efficiency, with some manufacturers asserting an improvement of 20 to 40% over the traditional fin and tube heat exchangers.

In Figure 1.1, controlled atmosphere brazing (CAB) technology is used to blaze the tube and fin at the aluminum heat exchangers. For aluminum MCHE brazing, the oxide film on all aluminum surfaces must be primarily demolished to permit the free flow of molten clad in brazing. The CAB method is completed for controlled surroundings by accumulating flux on an aluminum surface to be joined [7].
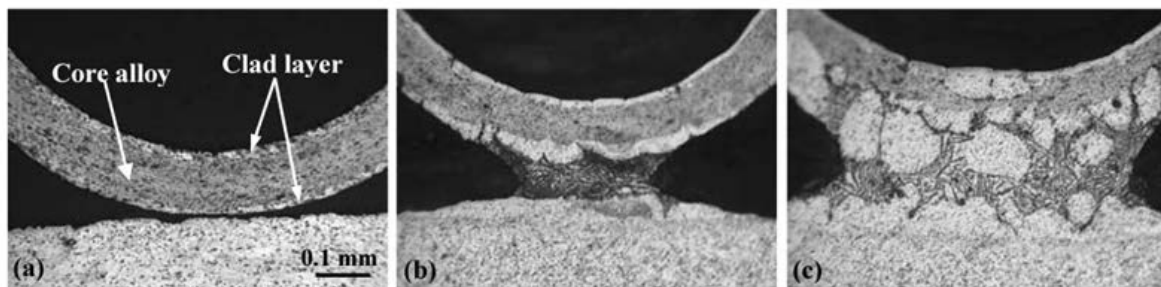
Figure 1.1: CAB brazed joint between fin and tube (a) Fin and tube before brazing; (b) and (c) after brazing [8]

The advantages of using all-aluminum microchannels in heat exchanger systems include increased equipment efficiency, decreased weight and size, and lower system end-cost. The most intensive heat transfer between refrigerants and tubes happens along the tube walls, with less heat transfer in the refrigerant flow center. In single-phase heat transfer, the critical role is played by tube diameter: the smaller the diameter, the greater the heat transfer coefficient. On the other hand, the refrigerant flow regime produces the most significant heat transfer ratio effect in two-phase heat transfer. Microchannel heat exchanger's heat transfer performance is excessive in single-phase heat transfer and two-phase heat transfer, considering that microchannel tubes have a smaller diameter than the finned tube heat exchanger's copper tubes, and the surface tension results in stratified flow in the microchannel.

The louvered plate's fins are periodically folded and bonded to the flat microchannel tube's surface. The geometry of louvered fins guarantees a heat transfer coefficient 50% higher than the rectangular fins required to construct finned tube heat exchangers. Louvered fins also reduce airflow turbulence and minimize air shadows. Louvered fins produce lower airside pressure drops when merged with flat, streamlined microchannel tubes with low-pressure drag. This study studies the effect of the channels' shape on their performance for different channel cross-sections, such as circular, rectangular, and triangular.

1.3   Conjugate Heat Transfer

The Conjugate Heat Transfer analysis type allows heat transfer model between fluid and solid domains by exchanging thermal energy at the boundaries between them. Heat transfer in heat exchangers mainly occurs along the walls via conduction, and the center of the fluid takes longer to release the heat via convection. As a result, convection plays less of a role in transporting the heat. A more significant percentage of the refrigerant is in contact with the sides to transfer heat, and the same degree of heat transfer consumes less refrigerant [9].

In a conventional heat exchanger, the solid thickness is small compared to the hydraulic diameter; therefore, a one-dimensional assumption may be a good approximation. This means the heat exchanger's performance primarily depends on the flow in the ducts, such as fluid properties and mass flow rate. However, the solid thickness of the microchannel heat exchanger is larger than the hydraulic diameter. Therefore, the conduction in the solid is essential, and a one-dimensional assumption will not be satisfied for a practical microchannel heat exchanger. In that exchanger, the axial conduction may play an important role.

Furthermore, the microchannel heat exchanger's effectiveness may decrease because of axial conduction, which increases the solid's thermal conductivity. This requires the solution of the three-dimensional equations in both solid and fluid [9]. Despite the thermal performance enhancement of MCHEs, corrosion of both tune and fin materials made of Aluminum 3xxx

4

series has remained a concern. The following section addresses the corrosion mechanism of Aluminum alloys used in MCHEs.

1.4   Corrosion Mechanisms of Aluminum Alloys

The oxide film on aluminum alloys has defects in real life because the underlying microstructure is diverse. These defects occupy places close to the grain boundaries and intermetallic particles. The oxide film can disintegrate in those weak areas, making it easier for localized corrosion to develop. The most common localized corrosion types on aluminum alloy surfaces are intergranular, exfoliation, pitting, and crevice [10-11].

Generally, localized corrosion consists of these steps in chronology: i) Reactive species adsorb onto the aluminum oxide film, ii) the adsorbed species participate in a chemical reaction with precipitated aluminum hydroxide, $Al(OH)_3$ or aluminum ions, iii) dissolution resulting in a thinner oxide film and penetration of reactive species into the oxide film, and iv) pitting propagation which consists of reactive species directly attacking the aluminum. In the second step, also called the competitive process, aggressive species like chloride ions compete with water molecules or hydroxyl ions to adsorb onto the aluminum surface. The surface would become less active if the aggressive species lost the adsorption competition [12]. Pitting corrosion occurs when holes from localized corrosion attack. This takes place when the passive oxide layer disintegrates. The first step of pitting corrosion is passivity breakdown (pitting initiation), which includes three mechanisms: i) adsorption and mechanisms which are adsorption-induced in which corrosive species, such as chloride ions, actively try to settle on the positions of the hydroxyl groups on the surface, ii) ions move across the metal-oxide interface, iii) the aggressive species break down the film and replace the preexisting ions, resulting in a new film containing the aggressive ions [10-11] [13-15]. After pitting initiation, propagation occurs, which means the pit grows autocatalytically. Cavities are formed on the metal surface from the autocatalytic reaction. [16] The pitting potential, E_{pit} is a measure of the

propensity for pitting to occur, and from Figure 1.2, having a lesser amount of chloride ions results in increasing E_{pit}. This means more resistance against pitting corrosion. The higher the difference between the corrosion potential, Ecor, and Epit, the higher the pitting corrosion resistance [10][17].
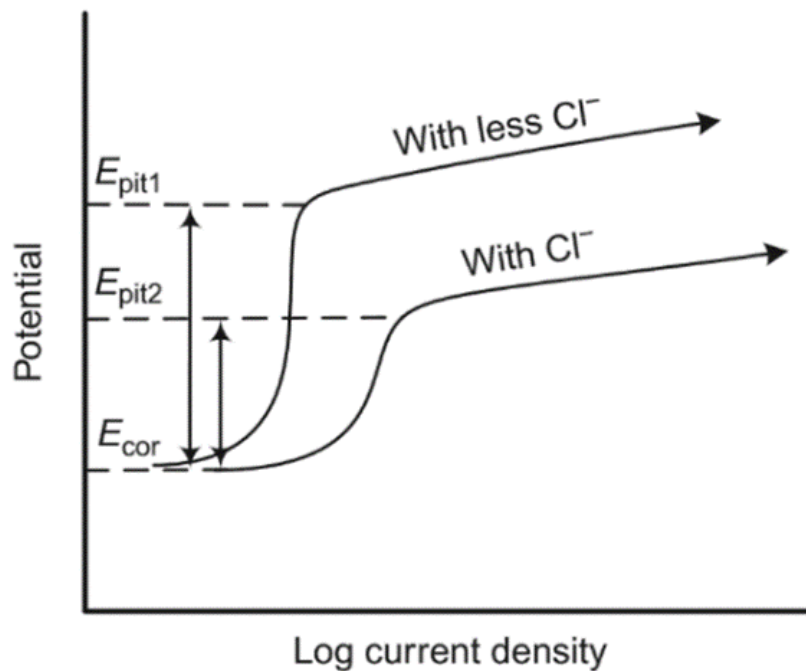
Figure 1.2: Examples of an anodic polarization curve and how the concentration of Cl- affects Epit.[10].

The reactions occurring at the anodic and cathodic sites are shown below [8].
(1) $Al \rightarrow Al^{3+} + 3e^-$

(2) $2H_2O + O_{2(aq)} + 4e^- \rightarrow 4OH^-$

(3) $2H^+ + 2e^- \rightarrow H_2$

(4) $Al^{3+} + 3Cl^- + 3H_2O \rightarrow Al(OH)_3 + 3HCl$
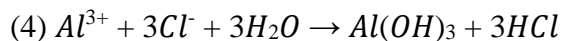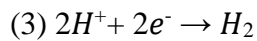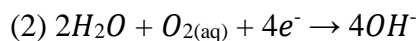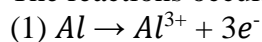
At the pit, reaction 4 shows that hydrochloric acid, HCl, is formed due to Al^{3+} reacting with H_2O, which makes the solution acidic. [10] Precipitation of $Al(OH)_3$ takes place, and the reduction of hydrogen cations makes microbubbles that will bring the $Al(OH)_3$ to the top of the pit. This will result in deposits that can be seen as white bumps. The corrosion products will accumulate at the pit's opening and prevent chloride ions from moving into the pits, thus reducing the pitting rate and even stopping it completely [18].

6

Crevice corrosion occurs in crevices, the confined parts of metal that consist of an electrolyte, like a gap. Another type of localized corrosion occurs due to similar chemical reactions, and this is called pitting corrosion [18]. Pitting corrosion is one of the most challenging forms of corrosion to manage reliably. Chloride is the most encountered aggressive agent, as it causes the pitting of many metals [19-20]. A significant engineering design feature of many structures and components is the resistance to pitting corrosion. Despite this and the wealth of knowledge in this area, chloride-induced pitting remains a primary form of failure. Many variables are involved in this phenomenon; almost every metal or environment system feature affects pitting. For example, the phenomenon of the chloride-induced pitting of many metals is well known, and it is naturally a function of the chloride concentration and the temperature. It is distinct from the metal's identity, composition, and microstructural characteristics. However, in addition to the chloride concentration, the presence of most other components of the environment also affects the pitting characteristics. Even ions with no noticeable chemical effect in the system can have a marked impact on pitting [21-23]. One consequence of the sensitivity to the many variables is the difficulty in classifying a metal's actual susceptibility or resistance to pitting. Moreover, to define the pitting characteristics, one needs to specify every possible component and feature of the system; if this is not done, it stands to reason that it will not be reproducible. In chloride solutions, pitting is often characterized by its so-called pitting potential and sometimes by its related passivation or protection potential. A wealth of literature on these characteristic potentials is essential to pitting knowledge. However, in terms of chloride solution, the pits can and do nucleate and even grow at potentials below the conventional pitting potential [24-31]. The pitting potential, which is often used to characterize the pitting of metals and alloys, does not mark the boundary between pitting and a lack of pitting. Aluminum alloys are susceptible to localized corrosion; as such, these alloys are typically protected with a coating system to provide them with barrier

protection from aggressive environments. However, aluminum alloys are susceptible to localized corrosion in crevices mainly because of their intermetallic particles that may have vastly different electrochemical behaviors than the aluminum matrix [32-35]. Coatings can be employed on the surface to protect the metal from the harsh environment. However, these coatings do not increase mechanical strength; rather, they isolate the material from the corrosive electrolyte [36]. These coatings are usually categorized into metallic, organic, and inorganic coatings. Chromate conversion coatings (CCC) are also used in aluminum alloys for protection. Utilizing coatings is a relatively simple application with a low cost that provides benefits to corrosion resistance, so it is used for various applications [37-40]. The formation of CCC and the mechanisms by which they protect aluminum alloys contribute significantly to their overall effectiveness as a surface pretreatment. This pretreatment is typically employed in an acid and chromium (VI) ion bath. The subsequent protective coating has two distinct layers; an outer layer that is thick and porous and a barrier layer that lies between the coating and the underlying metal surface [37]. Campestrini et al.,[40] recommended a three-stage formation process. Initially, there is the passive layer. Here, the aluminum surface is activated by thinning the original aluminum oxide, allowing the dissolution of aluminum to appear across the interface. Following the activation of the aluminum surface, chromium reduction begins to occur. This leads to the saturation of the solution with trivalent chromium. As supersaturation occurs, chromium oxide begins to deposit on the surface. The ultimate step consists of covering the entire surface with chromium (III) hydroxide and the layer growing. At this point, the surface becomes covered with spherical particles of chromium oxide; however, the porosity of the layer lets the subsequent processes continue, which results in the thickening of the chromate layer. Metallic coatings can be used as a substrate in numerous ways, such as hot dipping, electroplating, spraying, cementation, and diffusion [40]. The type of coating process one chooses depends on several factors, including the essential corrosion resistance and the

8

anticipated lifetime of the coating. On substrates made of alternative materials, coatings employed are often nickel, zinc, lead, tin, aluminum, cadmium, and chromium [41]. Paints, lacquers, resins, and plastic linings are all organic coatings [42]. They usually have a high impermeability and they have an inhibitive function to the corrosion process; moreover, they can also contain catholically protective pigments. Each coating can be used in heat exchangers to protect the heat transfer surface from corrosive conditions [43-45].

Furthermore, coatings can also play a different role in protecting from corrosion. Wang et al. tested hydrophilic coatings being used to increase condensation draining in fin-and-tube heat exchangers [46]. With better draining, this could reduce the pressure drop by up to 40%. In addition, in dehumidifying heat exchangers, hydrophilic coatings have effectively been utilized [47]. Intergranular corrosion occurs around the grain boundary of a metal and its alloys; it arises when the crystal and its grain do not experience evident destruction. This dramatically weakens the mechanical properties of a metal and its alloy [48]. In electrochemistry, the difference in the microstructure grain boundary between aluminum and its alloys will result in potential electrochemical formation and electron exchange [49]. Intergranular corrosion starts as a result of pitting corrosion, and it spreads fast along the grain boundary. When the grain boundary of the metal and its alloy become active, intergranular corrosion may occur. The condition includes increasing or decreasing the elements of the metal alloys near their grain boundaries. In turn, the grain boundary needs an electronegative area. The electronegative area will corrode first [50]. An example of intergranular corrosion is putting a high-purity aluminum alloy in a strongly acidic environment or a high-temperature water, including Al-Mg, Al-Cu, and Al-Zn-Mg.

Figure 1.3 illustrates intergranular cracks of aluminum tubes [51]. Beginning in the mid-20th century, intergranular corrosion drew more attention from researchers. Three major theories of intergranular corrosion were devised.

1) The electrochemical potential formation between the alloy crystalline lattice and the anodic grain boundary results in galvanic corrosion, leading to further intergranular corrosion [52].

2) The difference in breakdown potential between the grain boundary and the solute atom depletion zones (SDZ) may cause intergranular corrosion [53].

3) When the precipitated phase is dissolved at the grain boundary, it forms an occluded environment, which results in intergranular corrosion [54-55].
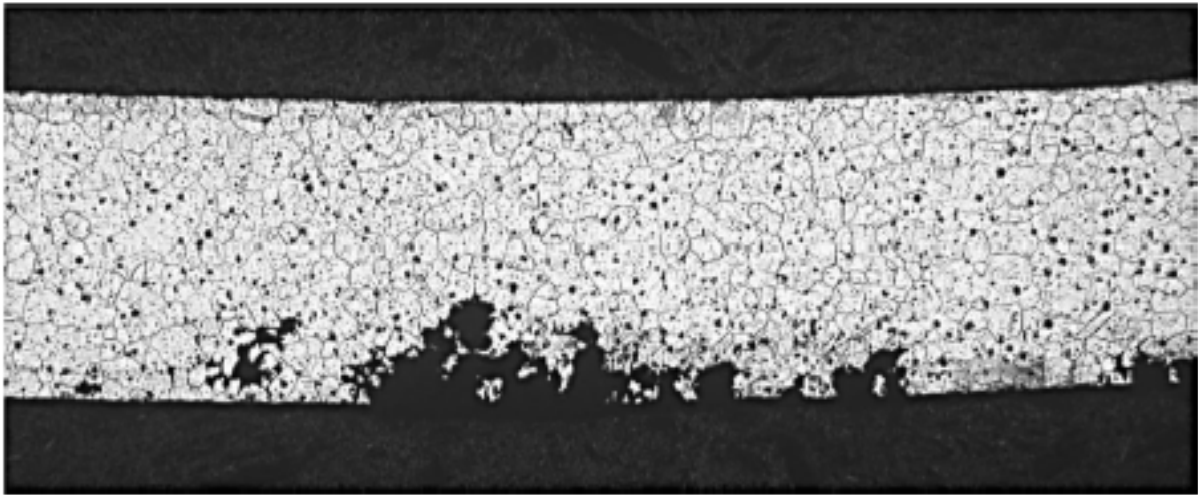
Figure 1.3: Intergranular corrosion of an aluminum tube.[51]

Since this time, most of the research about intergranular corrosion has been based on one or more of the above theories. To investigate the grain boundary precipitation phase, one must use the galvanic coupling method. This forms a galvanic couple between pure aluminum and the grain boundary precipitation compositions [54-55]. Subsequently, it determines the polarization curves and compares the current corrosion magnitude. Investigating the breakdown potential between the SDZ and lattice allows researchers to determine the corrosion mode at different potentials using polarization curves [53].

In 1970, Hedrick found that aluminum alloys are more likely to experience microbiologically induced corrosion under the bacteria environment [56]. In [57], Giacobone investigated the corrosion behavior of aluminum 6061 alloys under the Bacillus cereus RE 10 environments. He stated that pitting corrosion was detected on the Al 6061 alloy. In contrast, pure aluminum does not corrode. The researcher concluded that the alloy surface's biological

membrane formation provides the environment for pitting corrosion [57]. In the literature, most studies proved that the existence of microorganisms (bacteria and fungi) accelerated the corrosion of aluminum alloys, especially local corrosion, which includes pitting and galvanic corrosion. [58-60].

1.5   The Objective of This Study

Many authors have investigated circular and non-circular microchannels, such as rectangular, trapezoidal, elliptical, and triangular, to identify the heat transfer characteristics. They used different methods to obtain these microchannel's hydrodynamics and heat transfer characteristics. All these works aim to get the best applicable microchannel geometry, which means a high heat transfer rate and a low-pressure drop.

However, there is nearly negligible numerical research concerning the environmental air domain. On the other hand, the available results concern that the exchanger's flow and heat transfer characteristics are not evident. Therefore, the 3D model with air and water fluid flow along with heat transfer domains has been used, as it provides more precise results than models that assume constant temperatures or heat fluxes on the tube walls. Furthermore, the developed model comprised the heat exchanger's full air and water flow. Therefore, this work is aimed to investigate the below main points:

(a) Obtain a numerical model for internal hydrodynamics and heat transfer in circular, triangular, and rectangular microchannel heat exchangers by solving the continuity, momentum, and energy equations and finding the optimum result considering the environmental air or crossflow domain.

(b) This study considers three different fin geometries (louver, step, and saw) with the same tube and circular shape microchannel and identifies the corrosion hot spot and thermal effectiveness.

(c) Analysis of fin tube geometry impact on the potential localized form of corrosion (pitting and crevice). Electrochemical testing (AC impedance and Potentiodynamic) on AA 3102 in simulated industrial and marine atmosphere.

1.6   Dissertation Layout

The remaining dissertation is organized as follows. Chapter 2 presents a literature review of MCHE for numerical simulation and an EIS test. Chapter 3 presents the experimental methods for the electrochemical testing method. Chapter 4 exhibits the initial setup for the numerical simulation. Chapter 5 presents the experimental results of the EIS experiment. Chapter 6 contains thermal and hydraulic performance evaluation simulation results for different microchannel geometry and fin geometry. Finally, a summary and future outlook will be presented in Chapter 7.

CHAPTER 2

LITERATURE REVIEW

In recent years, the research in the field of thermal-hydraulic at the micro-scale level has been increased constantly due to the rapid growth of technology applications required to transfer high heat rates in relatively small spaces and volumes—the present work studying the problem of impact on thermal efficiency in MCHE. As a result, many researchers in the literature studied parameters affecting the performance of MCHE, including thermal efficiency. Below is a review of most related papers.

Jiang et al. [61] experimentally studied the fluid flow and forced convection heat transfer in the rectangular MCHE for two different channel heights. They exhibited that the pressure drop in the MCHE with deep channels (large height) for the same flow rate is much lower than in the exchanger with shallow channels (small height). Also, they concluded that the MCHE with deep channels has the best overall thermal-hydraulic performance. Al-bakhit and Fakheri [62] determined that the complete numerical solution of the microchannel heat exchangers is computationally unaffordable because the flow and temperature fields must be simultaneously resolved in the two fluids and the solid. The researchers proposed a hybrid approach in which the nonlinear momentum equations for one or two channels are solved by using a commercially available CFD (computational fluid dynamics) code. The velocity field is used in a user-developed code for solving the linear energy equations for the entire heat exchanger. Al-bakhit and Fakheri [63] investigated the parallel flow MCHEs performances with rectangular ducts. They found that the overall heat transfer coefficient is rapidly changed for the entrance region of the duct where Graetz number is less than 0.03; therefore, the constant overall heat transfer coefficient assumption is not always valid. Brandner et al. [64] studied various microstructure crossflow heat exchangers and compared their thermal performances. They found that heat transfer in the micro heat exchanger can be improved by decreasing the

hydraulic diameter of microchannels. They also fabricated heat exchangers with two distinct layouts of microcolumn arrays (aligned and staggered). They showed that the array of microcolumns can maximize heat transfer while minimizing the pressure drop across the heat exchanger. Hasan et al. [65] numerically investigated the hydrodynamics and thermal behaviors of the laminar, 3-D, fully-developed flow for different geometrical shapes of MCHE. They showed that at a lower Reynolds number (Re), a circular-shaped channel is the most effective. In turn, at a higher Re, triangular channels are the most effective, followed by trapezoidal and then circular. This occurs because of the entrance region, which is longer in a triangle and trapezoid than it is in a circular channel. A relationship has been shown between the effect of an increased entrance region and an increase in the Reynolds numbers. Usually, the effectiveness decreases when the Re decreases due to an increase in flow velocity and, at the same time, a decrease in the residence time inside the microchannel. Glazar et al. [66] showed that the thermodynamical and hydrodynamical investigation of compact heat exchangers with different microchannel shapes had been achieved concerning the heat transfer effectiveness and pressure drop. Results exposed that heat transfer effectiveness decreases with the rise of inlet air velocity. The best achievements about the same parameters were accomplished with microchannels of diamond and hexagonal shapes. Although higher heat transfer effectiveness of mentioned shapes, the best performance is achieved by rectangular shape according to water side pressure drop. Glazar et al., [67] showed multivariate optimization of the air-water heat exchanger with a microchannel coil. Optimization included four geometry parameters that were used to develop several new objective functions. Fin pitch, microchannel flat-tube transversal row pitch, number of small channels, and partition wall thickness were set as variable geometry parameters. Numerical simulations were performed using fluid flow and heat transfer solver FLUENT. The SIMPLE algorithm was used for pressure-velocity coupling to ensure mass conservation and obtain a pressure field. By using

optimal geometry values, the performance of MCHX can be improved. Though aluminum alloys are passive and use all the aluminum to resist galvanic corrosion, there are reports of MCHE systems corrosion [68-75]. Most heat exchanger failures occur because of the hostile atmospheres in which the heat exchangers operate. For example, crevice corrosion occurs due to salt discharge and fouling [68]. Yoshino et al. [76] examined intergranular corrosion (IGS) because of the contact of the fin with the microstructure and chemical composition. The area prone to crevice corrosion accumulates deposits; in turn, dust holds wetness for extended periods, leading to increased wetness. The area between the fin and tube is most vulnerable to crevice corrosion due to a lack of fluid flow or very low fluid velocities. Stagnant areas contain corrosive salts and other contaminants that form pits of various sizes and, ultimately, perforated tubes. A localized form of corrosion in heat exchangers was observed by Faes et al., [75]. Aluminum alloys form a protective film that is typically vulnerable to pitting [77]. Pits start because there is surface damage to the protective layers. These pits become more prominent over time and perforate the heat exchanger tube. This pitting is initiated due to the presence of corrosion products in the atmosphere. For example, chloride content, excessive temperatures, and lower pH values can lead to pitting corrosion.

During the construction phase of MCHE, the metal protective film is sometimes damaged locally, and this initiate pitting [78]. Crevice corrosion is also localized corrosion caused by a local environment different from the bulk environment. For example, oxygen exhaustion can occur in crevices or shielded areas where stagnation occurs. This variance in concentration of oxygen influences the induction of crevice corrosion.

Despite many studies of MCHE systems in the past, most investigations focused on the thermal performance of MCHEs but ignored corrosion aspects based on the local flow pattern. This study shows that the corroded crevice area or corrosion hot spot due to zero velocity conditions exists near the fin and solid junction. Furthermore, this study consists of three fin

geometries (louver, step, and saw) with circular MCHE. A predicted flow field is also used to identify corrosion hot spots, often associated with low-velocity regions where materials degradation due to crevice corrosion is likely to cause pitting, followed by perforation and eventual leaking of MCHEs.

Several tests and standards have been created for the corrosion testing of metals. Cabinet tests are one of the oldest techniques used since the 1900s to evaluate coatings against corrosion. They were also used as means for performing accelerated corrosion testing. As the name suggests, these tests are performed in a chamber or cabinet, where a corrosive environment is simulated. Typical corrosive environments produced in a test chamber are salt fog, humidity, hot and cold temperatures, ultraviolet exposure, and corrosive gases. These environments may be used independently or in combination with each other. With technology, these tests have evolved from homemade cabinets that operated at fixed temperatures and humidity to complex computer-controlled tests with varying service conditions. There have also been advancements in the size of the cabinets to accommodate various samples. They have evolved from bench-top cabinets to walk-in and drive-in chambers [79-80].

Salt-Spray (FOG) Tests are the most common type of cabinet test. This procedure exposes the samples to a fog produced by air-atomizing sodium chloride solution while controlling the cabinet temperature. Salt-spray tests have widespread use in many industries, including but not limited to automotive, aerospace, paints, and coatings. These tests can be performed as standalone tests or in conjunction with others. The duration of these tests can be up to 5000 hours, during which the chamber must be closed, except for events when samples need to be rotated or visually inspected.

The results of the FOG tests are usually interpreted based on visual inspection of the failure of the coatings or the total mass loss of the sample. Not infrequently, such tests have been misapplied and misused. Sometimes there is no clear correlation between salt-spray tests

and failures in the natural environment. Strictly, these tests cannot be used as quantitative indicators of corrosion but can help control the quality of a coating process. After a sample is prepared, it is exposed to a FOG chamber, and if the sample does not survive a certain number of hours in the chamber, it can indicate that the coating process of the sample might not have been appropriately done [81-82].

The standard FOG tests have other variations designed for different materials. For example, certain aluminum alloys develop surface blisters when exposed to marine atmospheres, followed by metal delamination: exfoliation. Cyclic acidified salt-fog tests are used for exfoliation testing. In these experiments, 5% sodium chloride solutions are utilized, adjusted to pH values between 2.8 and 3.0 with acetic acid. Another variation of this test is the acidified synthetic-seawater (FOG) test. Instead of a 5% sodium chloride solution, a synthetic seawater solution with pH adjusted to values between 2.8 and 3 is used. Many other variations of the FOG tests exist, often applicable to materials other than aluminum [79].

Humidity tests are categorized into controlled humidity tests that target a specific relative humidity or high humidity tests conducted at high humidity ranges, typically over 95%. In the humidity range of 70% to 95%, filiform corrosion, identified by thread-like strands, is formed under finishes such as clear-coated aluminum powder. Therefore, testing for filiform corrosion is initiated with salt spray exposure for six hours, followed by 70-90% humidity exposure. Visual observations are used to evaluate all the tests above [79].

All aluminum microchannel heat exchangers take advantage of cathodic protection using a sacrificial anode to protect them. Aluminum tubes and fins are protected by using a thin zinc-based coating as a sacrificial layer to protect the aluminum substrates [83]. Zinc is anodic to aluminum on the galvanic series; as a result, zinc becomes the anode that scarifies itself. In turn, the aluminum substrate becomes the cathode that is protected [84-85]. Long-term atmosphere exposures and accelerated corrosion tests are widely used to assess different

zinc coatings' corrosion resistance [86-88]. However, compared with accelerated corrosion tests, performing long-term atmosphere exposures is time-consuming and region dependent. As such, this method is unfavorable for applying and promoting new coatings.

In contrast, electrochemical methods, particularly the electrochemical impedance spectroscopy (EIS) technique, is an efficient and convincing tool used for analyzing the corrosion behavior of metals. [89-90]. Aqueous corrosion is an electrochemical process that can be tracked using electronic devices (potentiostat); it applies an electrical signal to measure and control the electrical charge transfer. When the evaluation is fulfilled, the reaction kinetics and the mechanism of the corrosion procedure take place at the metal interface. The electrochemistry impedance is the correlation between a potential energy distinction and the flow of electrons constructed by a wave signal applied in an aqueous media. EIS was used to assess the properties of thin oxide films developed on metals, monitoring superficial degradation of coatings due to the swelling process. Surface changes caused by ion adsorption at the interface can also be recognized by knowing the kinetics reaction on metals under the corrosion process. In addition, electrochemical techniques can provide facts on the reactions and mechanisms of electrochemical deterioration.

This chapter reviewed analytical, experimental, and numerical studies in the microchannels field. These studies showed that the main advantage of microchannels is their high heat transfer rate because of their small hydraulic diameters. On the other hand, the studies indicated that pressure drop is high in these channels for the same reason. Therefore, many researchers investigate the flow and heat transfer characteristics in different microchannels geometries to obtain the best applicable geometry (high heat transfer rate and low-pressure drop). One of the numerical analyses shortcomings of the aforementioned studies is that none considered the effect of environmental airflow. Glazar et al., [67] numerically analyzed the optimization of an MCHE considering the environmental airflow. Optimization included four

geometry parameters: fin pitch, microchannel flat-tube transversal row pitch, number of microchannels, and partition wall thickness. Results showed the geometry with optimal values improves the performance of MCHE. Although the environmental airflow was considered by Glazer et al., the focus of the study was laid more on optimization. Hence fin shapes were simplified. In this study, high-fidelity conjugate heat transfer simulations are used to study the thermal-hydraulic performance of a MCHE with louver-shaped fins in a crossflow. This study considers three MHCEs with different microchannel geometries (circular, triangular, and square). This study shows that the corroded crevice area or corrosion hot spot due to zero velocity conditions exists near the fin and solid junction. Furthermore, this study consists of three fin geometries (louver, step, and saw) with circular MCHE. A predicted flow field is also used to identify corrosion hot spots, often associated with low-velocity regions where materials degradation due to crevice corrosion is likely to cause pitting, followed by perforation and eventual leaking of MCHEs. The developed numerical model for the microchannel heat exchanger is presented in chapter five for different geometries. Furthermore, this work aimed to study the corrosion resistance of the Al-3102 MCHE tube. The result of the experimental work for the EIS test is presented in chapter four for MCHE tubes in different chloride and sulfate concentrate electrolyte.

CHAPTER 3

EXPERIMENTAL METHOD

EIS involves the application of a small, sinusoidal, alternating current (AC) or voltage to the sample undergoing investigation. The AC perturbation (either voltage or current) is applied over a range of frequencies, and the electrical response of the system is measured and studied over this range of frequencies [91]; an EIS setup consists of a working electrode (WE), a counter electrode (CE), and a reference electrode (RE). The working electrode, generally the material under investigation, is where the corrosion reaction(s) occurs in an electrochemical system. The counter or auxiliary electrode in the cell provides the primary current source, and the reference electrode serves as an experimental voltage reference point.

3.1 Concept and Representations of EIS

In an electrochemical cell, the interactions between electrodes and redox species include the concentration of electroactive species, charge transfer, and mass transfer from the bulk solution to the electrode surface. Each feature is characterized by an electrical circuit consisting of resistances, capacitors, or constant phase elements connected in parallel or series to form an equivalent circuit. Thus, the EIS could explore mass transfer, charge transfer, and diffusion processes. Accordingly, the EIS can study intrinsic material properties or specific processes that could influence an electrochemical system's conductance, resistance, or capacitance. Electrochemical impedance spectroscopy (EIS) is a small signal electrochemical method that makes the response pseudo-linear. The applied electrochemical perturbation is small, around 10 mV. So, due to the measurement, the damage is insignificant. As a result, the electrochemical cell response is pseudo-linear, acquiring a phase shift, while the current response to a sinusoidal potential is a sinusoid at the applied frequency. Thus, the excitation signal is displayed as a function of time, as shown in Equation (3.1):

$$E_t = E_0 \sin(\omega t) \tag{3.1}$$

where E_0 is the amplitude of the signal, E_t is the potential at time t, and ω is the radial frequency. The correlation between the radial frequency (ω) and the applied frequency (f) is calculated by Equation (3.2):

$$\omega = 2\pi f \tag{3.2}$$

In a linear system, the signal is shifted in phase (φ) and has a different amplitude than I_0 (Equation (3.3).

$$I_t = I_0 \sin(\omega t + \varphi) \tag{3.3}$$

Thus, the impedance of the complete system can be obtained from Equation (3.4):

$$Z = \frac{E}{I} = Z_0(\cos(\varphi) + j\sin(\varphi)) \tag{3.4}$$

where E, Z, I, ω and φ, are potential, impedance, current, frequency, and phase shift among E and I, respectively. The impedance is conveyed in terms of a magnitude, Z_0, and a phase shift, φ. If the operated sinusoidal signal is plotted on the X-axis and the sinusoidal response signal on the Y-axis, the result is a "Lissajous Plot".
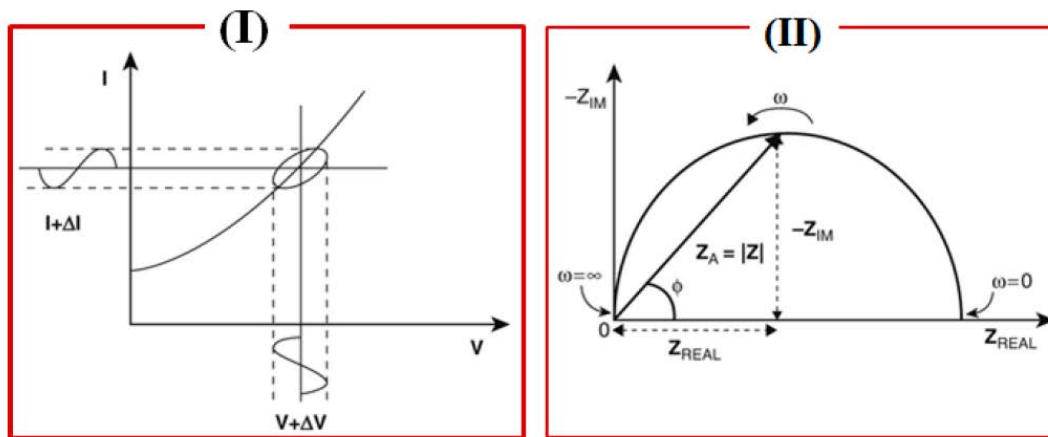
Figure 3.1: The Lissajous plot (I) and the Nyquist plot with impedance vector (II). Source: Figure modified from [92], electrochemical impedance spectroscopy (EIS) applications to sensors and diagnostics. [93]

The impedance expression is split into a real part and an imaginary part. When the real part (Z_{real}) is plotted on the X-coordinate and the imaginary part is plotted on the Y-coordinate to form the "Nyquist Plot" showed in Figure 3.1(II). Each point on the Nyquist plot is an

impedance evaluate at a frequency point, while the Z_{img} is negative. On the real axis or X axis, the impedance is accompanied by low frequency, whereas the higher frequencies are applied on the left. In Figure 3-1, the angle between the arrow and the X-coordinate is called the "phase angle". Another way to convey the impedance results is to use a Bode plot, where the Bode plot contains two separate logarithmic plots: magnitude vs. frequency and phase vs. frequency (Figure 3.2).
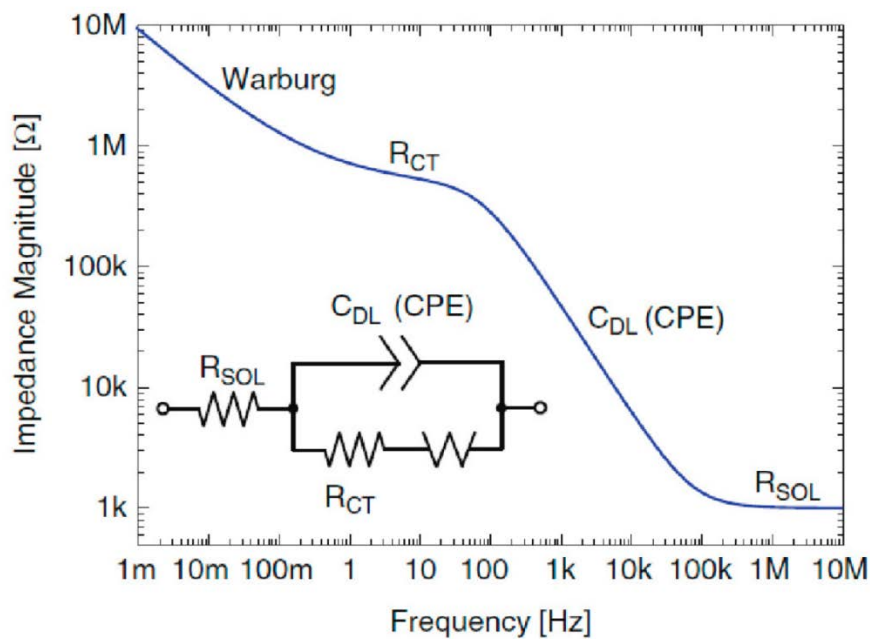
Figure 3.2: Bode plot of the impedance magnitude of an electrochemical interface [94].

When the frequency is plotted against the phase angle, a Bode plot is configured, which helps find the capacitance of the electrochemical systems.

3.2   Equivalent Circuit Modelling

One of the convenient analytic tools for interpreting EIS data is equivalent circuit modeling (ECM) [95]. The equivalent circuit is designed to identify and assess the characteristic elements of the EIS system. ECM can be combined with a physical model of the system; mechanistic interpretation is possible [96]. However, inappropriate models, each passive element of the EC provides facts on processes in the system. For example, processes occurring on coated metals that can be characterized include corrosion at coating defects [97],

adhesion [98], and undercoating corrosion [99].

The reactance of electrochemical systems is primarily capacitive. This response presents as depressed arcs in the complex plane or phase angles that approach but to not reach -90°. Therefore, a constant phase element (CPE) is exploited to improve fitting [95]. A CPE is a mathematical construction that accounts for dispersion in the value of the interfacial capacitance over the sample area connected with inhomogeneity on the surface of the electrode. The impedance of a CPE can be expressed as below:

$$Z_{CPE} = \frac{1}{Y_0(j\omega)^n} \tag{3.5}$$

where ω is the angular frequency, n is the CPE power number defined as $n = \frac{\alpha\pi}{2}$, α is the constant phase angle of the CPE and Y_0 is the CPE constant [101]. The CPE behaves as an ideal capacitor if the power number n equals 1. If it equals 0, the CPE behaves as an ideal resistor; if it equals -1, it behaves as an ideal inductance. Westing *et al.* used CPE to model the non-ideal behavior of epoxy coatings with different thicknesses and solvent concentrations applied to steel substrates. By analyzing the response of *n,* the authors could characterize the curing process [100].

It is common practice to present capacitance values instead of CPE parameters such as Y_0 or *n* [101]. There are at least two empirical methods to extract the accurate capacitance from the CPE parameters, the maximum frequency method introduced by Hsu and Mansfeld [101] and the parallel resistance method introduced by Brug *et al.* [102].

3.3   Potentiodynamic Polarization

The relationship between the current and potential of the electrochemical cell in the presence of two kinetically controlled reactions is given by Eq. (3.6), where I_{corr} is the corrosion current, E_0 is the potential at OCP, also called the corrosion potential, the β coefficients are the Tafel constants for the anodic and cathodic reaction, respectively.

Derivation for the potential, simplification, and rearrangement of (Eq. 3.6) results in (Eq. 3.7), which includes R_p, the polarization resistance. High polarization resistance implies a high corrosion resistance [103].

$$I = I_{corr}(e^{\frac{2.3(E-E_0)}{\beta a}} - e^{\frac{-2.3(E-E_0)}{\beta c}})$$ (3.6)

$$I_{corr} = \frac{\beta_a \beta_c}{2.3(\beta_a + \beta_c)} * \frac{1}{R_p}$$ (3.7)

In a potentiodynamic polarization experiment, one measures the current at different applied potentials, above and below the E_0. From these measurements, one can determine the E_0, I_{corr} And the Tafel constants, as illustrated in Figure 3.3, E_0 is the potential at which the extrapolation of the linear part of the anodic and cathodic branches intersect, and the I_{corr} is the current at this point. A drawback with this method is that it affects the sample since you drive the electrochemical reactions with the applied potential [104]. I used this method as a complement to the EIS measurements.
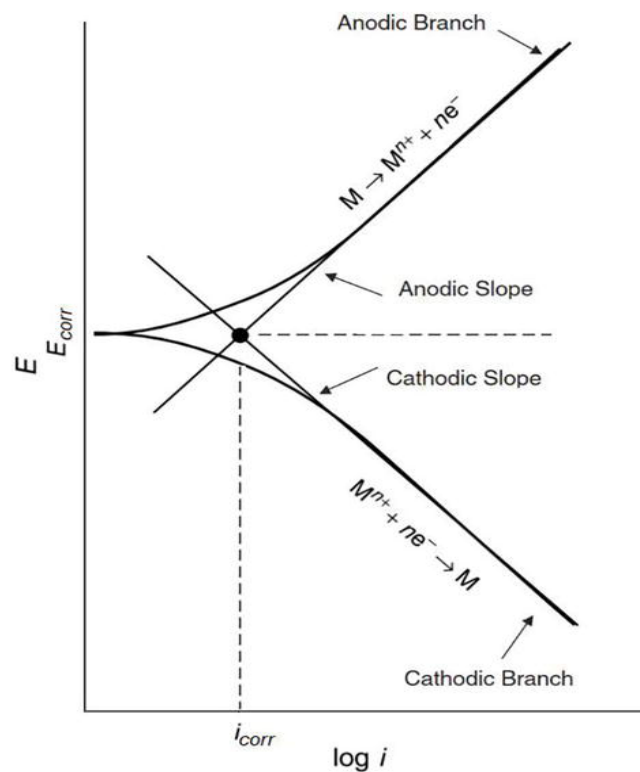
Figure 3.3: Typical data from a potentiodynamic polarization experiment with anodic and cathodic branches (curves). The slopes of the linear part of these branches are called Tafel slopes. [104]

24

3.4   Cyclic Polarization

Cyclic polarization is applied to investigate the corrosion behavior and pitting tendency of a corrosive material in an electrolyte. Figure 3.4 exhibits the electrochemical cell with its parts. In cyclic polarization, the potential begins in a potential below E_{corr}. Next, it is moved in the positive direction until it goes to the preselected potential or current. Then it is switched to more negative values to the beginning value of the potential. Higher breakdown potentials (E_{br}) suggestive of higher pitting resistance of Aluminum alloy is highly desirable. Therefore, cyclic polarization is an electrochemical test that can determine Aluminum alloys' tendencies toward pitting. For all heat exchangers, pitting results from atmospheric corrosion in environments containing pitting agents such as chloride. The electrolytes of these tests are selected in a way to simulate the effects of pollutants that exist in the environment. These contaminants include Sulfur, Chloride, and Nitrogen. Parameters measured in these tests are Passive potential (Ep), pitting potential (E_{PIT}) and pitting loop, which is the area under the potential-current loop. The pitting loop measures the pitting movements of Aluminum alloys [105].
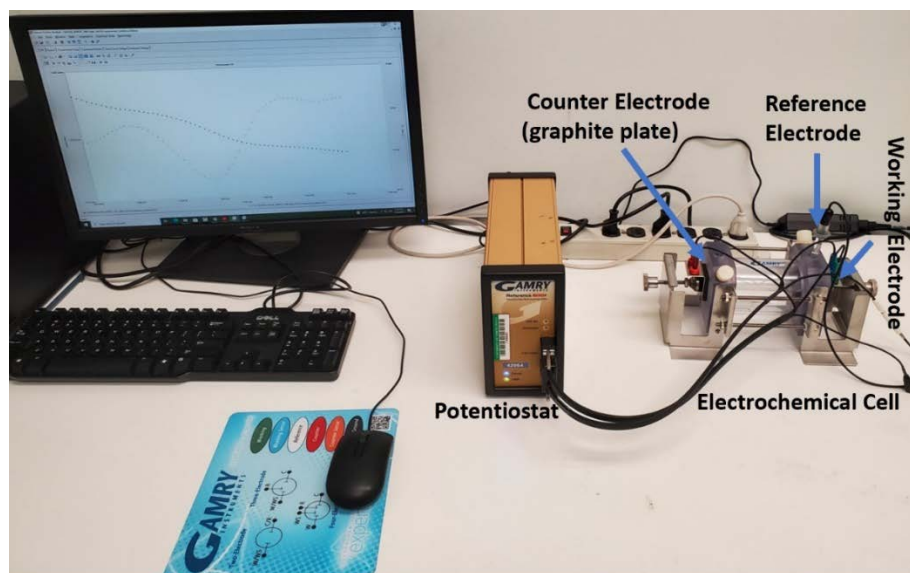
Figure 3.4: Experimental setup for EIS

3.5   Experimental Setup

This   work   uses   Gamry   600   plus   potentiostat   with   three-electrode   system

electrochemical cells. A potentiostat controls the voltage dissimilarity between a working electrode and a reference electrode. The potentiostat implements this control by introducing current into the cell via an Auxiliary, or Counter, electrode.

3.6   X-ray Photoelectron Spectroscopy (XPS) of AA 3102

X-ray photoelectron spectroscopy (XPS-PHI 5000 Versaprobe) was performed to confirm the presence of a thin sacrificial Zn layer on AA 3102 alloy. The binding energies were adjusted based on the C1s peak value at 284.6 eV. AA 3102 alloy, as received, was cleaned using Alcohol and Acetone and analyzed for Aluminum and Zinc peaks.

CHAPTER 4

NUMERICAL ANALYSIS

To analyze the effect of microchannel geometry accurately and efficiently, heat transfer between refrigerant flow and airflow in segmental MCHE was modeled using Computational Fluid Dynamics (CFD) simulation.

4.1   Modeling of Microchannel Heat Exchanger

To minimize the computational cost, the CFD computational model has consisted of a small section of an MCHE tube with five louvered shape fins attached to it, as shown in Figure 4.1. Only half of the fins' height on each side of the tube is considered due to the symmetric conditions of MCHE. The overall dimensions of the considered section of MCHE is $(0.4 \times 0.07 \times 0.05)(l \times w \times h)$ inch^3. Three microchannel geometries are considered for the tube, including circular, triangular and rectangular microchannels. All microchannels have a similar volume $(4.882 \times 10^{-5}$ inch$^3)$ but different hydraulic diameters, as listed in Table 4.1. In simulations, the coordinate system is selected in such a way that the Z axis is along with the axis of the microchannel.
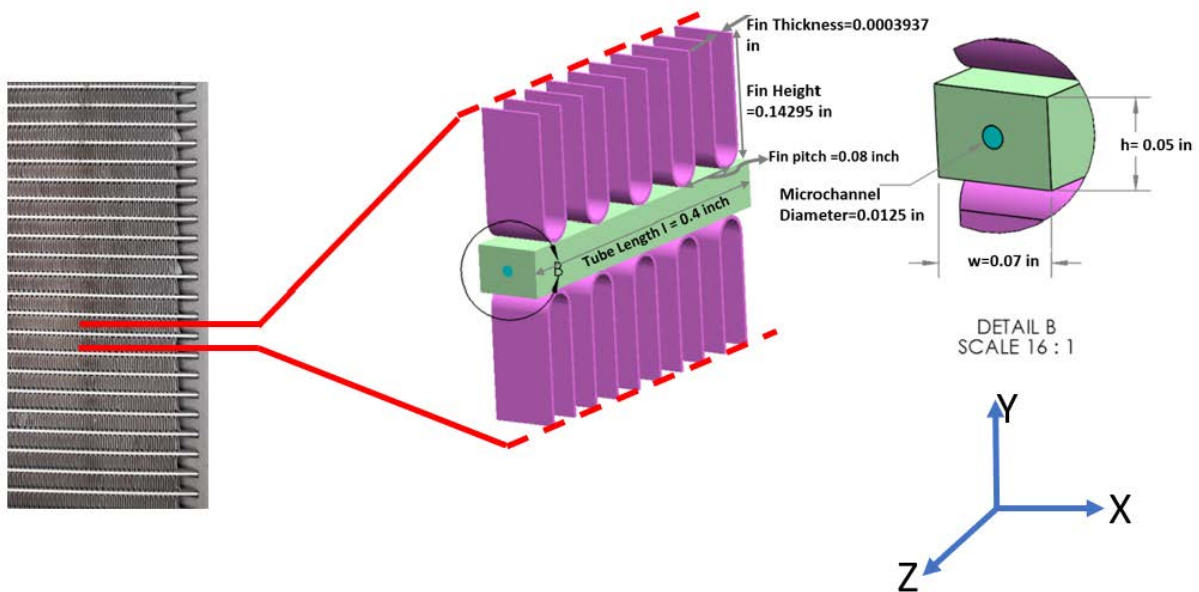
Figure 4.1: Characteristic part of MCHX.

The Y axis is parallel to the fin surfaces and along with the flat tube height. X axis is along with the flat tube width.

Table 4.1: Geometry specification of MCHE

Microchannel shape	Circular
Parameter	Value
Tube length l (inch)	0.4
Tube height h (inch)	0.05
Tube width w (inch)	0.07
Hydraulic diameter (inch)	0.0125 (Circular) 0.00972 (Triangular) 0.01108 (Rectangular)
Microchannel volume (inch^3)	4.8819 x 10^{-5}
Fin type	Louver
Fin thickness (inch)	0.0003937
Fin height (inch)	0.14295
Fin pitch (inch)	0.08

4.2   Mathematical Model

The segmental MCHE was simulated using ANSYS Fluent. Governing equations for the mass, momentum, and energy are solved using the finite volume method are below:

$$\frac{\partial \rho}{\partial t} + \vec{\nabla}.(\rho\vec{v}) = 0 \tag{4.1}$$

For steady state and incompressible flow, mass conservation equation 4.1 can be expressed as below:

$$\nabla.\vec{v} = 0 \tag{4.2}$$

Equation 4.3 and 4.4, show the momentum and energy equation for steady state and incompressible flow.

$$\rho \frac{\partial}{\delta t}(\vec{v}) + \nabla.(\rho\vec{v}\vec{v}) = -\nabla p + \mu\nabla^2\vec{v} + F \tag{4.3}$$

$$\rho C_p \frac{\partial T}{\partial t} + \rho C_p \vec{v}.\nabla T = \nabla.(k\nabla T) + \emptyset \tag{4.4}$$

where the static pressure p, molecular viscosity μ, velocity field $\vec{v}$, temperature T, specific heat at constant pressure C_p, body force F, and dissipation function $\emptyset$ represent the work done against viscous forces.

For the solid side, the following heat conduction equation is solved:

$$\rho C_p \frac{\partial T}{\partial t} = \nabla.(k\nabla T) + \emptyset \qquad (4.5)$$

4.3   Computational Domain, Boundary Conditions, and Grids

The computational domain contains three major regions: cross flow, microchannel flow, and solid regions. Figure 4.2 represents the schematic view of the computational domain. The crossflow domain is divided into the inlet region, the region between fins, and the outlet region.
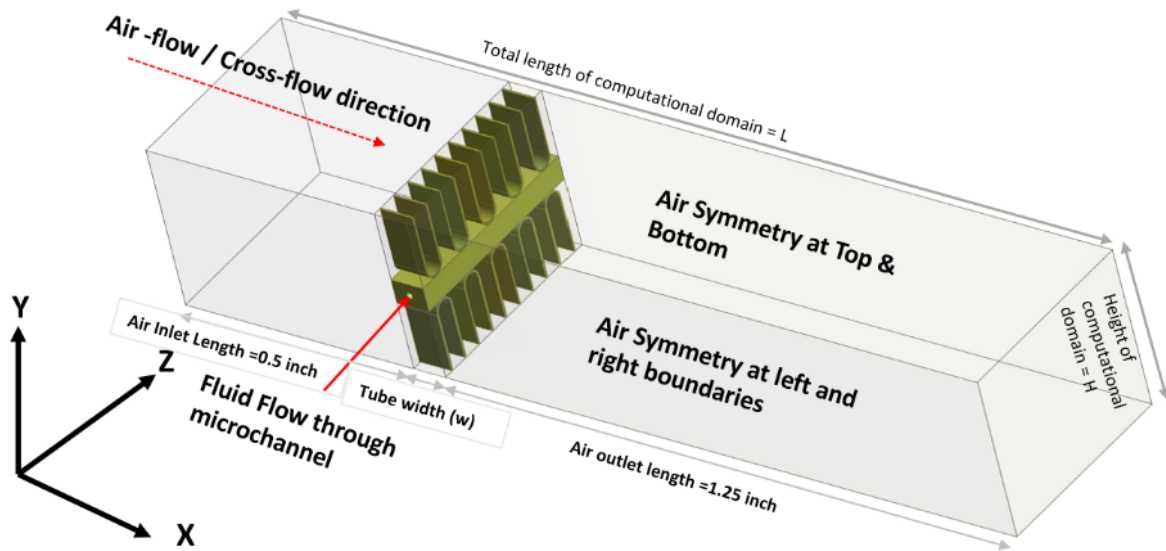
Figure 4.2: Computational domain for MCHE.

The crossflow domain is extended from X~-7 w (0.5 inch) to X~18 w (1.25 inch), where w is the width tube. The width and height of the crossflow domain are the same as the width and height of the section of MCHE considered in the simulation. The microchannel flow domain has a length of L=0.4 inch with the diameter of 0.0125 inch for cylindrical geometry and hydraulic diameter of 0.00972 inch and 0.01108 inch for triangular and square microchannels, respectively. The solid domain has two regions, a tube and a louver-shaped fin. The simulation includes the solid domain to model heat conduction in solid domains and predict the effect of non-uniform temperature distribution in the solid domain on heat transfer.

For the crossflow domain, unstructured quadrilateral/hexahedral grids are used. The number of grids in the crossflow domain is ~4.5M, as listed in Table 4.2. For the solid domain (fins and tube), the structural hexahedral mash is used, as shown in Figure 4.2. The surface grid for each fin's inner and outer surface has 65 along the fin's width and 248 along the fins' length. The surface grids are used to generate the structured hexahedral grids for fins. The number of grids in fins is 0.8M. The tube has also 3.3 M structured hexahedral grids. For the microchannel, prism and hexahedral grids are used. The microchannel has 216, 205, and 225 grids in the streamwise direction and 15600, 14988, 15920 along the perimeter for the circular, triangular, and square geometry, respectively.

(a)   (b)
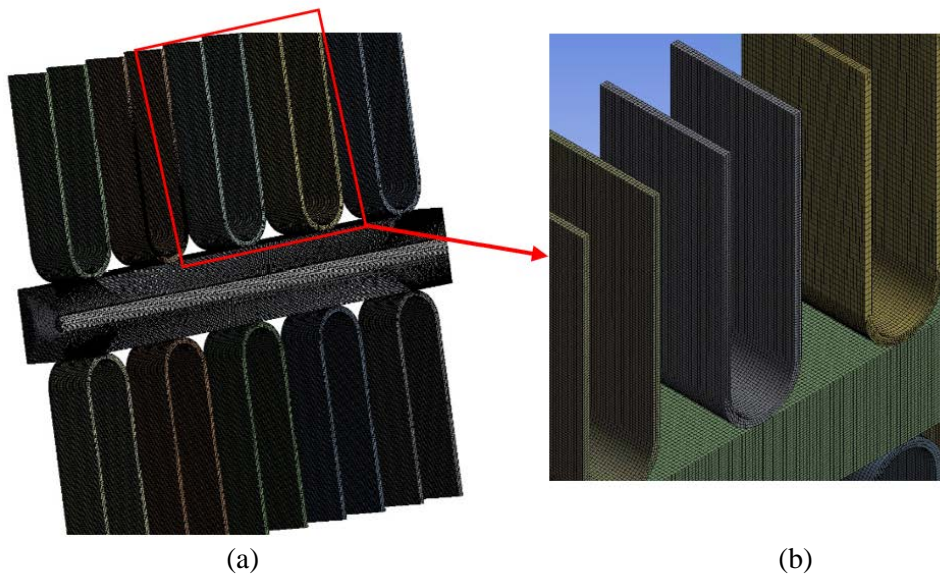
Figure 4.3: Details of triangular prism and hexahedral mesh of circular MCHE (a) cross-sectional view of solid domain and (b) enlarge view of Red marked area.

Table 4.2: Grid sizes

Domain	Grid
Crossflow domain	4463186
Microchannel	43992 (Circular) 42877 (Triangular) 44154 (Square)
Fin	823857
Rectangular tube	3339600
All domains	8670635 (Circular) 8669520 (Triangular) 8670797 (Square)

The number of grids in all microchannels is nearly 43k. The total number of grids for each case is about 8.7M, decomposed into 32 cores for parallel processing.

The crossflow domain's velocity is set to 16 m/s and the inlet temperature is 26.85 °C. The crossflow outlet is a pressure outlet. The symmetric boundary condition is used for all sides of the domain. Air is used as a working fluid for the crossflow domain. For this simulation, properties of air, such as density ρ_{air} is set as 1.225 kg/m³ and specific heat is assigned as $c_{p,air} = 1006.43 \frac{J}{Kg.K}$. For the microchannel domain, the velocity is set to 0.2 m/s at the inlet, zero velocity gradient boundary condition is used at the exit, and a non-slip boundary is employed at wall. For microchannel, water is used with viscosity $\mu = 0.001003 \frac{kg}{ms}$, specific heat, $C_p = 4182 \frac{Jkg}{k}$, and density $\rho = 998.2 \frac{kg}{m^3}$. For the solid domain, the surface of the fins and the exterior surface of the tube are thermally coupled with the crossflow domain, while the interior surface of the tube is thermally coupled with the microchannel flow domain. The tube section has an inlet temperature of 26.85 °C. Symmetric boundary conditions are used at the upper and lower boundaries of fins i.e., $\frac{\partial T_{fin}}{\partial y} = 0$. Details of the boundary condition are given in Table 4.3.

Table 4.3: Boundary conditions

Microchannel	Inlet (water inlet, z-direction)	Velocity inlet: $U_w = 0.2$ m/s Inlet temperature of the water, $T_{w,in} = 50$ °C
	Outlet	Pressure outlet
	Wall	Via system coupling with solid for temperature; No-slip boundary condition for velocity
Solid (aluminum)	Inlet	Inlet temperature $T_S = 26.85$ °C
	Outlet	Heat flux=0
	Wall	Via system coupling with air for temperature; No-slip boundary condition for velocity
Fin (aluminum)	Top fin and bottom fin boundaries	Symmetric
Crossflow	Inlet (air inlet, x-direction)	Velocity inlet: $U_a = 16$ m/s (Inlet temperature of the air, $T_a = 26.85$ °C)
	Outlet	Pressure outlet
	Side boundaries	Symmetric

4.4   Finite Volume Method

The mathematical model is entirely determined by partial differential equations and given boundary conditions. The application of differential Equations in problem-solving in engineering practice is extensive because they best describe mathematically the processes that occur in nature. However, solving partial differential equations relied on search before computer time analytical solutions that required considerable effort. Some solutions, especially in the case of highly complex geometry, could not even be found. By applying numerical methods mathematically, the model is explained into systems of algebraic equations. Today, computers are numerically used to solve partial differential equations, which is the fastest way to develop their solutions. Some methods for finding partial differential solutions in the equations are the finite difference method, finite element method, and finite method volume. The basis of solving partial differential equations by the control volume method is the division of the domain and the period in which we observe the process to the final number of volumes and time steps. Finite volume methods have become widespread in Computational Fluid Dynamics CFD because they first ensure that the discretization is conservative. Also, it does not necessitate a coordinate transformation to be applied for irregular meshes. This increased flexibility can be used for excessive compensations in generation grids about arbitrary geometries [106].

Moreover, the finite volume method combines the simplicity of the finite difference's method with the local accuracy of the finite element method; also, at the same dimension of the discretized problem, the accuracy is higher than with finite differences and nearly the same as with finite elements [107]. The finite volume method has been used to discretize the governing equations and boundary conditions. Fluids were assumed incompressible with constant physical properties, and the flows were assumed to be laminar. The couple algorithm for pressure-velocity coupling was used, which solves the momentum and continuity equations

together, unlike the predictor-corrector segregated methods. The convection-diffusion terms have been discretized using the second-order Upwind scheme.

4.5 Couple Algorithm

The coupled solver simultaneously solves the governing equations of continuity, momentum, and (where appropriate) energy (i.e., coupled). Since the governing equations are non-linear (and coupled), numerous iterations of the solution loop must be performed before a converged solution is found. The coupled scheme acquires a robust and efficient single-phase operation for steady-state flows, with higher performance than the segregated solution schemes. This pressure-based coupled algorithm offers an substitute to the density-based and pressure-based segregated algorithm with SIMPLE-type pressure-velocity coupling. The coupled algorithm solves the momentum and pressure-based continuity equations together. One of the limitations of the pressure-based coupled algorithm is not well-suited with the non-iterative time advancement solver [108].
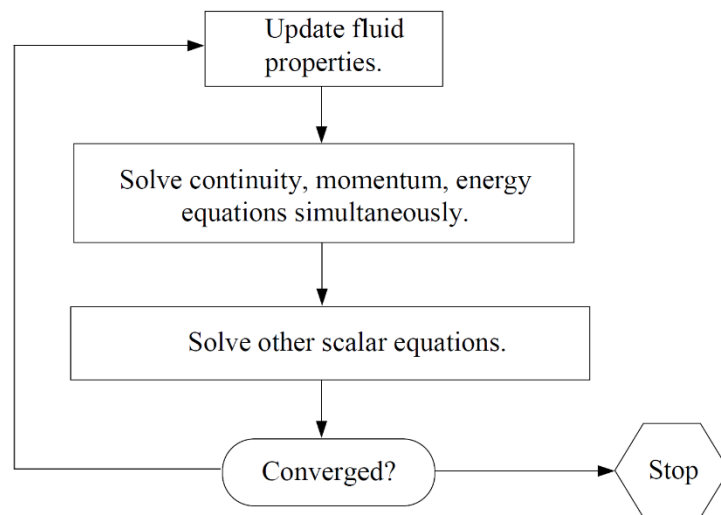

Figure 4.4: Overview of the Coupled Solution Method.

Each iteration consists of the steps shown in Figure 4.4 and outlined below:

1. Fluid properties are updated based on the existing solution. (If the calculation has just been initiated, the properties of the fluid will be updated based on the initialized solution.)

2. The continuity, momentum, and energy equations are solved simultaneously for steady-state conditions.

3. Where appropriate, equations for scalars such as convection (conjugate heat transfer) are solved using the beforehand updated values of the other variables.

4. These steps are continued until the convergence criteria are happened.

4.6   Grid Uncertainty

In numerical simulation, being efficient in computational time and having accurate results are equally important. However, if we want very high accuracy or high grid size, that will have high computational time. Therefore, to get accurate results with minimum computational time, we need to conduct grid independence or grid uncertainty tests. Grid verification study was conducted for the microchannel flow using 20 thousand grids for coarse mesh, 40 thousand for medium, and 80 thousand grid sizes for fine mesh. The predicted centerline velocity changes 0.27% from coarse to medium and 0.25% from medium to fine grid, suggesting the results are fairly insensitive to the grid size. Hence, the medium grid is used for all simulations.
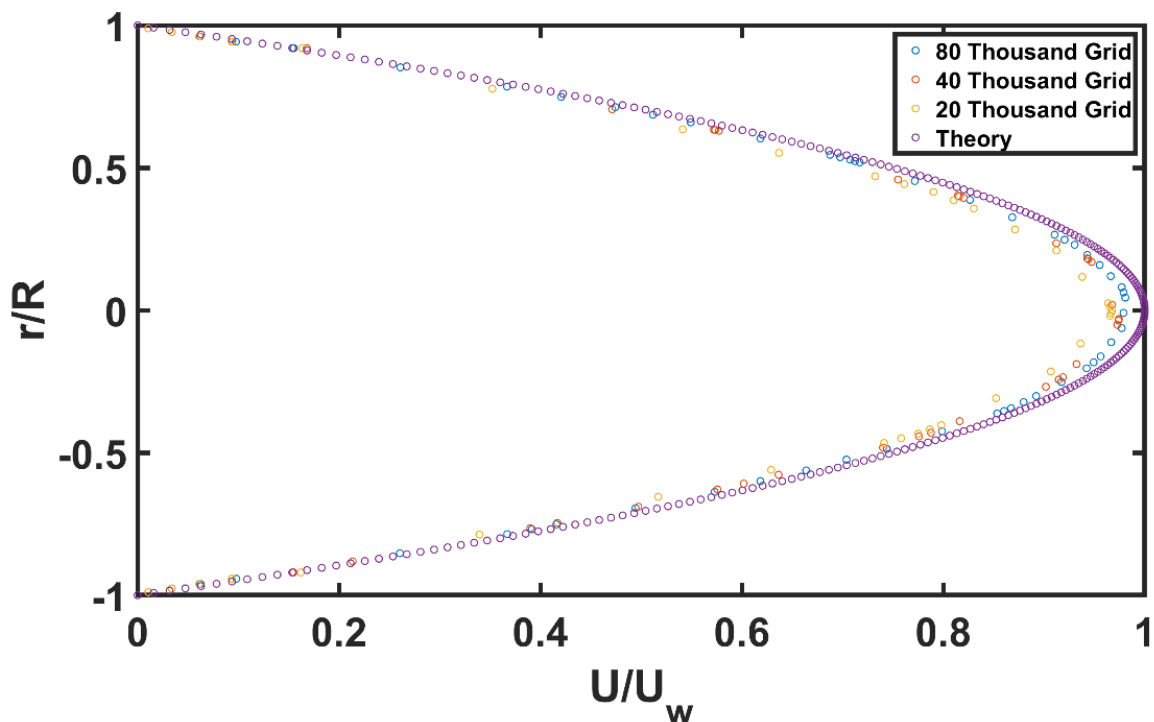
Figure 4.5: Verification analysis for flow through circular microchannel.

To validate the results, Figure 4.5 shows the analytical velocity profile compared to the predicted one. The results show that the predicted profile agrees well with the theory. The maximum error is for the velocity at the centerline which is 3.25% for the coarse grid dropping to 2.56% and 1.93% for the medium and fine grids, respectively.

$$\text{At } 50°\text{C}, \ Re_D = \frac{\rho u_m D}{\mu} = \frac{998.2 \ \frac{kg}{m^3} \times 0.2 \frac{m}{s} \times 0.000375 \ m}{0.0005 \ \frac{kg}{ms}} = 149.73$$

$$Re_D < 2300; \ laminar \ flow$$

$$\text{At } 50°\text{C}, \ hydrodynamic \ entry \ length,$$

$$x_{fd,h} \approx 0.05 \times Re_D \times D = 0.11 \ inch$$

CHAPTER 5

EXPERIMENTAL RESULT

This investigation aims to assess the corrosion tendency of AA 3102 in general and its pitting vulnerability in aqueous corrosive environments containing low and high concentrations of the combination of sodium chloride and ammonium sulfate. Pitting potential, passive potential, and corrosion rates are measured using cyclic polarization tests. In addition, electrochemical impedance spectroscopy (EIS) analysis was done on the alloy in the same corrosive electrolytes. Results indicate AA3102 alloy is most vulnerable to electrolytes used sea water acetic acid test (SWAAT) is ASTM G-85 standard test compared to other less aggressive electrolytes used in this research. However, the electrolyte used in the SWAAT test is highly acidic (pH=2.9) and makes it non-representative of natural atmospheres, creating doubts about the validity of ASTM G-85 test results. On the other hand, electrolytes used in this research have pH values ranging from 4.0 to 5.8, which is closer to nearly neutral environments encountered in many atmospheres.

Many standard tests have been developed to promote degradation faster than in-service conditions. Reputable manufacturers of HVAC-R industries have developed their corrosion testing methods while standard testing protocols such as salt fog test (ASTM B-117), sea water acetic acid test (SWAAT, ASTM G-85), and copper-accelerated acid-salt (Fog) spray test (CASS, ASTM B368) [109-110]. Nasrazadani at el. [111] has published a comprehensive review of cabinet-based accelerated corrosion testing used in the HVAC-R industry folks. These methods are ASTM B117 continuous salt spray fog, ASTM G154 weathering chamber, and ASTM G85- Prehension [112]. Salt-spray (FOG) Tests are the most common type of cabinet test. Unfortunately, most of these testing methods take too long to complete and produce results that are non-representative of actual field conditions and produce results that lack reproducibility and unreliable data that makes results mostly inconclusive. The duration

of these tests can be up to 5000 hours.

Long-term atmosphere exposures or accelerated corrosion tests are widely used to assess zinc coatings' corrosion resistance [113-115]. However, compared with accelerated corrosion tests, long-term atmosphere exposures are time-consuming and region-dependent, unfavorable for applying and promoting new coatings. On the other hand, electrochemical methods, particularly the electrochemical impedance spectroscopy (EIS) technique, are an efficient and convincing tool for analyzing the corrosion behavior of metals [116-117]. Aqueous corrosion is an electrochemical process that can be tracked utilizing electronic devices that applies an electrical signal to measure and control the electrical charge transfer; in pursuance of assessing the reaction kinetics and mechanism of the corrosion progression that takes place at the metal interface. The electrochemistry impedance is the relationship between a potential energy difference and the flow of electrons generated by a wave signal employed in an aqueous media. EIS was used to evaluate the properties of thin oxide films formed on metals, supervising superficial degradation of coatings because of the swelling process. Surface variations due to ion adsorption at the interface can also be detected, knowing the kinetics reaction on metals under the corrosion process. In addition, electrochemical methods can deliver information on the reactions and mechanisms of electrochemical deterioration.

This work aimed to study the corrosion resistance of the Al-3102 microchannel heat exchanger tube in different chloride and sulfate concentrate electrolyte. First, the corrosion resistance of the Al-3102 microchannel heat exchanger tube was monitored by potentiodynamic polarization test and electrochemical impedance spectroscopy. Furthermore, the surface and cross-section morphological characteristics of zinc-based coatings after immersion tests were investigated by scanning electron microscopy (SEM). Finally, EIS results, including R_{sol}, R_{pore}, and R_{ct} of AA3102 with very thin arc evaporated porous Zinc film on AA 3102 along with their equivalent circuit, is presented.

5.1 Electrochemical Testing

A heat exchanger manufacturer provided AA3102 (Fe 0.70%, Si 0.40%, Zn 0.30%, Cu 0.10%, Ti 0.10%, Mn 0.40%, balance Al) tube sheets with 100 μm thick arc evaporated zinc film was cut to 1 in^2, polished using 3, 0.5, and 0.05 μm alumina particles to remove all debris and greases from the surface followed by rinsing in acetone, alcohol, and distilled water. A flat cell with 1 cm^2 exposed sample surface area, along with a three-electrode system, was utilized in this research. Cyclic polarization is used to investigate and study material's corrosion behavior and pitting tendency in corrosive electrolytes. Cyclic voltammetry was performed using the Applied Princeton Research EG&G PARSTAT 2273 system for a potential range of -2.0 to +0.2 V at a scan rate of 0.5 mV/s with 1 mV steps. A saturated Calomel Electrode (SCE) was used as a reference electrode in all measurements in this investigation. Parameters that are measured in these tests are Passive potential (Ep), pitting potential (E$_{PIT}$), breakdown potential (E$_{br}$), and pitting loop, which is the area under the potential-current loop. The pitting loop measures the pitting tendencies of Aluminum alloys. EIS analysis was done using the frequency range from 100,000 Hz down to 0.1 Hz with an amplitude of 5 mV for the experiments reported here.

5.2 Surface Characterization of AA 3102 Samples

5.2.1 XPS Analysis

Elements detected on the surface of AA 3102 samples include Al, Zn, O, and C. Carbon is an impurity coming from the instrument. However, Al, Zn, and O are present as a thin layer of Zn (~ 100 μm) as sacrificial anode protecting aluminum. Oxygen as a minor constituent indicates the presence of alumina (Al$_2$O$_3$). Peaks used to identify Zn are located at binding energy for Zn$_{2p1}$ and Zn$_{2p2}$. Figure 5.1 illustrates the XPS Spectrum of AA3102 sample.
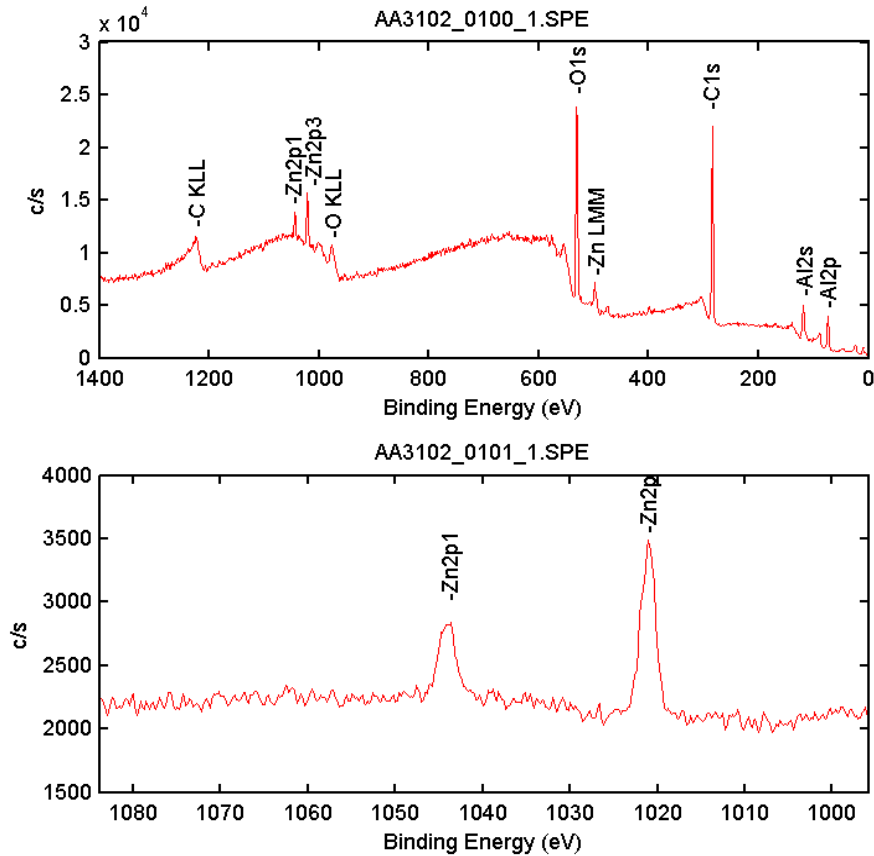
Figure 5.1: XPS Spectrum of AA3102 sample.

5.2.2 DC Electrochemical Analysis

Cyclic polarization curves on AA 3102 in corrosive solutions containing high sodium chloride (3.5%) and low ammonium sulfate (0.5%) are shown in Figures 5.3 to 5.5. Corrosive solutions were chosen to study the impact of pollutants such as salt in marine environments and sulfur in industrial atmospheres on the corrosion of AA 3102 alloy. Upon the completion of each test, several measured parameters of interest, including corrosion potential (E_{corr}), primary passive potential (E_{pp}), protection potential (E_{PR}), and transpassive potential ($E_{transpassive}$) were identified. Cyclic polarization plots are commonly used to assess the pitting tendency of engineering alloys in corrosive environments, most of which contain chloride ions. If the reverse path results in higher currents than the forward path for any given potential, then a hysteresis loop is generated in the potential-current plot. The generated loop's size indicates

the alloy's pitting tendency in each corrosive electrolyte. A larger loop area indicates a higher pitting tendency of the alloy in the corrosive electrolyte. If the reverse path results in lower currents than its forward counter path, the alloy is not vulnerable to pitting in that corrosive electrolyte. In addition, when protection potential is more positive than passive potential, the alloy is not expected to undergo pitting in that electrolyte.

Typical cyclic polarization curve for AA 3003 is shown in Figure 5.2. Figures 5.3 to 5.6 show the Cyclic Polarization plot of AA 3102 in 3.5% Sodium Chloride and 0.5% Ammonium Sulfate solution but employing different techniques for sample preparation. A higher concentration of sodium chloride is expected to increase the probability of pitting corrosion in AA 3102.
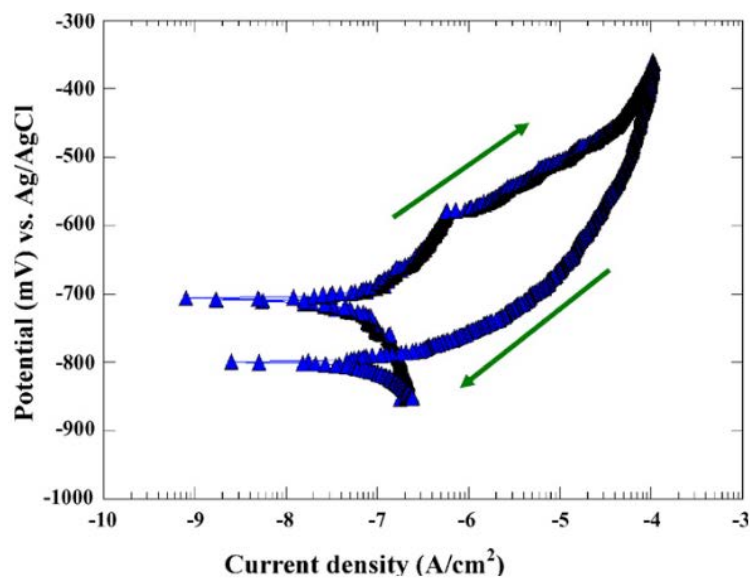

Figure 5.2: Cyclic polarization curve of EN AW-3003 alloy (Si 0.15%*, Fe 0.48%, Cu 0.12%, Mn 1.1%, Mg 0.03%, Zn <0.01%) in 10 mM NaCl solution [118].

Figure 5.3: Cyclic Polarization plot of AA 3102 in 3.5% Sodium Chloride and 0.5% Ammonium Sulfate solution. (Sample polished)

Figure 5.4: Cyclic Polarization plot of AA 3102 in 3.5% Sodium Chloride and 0.5% Ammonium Sulfate solution. (Sample rinsed with DI water)

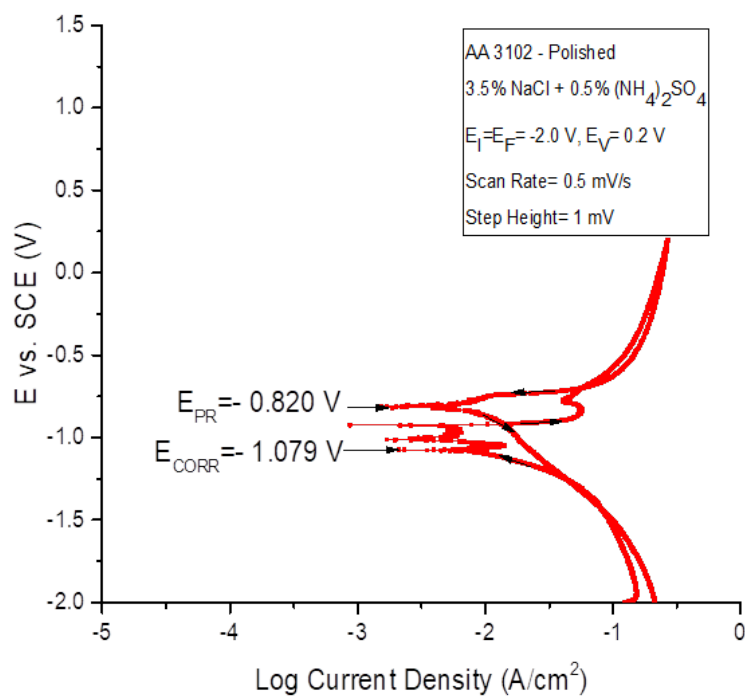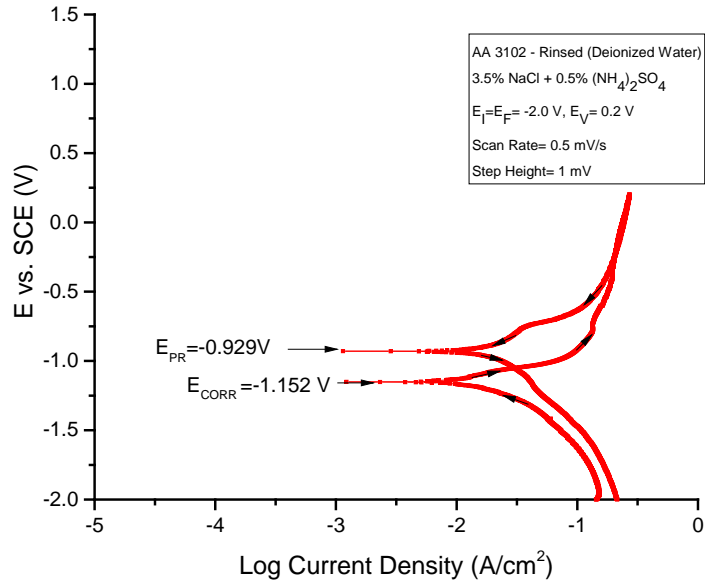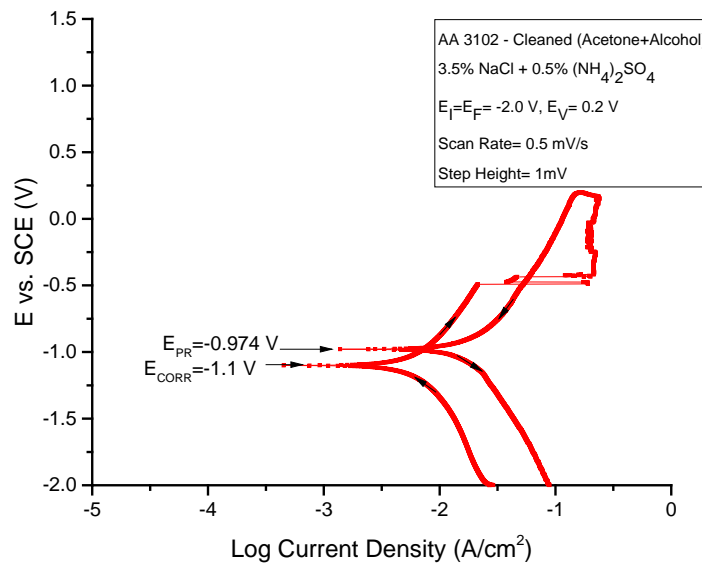**Figure 5.5: Cyclic Polarization plot of AA 3102 in 3.5% Sodium Chloride and 0.5% Ammonium Sulfate solution. (Sample cleaned with acetone and alcohol)**
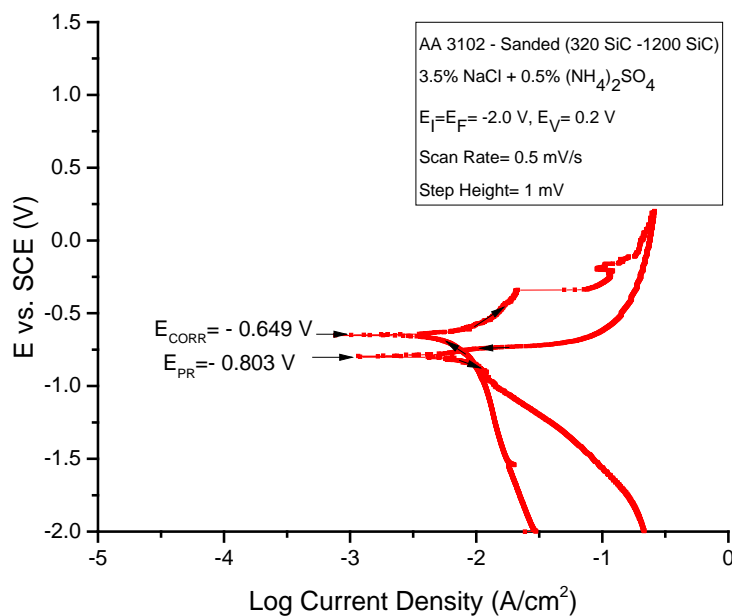

Figure 5.6: Cyclic Polarization plot of AA 3102 in 3.5% Sodium Chloride and 0.5% Ammonium Sulfate solution. (Sample sanded or remove the Zn coating)

Besides pitting potential and other related parameters measured, corrosion rate of AA 3102 alloy was measured in the corrosive electrolytes used in this investigation. Table 5.1 show parameters used to calculate corrosion rates including corrosion current (Icorr) and thickness loss (mpy) of the alloy in these electrolytes.

Table 5.1: Average corrosion rates of Ally 3102 alloy in various corrosive electrolytes.

No	Solution	pH	E_{corr} (mV)	I_{corr} (µA)	βc (mV)	βa (mV)	Corrosion rate (mpy)
1	3.5% NaCl + 0.5% $(NH_4)_2SO_4$	4	-1176	104	97	186.5	44.2
2	3.5% NaCl + 0.5% $(NH_4)_2SO_4$	5.6	-1173	43.6	64.5	182.5	18.6
3	0.5% NaCl + 3.5% $(NH_4)_2SO_4$	5.6	-1133	31.31	75	57.5	13.35
4	4.2% NaCl + 1%Glacial Acetic Acid (SWAAT)	2.9	-1036	202.9	226	58.5	86

5.2.3 Scanning Electron Microscopy (SEM)

SEM micrographs of AA 3102 alloy presented in Figure 5.7 to 5.9 shows severe pitting in all electrolytes, with the most extensive pitting in SWAAT electrolyte, which is most acidic followed by high chloride and high chloride and high sulfate electrolytes that have higher pH acidity. As expected, pit formation is initiated at the weakest part of the surface where grain boundaries are located.

Figure 5.7: SEM image of AA3102 surface after cyclic polarization test in 0.5% Sodium Chloride and 3.5% Ammonium Sulfate solution.

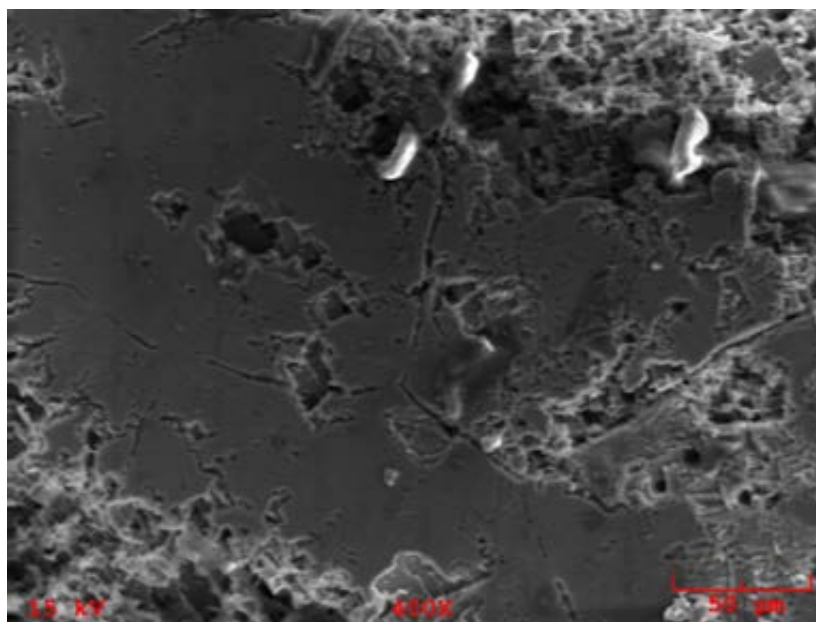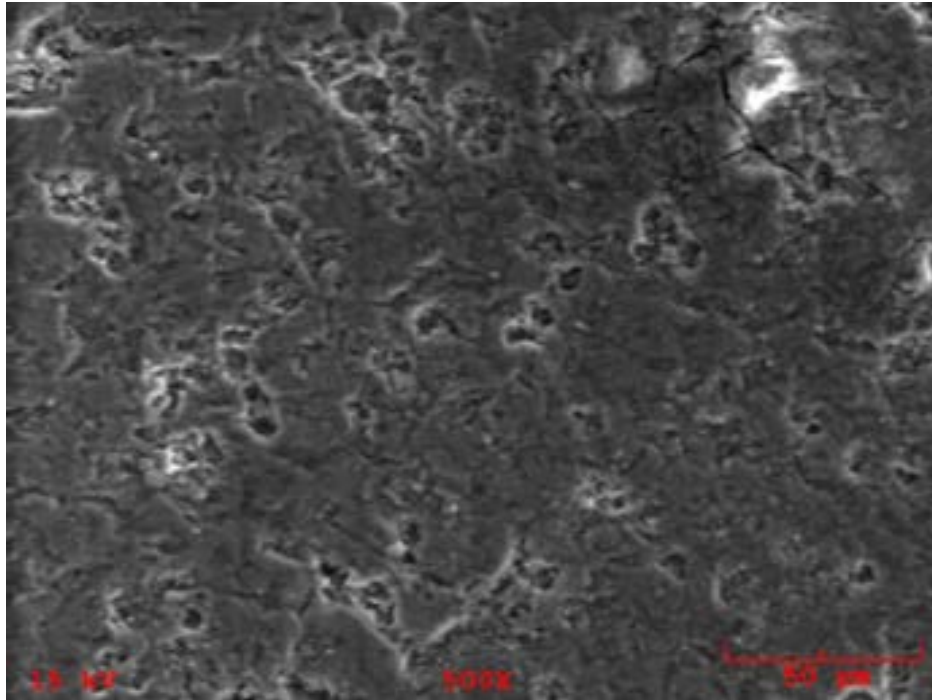**Figure 5.8: SEM image of AA3102 surface after cyclic polarization test in 3.5% Sodium Chloride and 0.5% Ammonium Sulfate solution.**
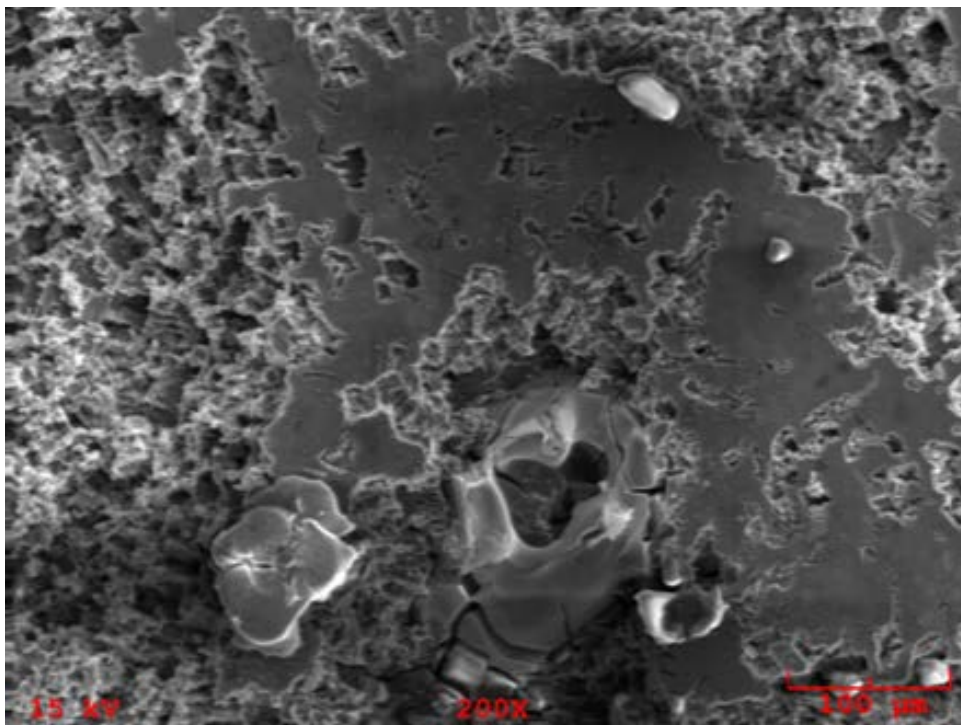

Figure 5.9: SEM image of AA3102 surface after cyclic polarization test in SWAAT electrolyte

Figure 5.9 illustrates an SEM micrograph of AA 3102 surface after cyclic polarization

showed severe grain boundary attack and regions with deep anodic dissolution of the alloy.

43

5.3 Electrochemical Impedance Spectroscopy (EIS)

This work aimed to study the corrosion resistance of the Al-3102 microchannel heat exchanger tube in different chloride and sulfate concentrate electrolyte. EIS is a technique that measures the impedance of an electrochemical system, and by inference, it can measure how well the coating protects the substrate. An excellent protective barrier will have a capacitive Bode plot, while a breached coating will have resistive traits at the low-frequency end of the EIS spectrum.

In one of the interpretations of this model, an assumption is made that the coating has been partially delaminated from the metal substrate, and the delaminated area is filled with solution. The interface between this pocket of solution and the bare metal is modeled as a double layer capacitance, CPE_{ct}, in parallel with a kinetically controlled charge transfer reaction element represented by the charge transfer resistance R_{ct}. It is sometimes also represented as a polarization resistance R_{pore}, a component representing the resistive corrosion product layer on the metal plate. The equivalent circuit model diagram is shown in Figure 5.10(b). In Figure 5.10(a), in the Nyquist plot, a second semicircle starts to appear. The first semicircle intercepts the real axis near the origin at the R_s value and ends at a value of $R_{pore} + R_s$, where the second semicircle starts. The second semicircle ends at a value of $R_{pore} + R_s + R_{ct}$. R_{ct} is inversely proportional to the corrosion rate. For 3500 mg NaCl + 500 mg $(NH_4)_2SO_4$ (pH=4.0) the solution, the value of $R_{sol} = 56.11\ \Omega$, $R_{pore} = 907.6\ \Omega$, $R_{ct} = 127.3\ \Omega$. For 3500 mg NaCl + 500 mg $(NH_4)_2SO_4$ (pH=5.6) the solution, and 500 mg NaCl + 3500 mg $(NH_4)_2SO_4$ (pH=5.6) the $R_{sol} = 44.34\ \Omega$ and 78.23 Ω, $R_{pore} = 382.96\ \Omega$ and 220.3 Ω, $R_{ct} = 629.4\ \Omega$ and 321 Ω. As shown in the schematic diagram in Figure 6(b), the charge transfer resistance R_{ct} is obtained from the addition of R_{pore} and R_{ind}. For 4.2% NaCl + 1%Glacial Acetic Acid (SWAAT) (pH=2.9), the value of $R_{sol} = 5.8\ \Omega$, $R_{pore} = 8.52\ \Omega$, $R_{ind} = 0.1\ \Omega$

These equivalent electrical circuits (EEC) models describe the impedance spectra for oxide products formed by corrosion reactions on the metal surface, anodizing coatings, or Zn-coated metals after exposure to corrosive electrolytes. Where CPE_{pore} is the capacitance of oxide film connected in parallel to R_{pore} that is, the oxide resistance, both connected in series to Randles circuit (RC) parallel, which contributes to the electrical response of the double layer interface. From Figure 5.10(a), the diameter of the second semicircle is increasing in EIS 2 compared with EIS 1. This is because EIS 1 and EIS 2 have the same high chloride concentration, and EIS 2 has a higher pH value.
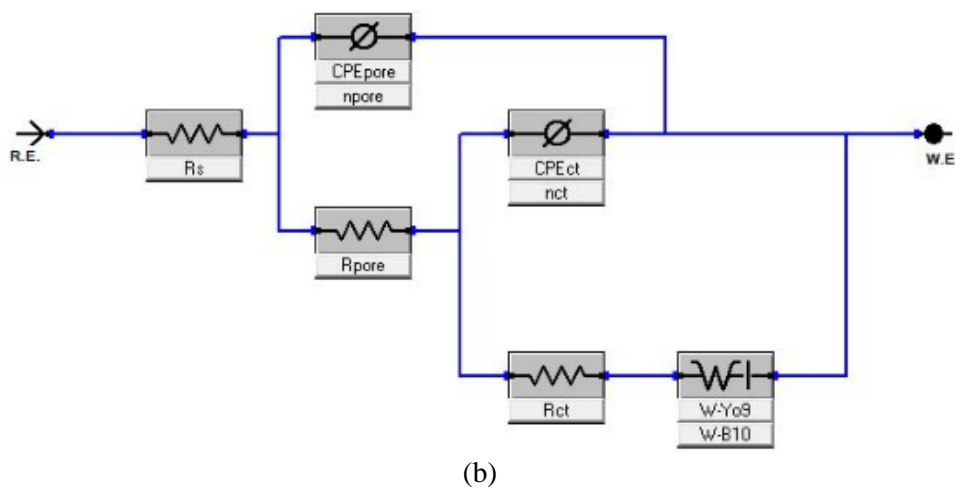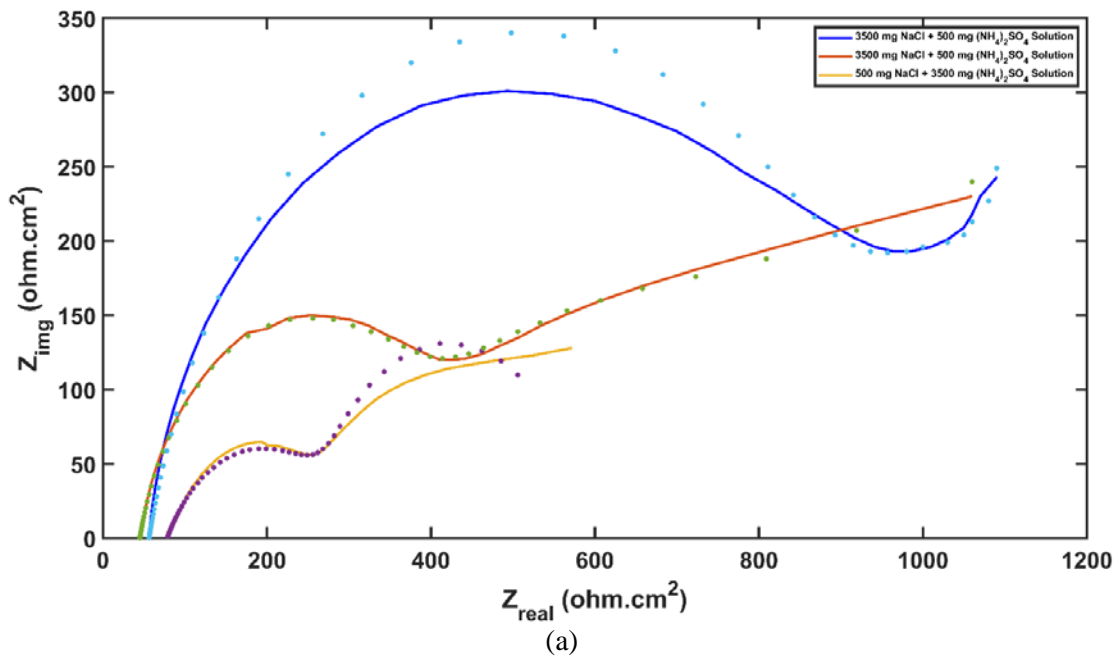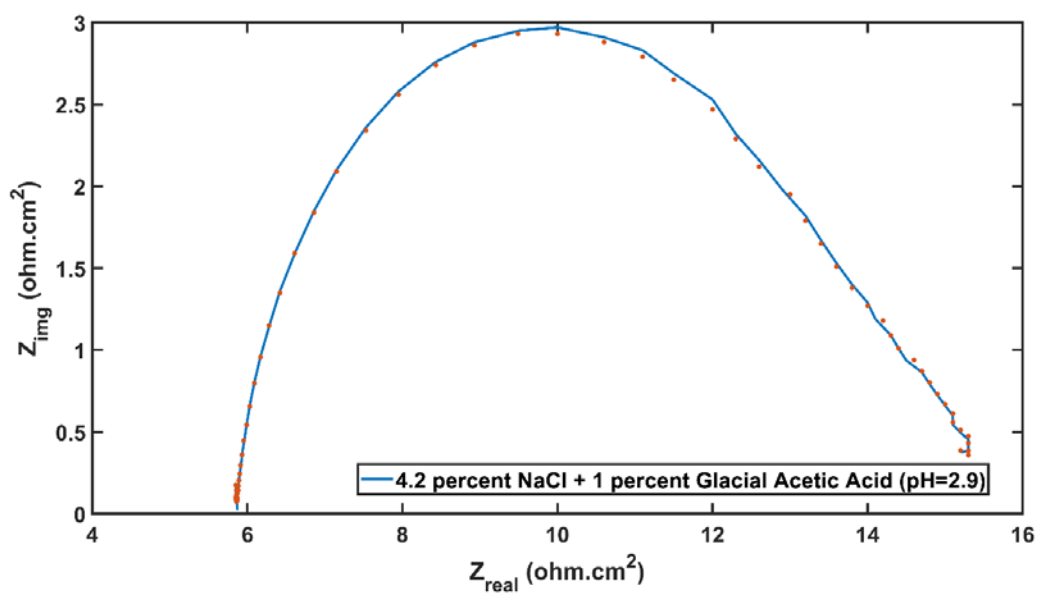

(a)

(b)

Figure 5.10: (a) Nyquist plot for high chloride at different pH levels, high sulfate solution, and (b) Equivalent circuit model used to analyze the experimental data.

45

In Figure 5.10(b), the equivalent circuit is designed to identify and assess the characteristic elements of the EIS system. For example, the diffusion of molecules or redox species can initiate an added resistance known as the Warburg impedance (W), which is frequency dependent. Warburg impedance (W) is small at high frequencies but at low frequencies, W increases due to the redox molecules having the force to diffuse at low frequencies. Warburg resistance is added due to the effect of a diffusion process at the electrode-electrolyte interface. Also, a constant phase element (CPE) is added to the equivalent circuit to show the non-ideal capacitance activities. Rp is the polarization resistance of the Al-3102 sample containing the Zn inhibitor. Table 5.2 describes the EIS experiment is used in this study. The polarization resistance is linked with corrosion happening on the metal surface. Therefore, a higher Rp value denotes higher corrosion resistance. The fitted EIS parameters are shown in Table 5.3.

Table 5.2: EIS study of Al 3102

Experiment	Solution	pH
EIS 1	3500 mg NaCl + 500 mg $(NH_4)_2SO_4$	4.0
EIS 2	3500 mg NaCl + 500 mg $(NH_4)_2SO_4$	5.6
EIS 3	500 mg NaCl + 3500 mg $(NH_4)_2SO_4$	5.6
EIS 4	4.2% NaCl + 1%Glacial Acetic Acid (SWAAT)	2.9

(a)

(b)
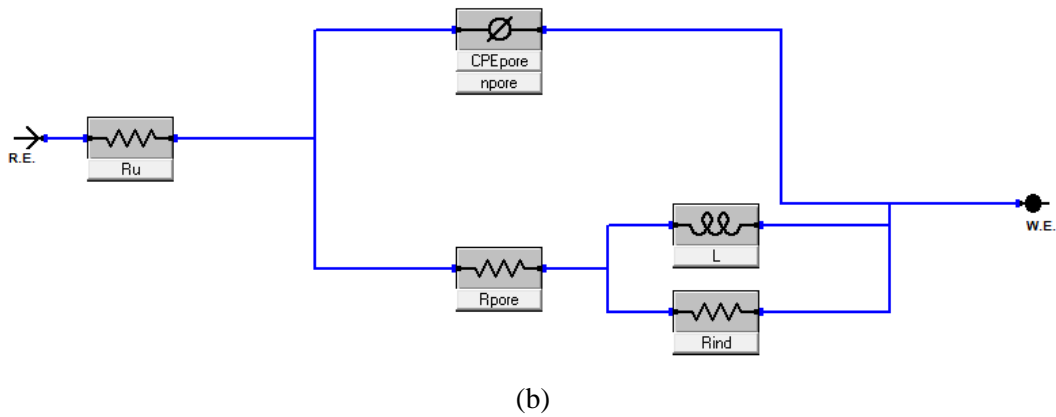
Figure 5.11: a) Nyquist plot for SWAAT solution and b) Equivalent circuit model used to analyze the experimental data.

Figure 5.11 (a) illustrates the inductive loop at the low-frequency region for the SWAAT solution. Interpreting the inductive loop is one of the most challenging problems in applying EIS for corrosion systems from an experimental and theoretical viewpoint. Most experimental impedance spectra containing an inductive loop in the low-frequency region have been determined at Ecorr in acid media in the presence of inhibitors.
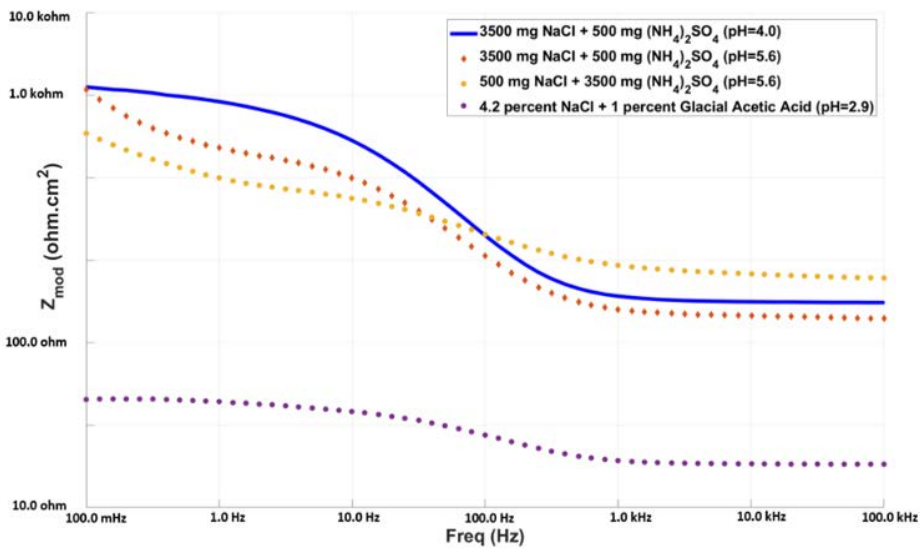
Figure 5.12: Bode plot for high chloride at different pH levels high sulphate and SWAAT solution.

In Figure 5.12, the frequency is plotted against the impedance, which helps find the capacitance of the electrochemical systems. Figure 5.12 is also known as the Bode plot.

The goodness of fit should be decreased by adding a new circuit element to the equivalent circuit model. For example, adding Warburg impedance (W) on experiment EIS (1-3) decreased the goodness of fit value by around tenfold. Therefore, the lower value of the goodness of fit in Table 5.3 justifies the equivalent circuit model.

Table 5.3: Equivalent circuit parameters.

Parameter	Units	EIS 1		EIS 2		EIS 3	
		Value	±Error	Value	±Error	Value	±Error
Rs	ohm	56.11	0	44.34	4.12E-03	78.23	8.07E-01
CPEpore	S*s^a	4.63E-05	1.51E-06	6.18E-05	6.42E-06	1.86E-04	1.37E-05
npore		8.17E-01	5.41E-03	8.18E-01	1.48E-02	6.25E-01	1.22E-02
Rpore	ohm	907.6	0	382.96	0	220.3	0
Rct	ohm	127.3	0	629.4	0	321.1	0
CPEct	S*s^a	2.02E-03	3.79E-04	2.16E-03	6.69E-04	2.35E-03	6.28E-04
nct		1	1.39E-01	6.72E-01	1.07E-01	8.69E-01	1.16E-01
W-Yo10	S*s^(1/2)	4.66E-03	1.35E-03	-3.70E-03	2.30E-02	2.58E-02	2.53E-01
W-B	sec^(1/2)	3.4	0	5.69E-01	2.22	-6.20E-01	5.38
Goodness of Fit		1.61E-03		3.74E-04		8.82E-04	

CHAPTER 6

SIMULATION RESULT

This chapter presents high-fidelity conjugate heat transfer simulations that are used to model a micro-channel heat exchanger (MCHE) in a crossflow to study its thermal-hydraulic performance. The first part of this study considers three different microchannel geometries (circular, triangular, and square) with louver shape fin. Then discuss the temperature and velocity distribution of the computational domain's major regions, which includes cross-flow, solid and microchannel regions. This study aims to identify the suitable microchannel geometry in terms of heat exchanger effectiveness ε and performance index η. This work's second or final part considers three fin geometries (louver, step, and saw) with the same circular shape microchannel and identifies the corrosion hot spot and thermal effectiveness. This section is divided into two parts.

1. Identification of thermally effective microchannel.

2. Identification of corrosion hot spots for different fin geometries

6.1   Identification of Thermally Effective Microchannel

Figures 4-25 and 4-26 in Chapter 4 depict the schematic diagram and computational domain. The main parameters that characterize the flow are dimensionless velocity and pressure drop Δp along the length of the micro heat exchanger. The main parameters that characterize heat transfer are the dimensionless temperature for the hot (water) and cold (air) fluid, dimensionless temperature for solid, heat transfer rate, microchannel heat exchanger effectiveness ε and performance index will be discussed.

6.1.1   Crossflow Analysis

Figure 6-1 shows the velocity contour in the crossflow at several x locations, marked in Figure 6-2. It should be noted that MCHE is located between x=0 and x=0.07 inches. As the flow travels over MCHE, a separated flow region forms on the tube (see Fig. 6-1(a-c)). The

49

thickness of the separated region fluctuates in the spanwise direction such that a larger separated region is formed in region A, trapped by each fin, than in region B located in the gap between two consecutive fins. The spanwise variation of the wake field is due to the interaction of fins with the flow field, proving lower velocity in region A than B. The velocity far from the solid surfaces shows higher velocity compared to the inlet velocity. The velocity increases due to the simultaneous effect of blockage and the formed boundary layer on the solid surfaces.

As the airflow travels downstream the MCHE, a large wake region is observed, as shown in Figures 6.1(d-f). In this larger wake region, the Kelvin–Helmholtz instability of finite amplitude is observed.
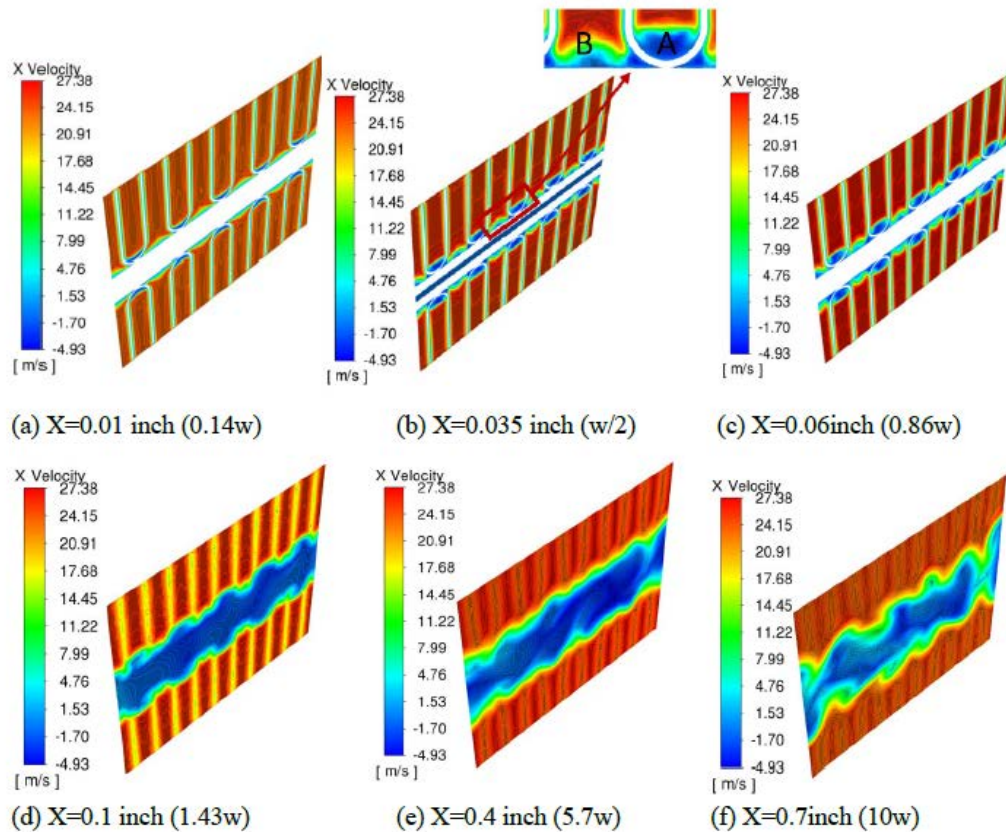

Figure 6.1: Velocity contour of crossflow for circular MCHE at different X locations

Figure 6.2 shows the crossflow at the midplane. Before MCHE, the flow velocity is uniform and similar to the inlet velocity. However, as the flow encounters the MCHE, the flow separation occurs at the contact point between the crossflow and solid tube such that the solid

tube becomes immersed in the separated flow region. In addition, the crossflow velocity increases around the MCHE due to both the blockage effect and the formation of the separated region near the MCHE. The crossflow velocity is largest at x=2.5w, where the wake thickness is the largest.
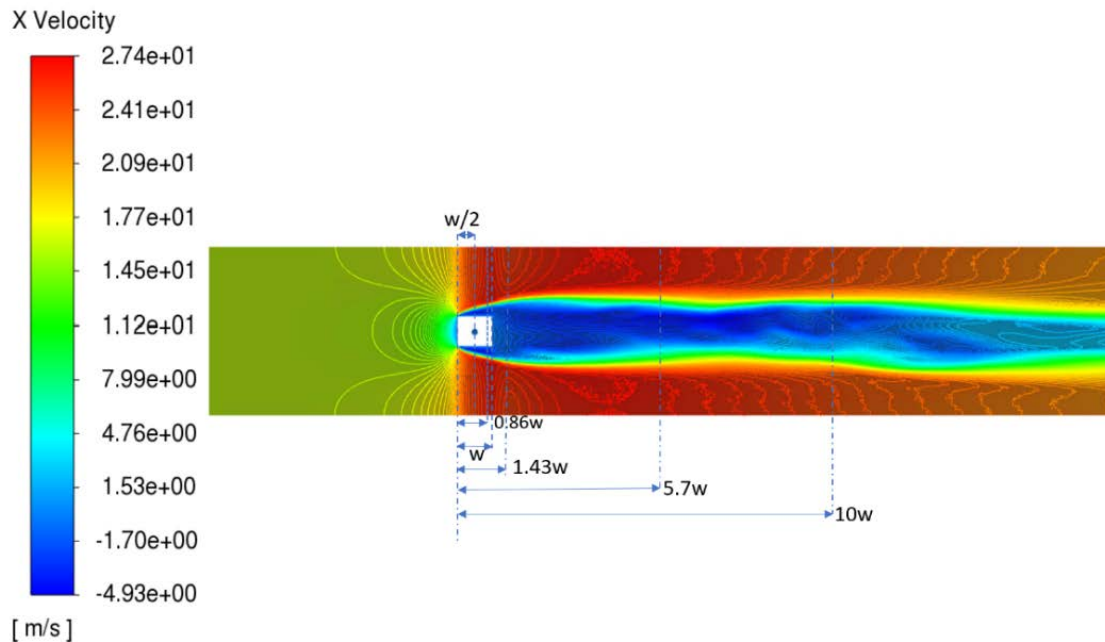

Figure 6.2: Velocity contour of crossflow for circular MCHE at the center plane.

Figure 6-3 shows the temperature contour in the crossflow. Around the MCHE (Figure 6-3(a-c)), the crossflow temperature increases near the solid surface due to hot water passing through the microchannel. The thermal boundary layer increases as the flow travels over the tube as the separated region's thickness increases (refer to Figure 6-2). The thermal boundary layer thickness fluctuates in the spanwise direction such that the thickness is larger in region A than B, following similar trends observed for the velocity field. The temperature of the crossflow drops as the flow travels downstream, reaching the inlet air temperature, $T_a = 26.85$ °C.

Figure 6-4 illustrates streamwise velocity at four lines (P1 to P4) at different y locations. Details of the P location is shown in a schematic diagram of Figure 6.4, where the height (y value) of P1=0.18 inch, P2=0.12 inch, P3=0.08 inch, and P4=0.06-inch. In Figure 6-4(a), those

lines are parallel to the x-axis (the direction of the crossflow), while Figure 6-4(b) shows the

streamwise velocity distribution along lines in the direction of the z-axis (spanwise direction).

(a) X=0.01-inch (0.14w)   (b) X=0.035-inch (w/2)   (c) X=0.06-inch (0.86w)

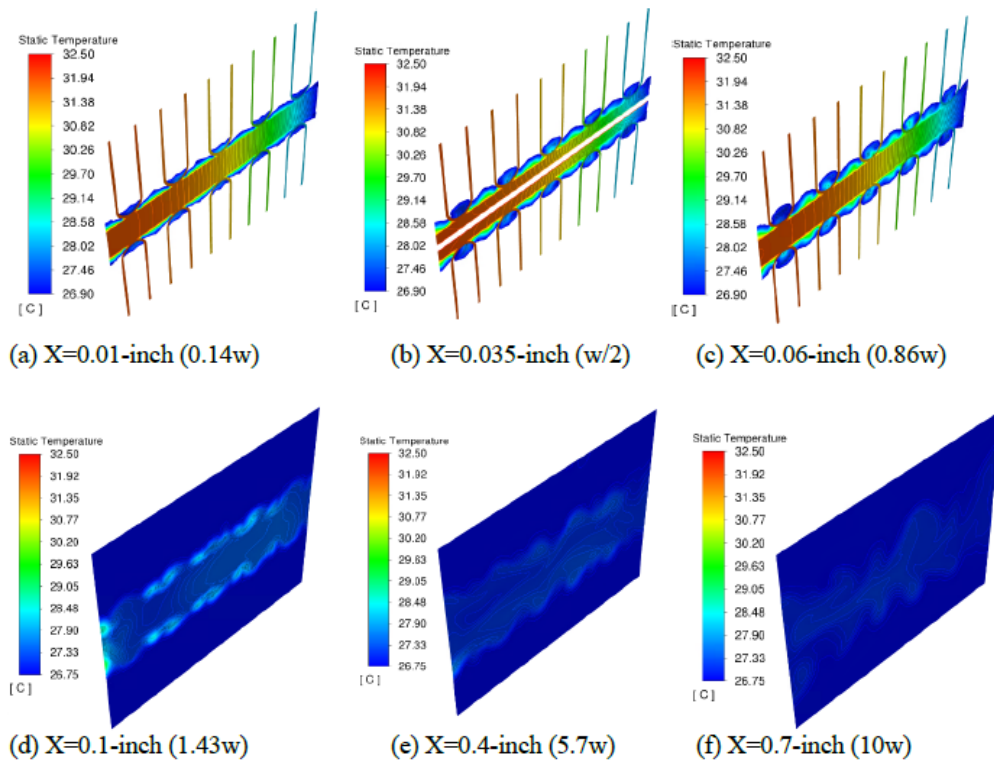(d) X=0.1-inch (1.43w)   (e) X=0.4-inch (5.7w)   (f) X=0.7-inch (10w)

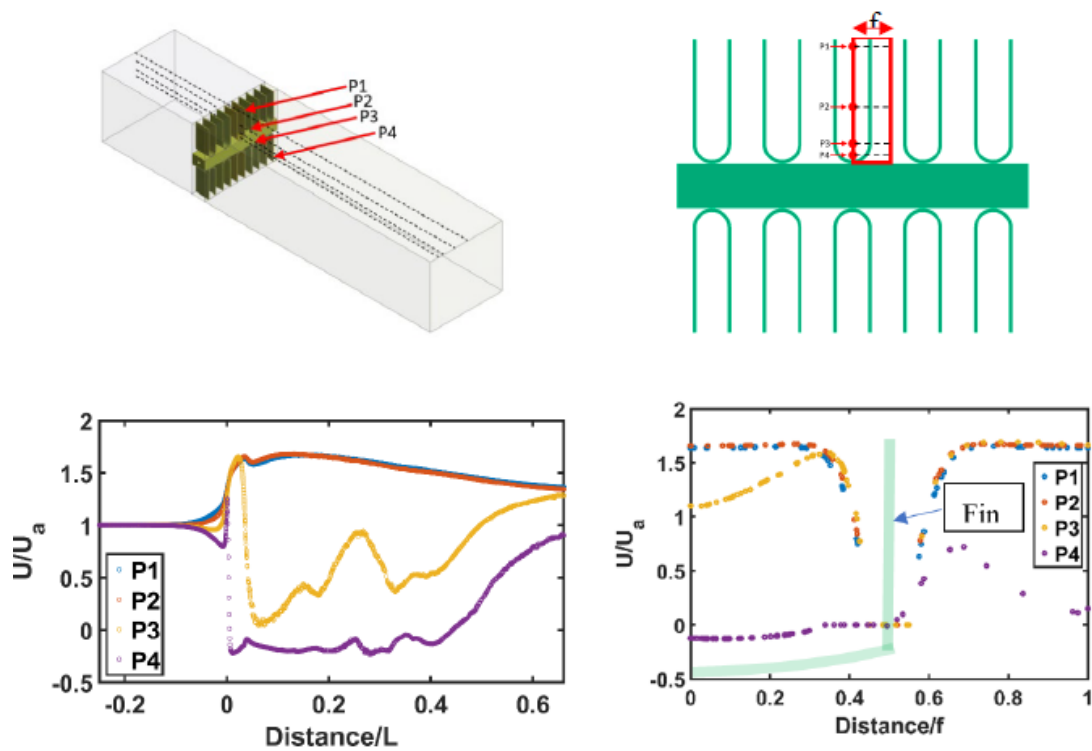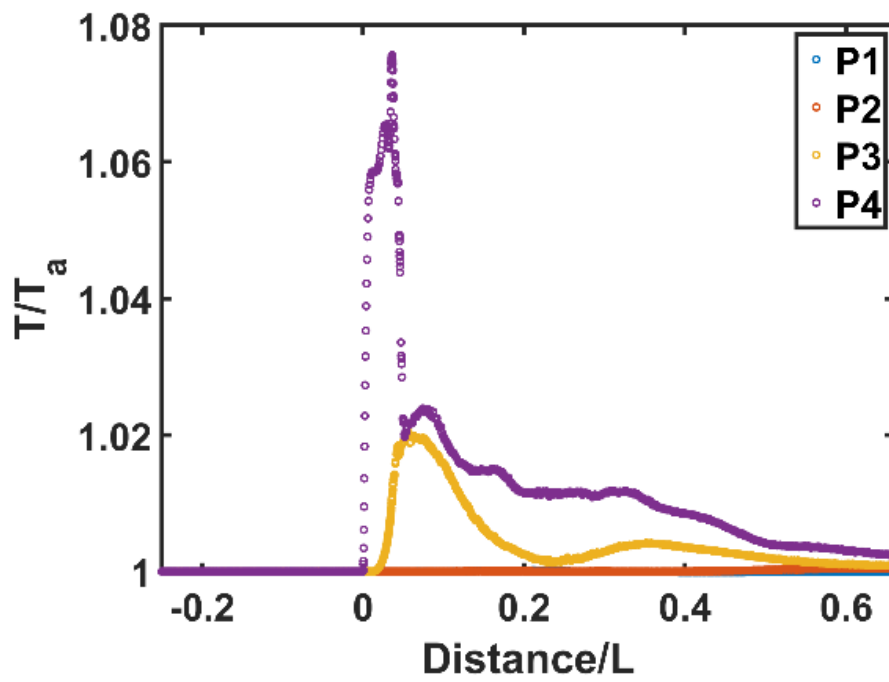**Figure 6.3: Temperature contour of crossflow for circular MCHE at different X location.**

Figure 6.4: Velocity flow distribution of crossflow for circular MCHE at P1, P2, P3 and P4 locations along (a) streamwise direction, and (b) spanwise direction

In Figure 6-4 (a), it is clear that the velocities along all those lines are close to the inlet velocity at upstream. As the flow travels within the fins, the velocity increases to about 1.6 times larger than the inlet velocity and then drops significantly for P3 and P4 and reduces slightly for P1 and P2 as the flow travels downstream. The profound velocity drop for P3 and P4 reveals those two lines are located inside the wake region at downstream of the heat exchanger. Figure 6.4(b) shows the streamwise velocity on the line passing P1 is largest at the point away from the fin surface and decreases dramatically to zero on the fin's surfaces. The velocity pattern is symmetric with respect to the fin's surface, i.e., the velocity profile is similar on both sides of the fin. A similar pattern is observed along the line passing P2. The velocity on the line passing P3 shows different distributions on different sides of the fin and the velocity is lower where the boundary layer is thicker (see region A in Figure 6.1). Velocity at P4 also reveals an asymmetric velocity profile with low velocity in the thick boundary layer formed in region A.

Figure 6.5 illustrates the temperature at four lines (P1 to P4) at different y locations. In Figure 6.5(a), those lines are parallel to the x-axis (the direction of the crossflow), while Figure 6.5(b) shows the temperature distribution along lines in the direction of the z-axis (spanwise direction). In Figure 6.5(a), it is clear that the temperature along those lines is initially close to the inlet temperature at upstream. As the flow travels within the fins, the temperature increases by about 7.8% at P4 and 2.1% at P3 locations. However, it stays relatively constant along the lines passing points P1 and P2 since they are located far from the heat exchanger. Figure 6.5(b) shows that the temperature on the line passing P4 is the largest since it is the closest point to the solid. The temperature on line P4 near the fin surface is 16% more than the inlet temperature and drops on both sides of the fin asymmetrically to a temperature about 7-8% more than the inlet temperature. As one moves from P4 to other lines, the crossflow temperature on the fin surface is relatively similar for all lines (16% more than the inlet temperature) but the

temperature far from the fin surface drops quickly to the inlet temperature at those lines as they are located far from the tube.

(a)
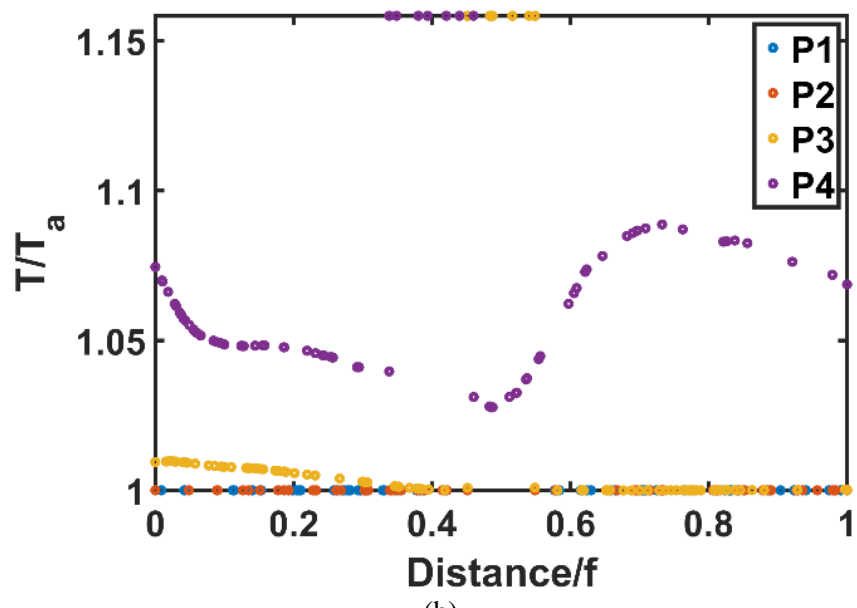
(b)

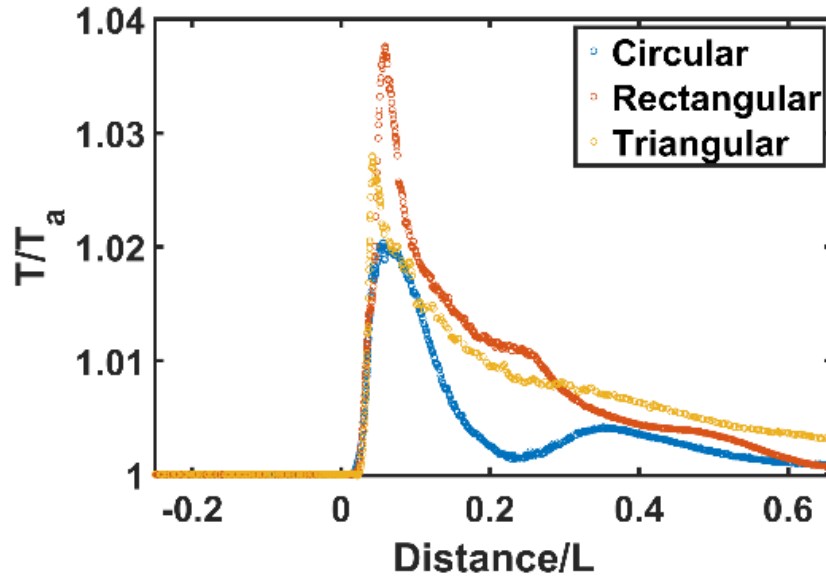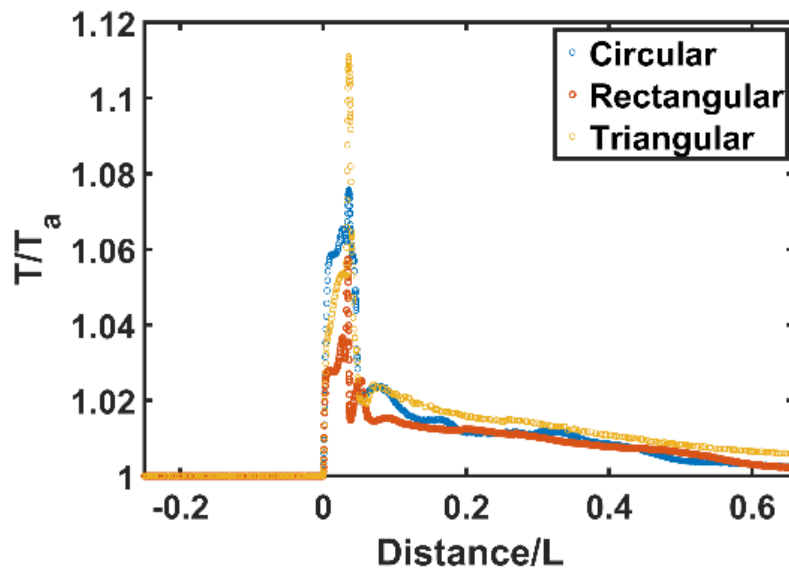**Figure 6.5: Temperature profile of crossflow for circular MCHE at P1, P2, P3 and P4 locations along (a) streamwise direction, (b) spanwise direction**

Figure 6.6 illustrates the crossflow temperature distribution from upstream to downstream along lines close to the solid surface (P3 and P4) for three different microchannel geometries. In Figure 6.6(a), it is clear that the temperature values of all lines are close to the

inlet temperature at upstream. At the P3 location, as the flow travels within the fins, the temperature increases about 3% for triangular MCHEs, while the increase is about 4% for the rectangular MCHE and 2% for circular microchannel.

a) P3 location

b) P4 location

Figure 6.6: Temperature profile of crossflow along streamwise direction for different MCHE geometries at (a) P3 location, and (b) P4 location

At location P4, shown in Figure 6-6 (b), temperature increases to 1.15 times more than the inlet temperature for triangular while the increase is about 8% for circular and 6% for rectangular MCHEs.

Figure 6-7 shows the temperature at P3 and P4 along lines in the spanwise direction. They show the temperature is highest near the fin surface, which is 16% more than the inlet temperature. At P4, the temperature at points far from the fin surface is similar for all three geometries while P3 shows slight changes in the temperature at points far from the fin surface among different geometries.

a) P3 location
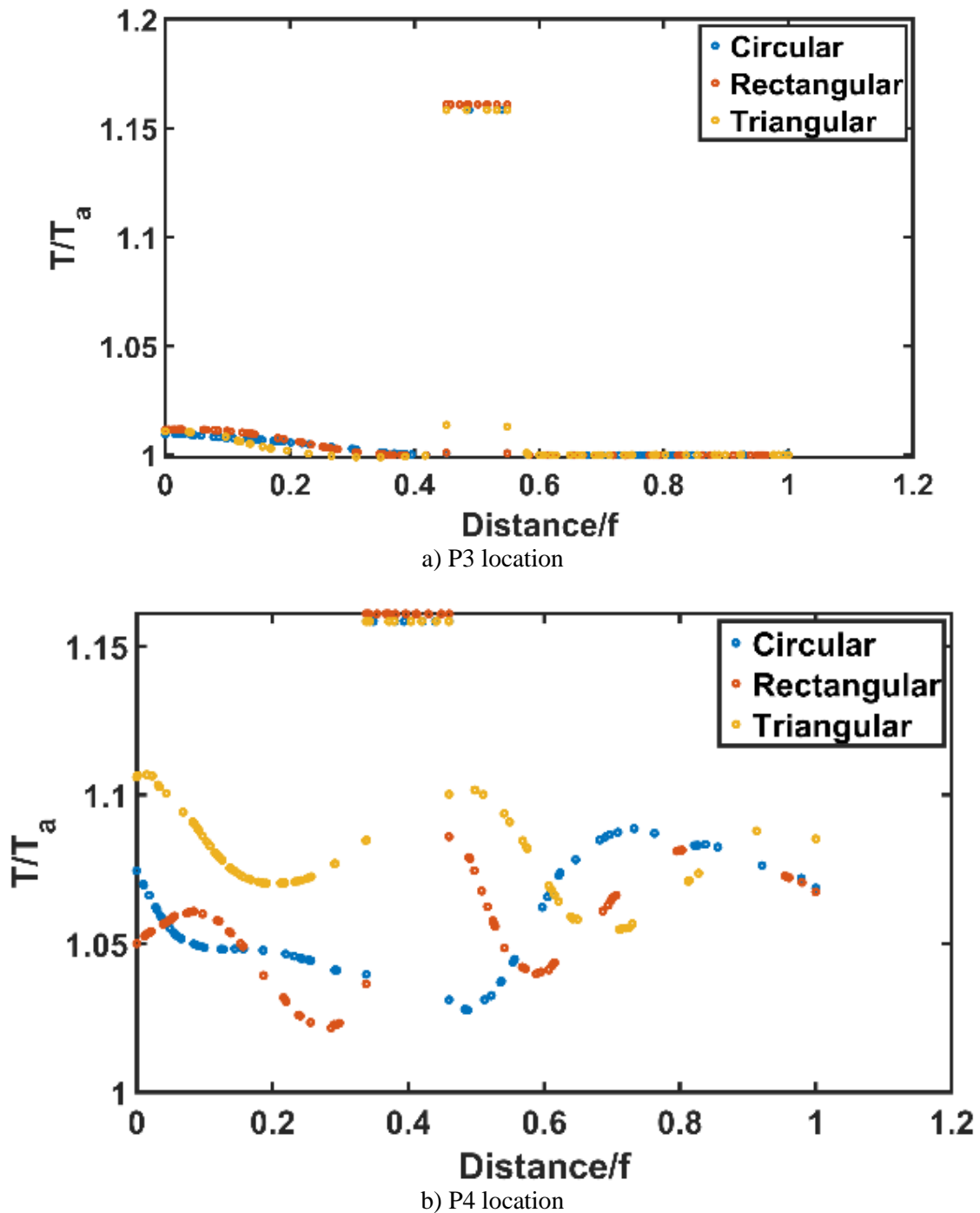
b) P4 location

Figure 6.7: Temperature profile of crossflow along spanwise direction for different MCHE geometries at (a) P3 location, and (b) P4 location

6.1.2   Solid Domain Analysis

Figure 6-8 illustrates two lines, one located at the backside surface of the tube and another located on the top surface of the tube. The temperature profile on the backside line in Figure 6-8(a) shows the tube temperature increases from the initial temperature as the water flows in the microchannel. The increase in the tube temperature is about 18% for all MCHEs. Figure 6-8(b) reveals the temperature is relatively uniform at the mid-section of the tube, with a slightly higher temperature predicted for rectangular MCHE and a slightly lower temperature for triangular MCHE.

(a)

(b)
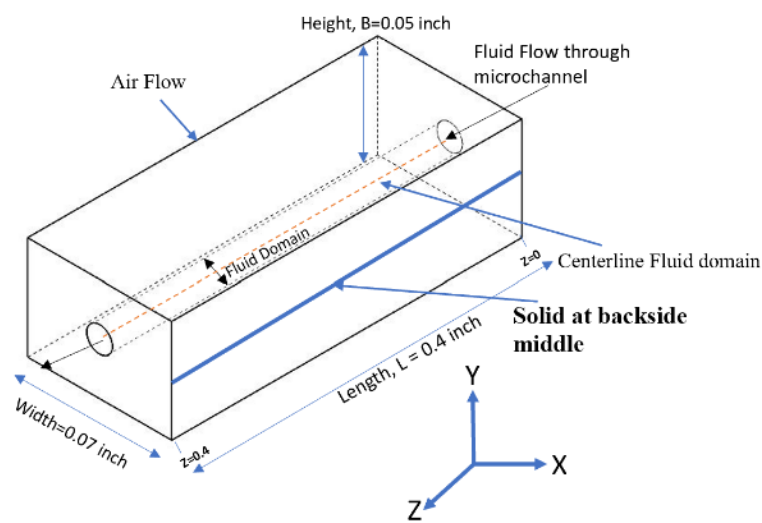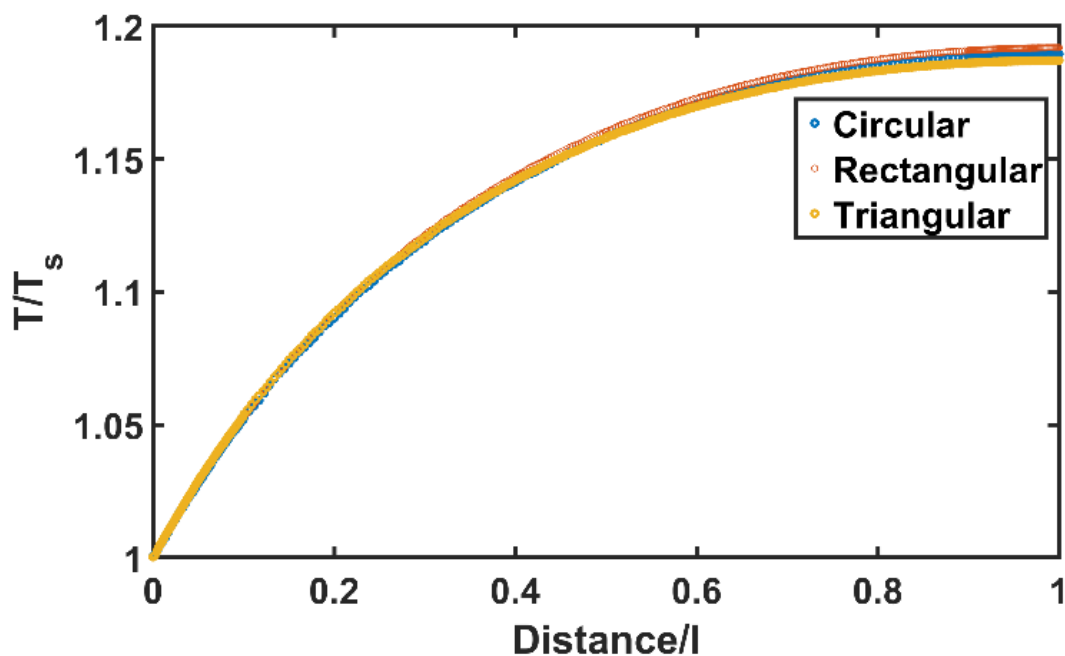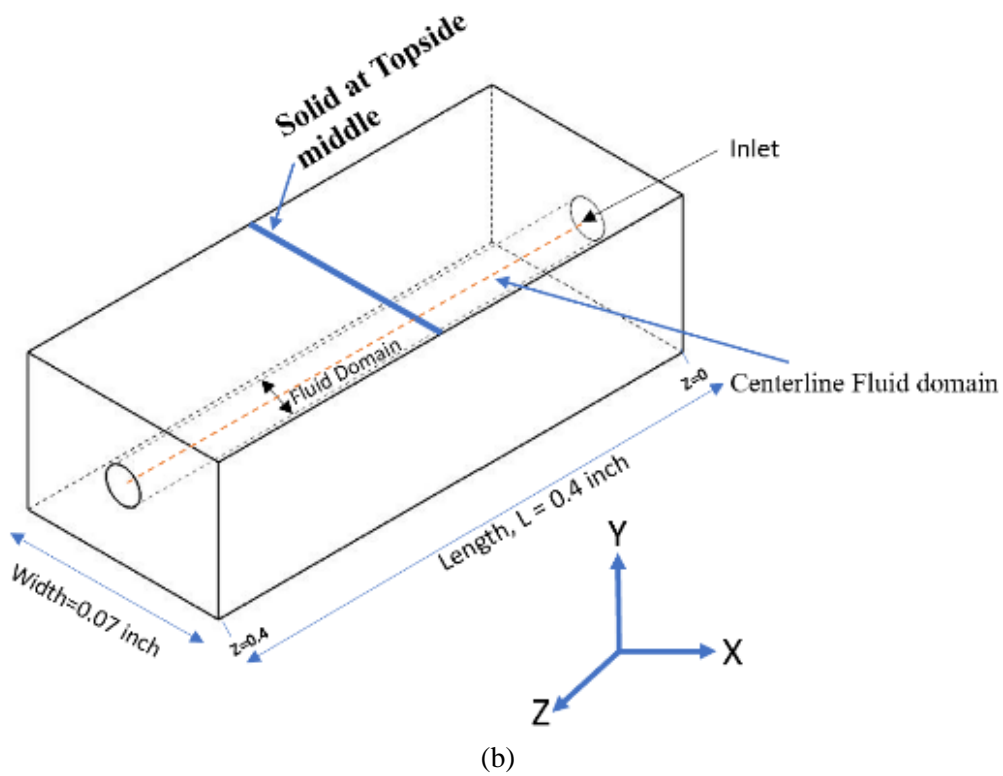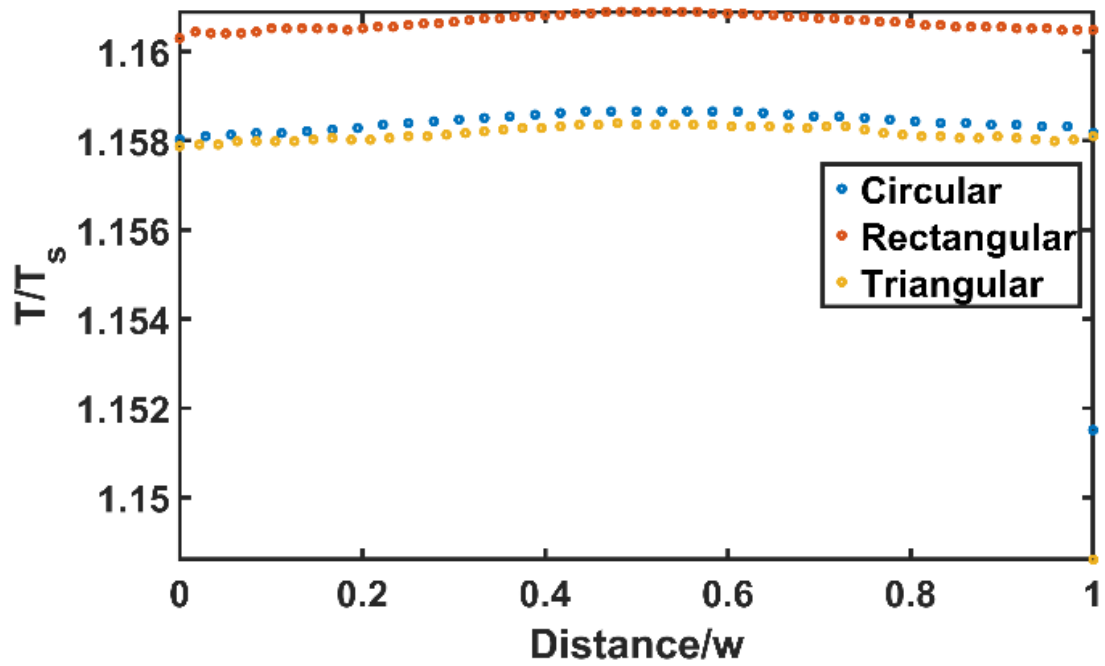
Figure 6.8: Temperature profile of tube at (a) backside middle, and (b) topside middle.

Figures 6.9 and 6.10 illustrate the temperature contour on the tube, fins, as well as microchannel surfaces for all considered MCHEs. The temperature of the tube and microchannel surfaces is nearly 26.8°C (the inlet temperature) and increases as the solid domain gets exposed to the hot flow in the microchannel.

(a) Circular   (b) Rectangular   (c) Triangular
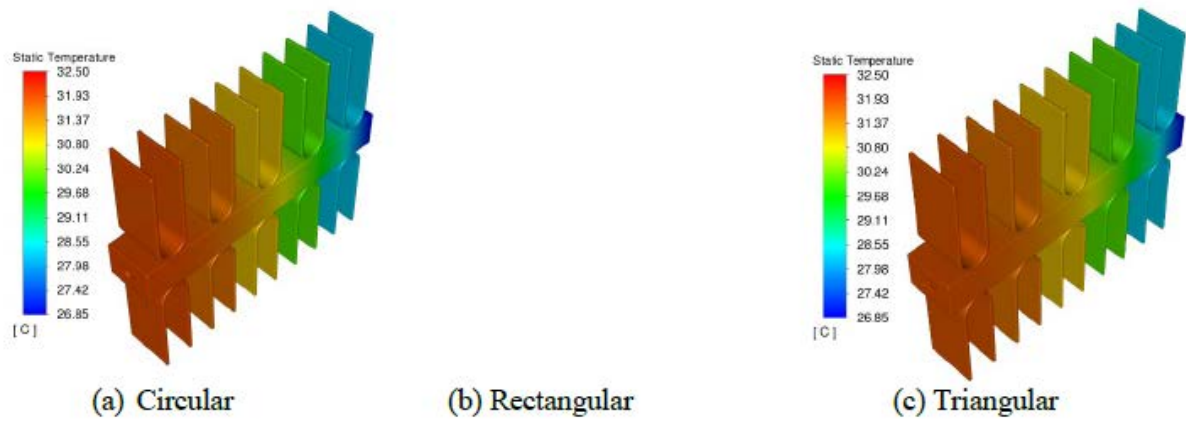
Figure 6.9: Temperature contour on different MCHE

(a) Circular   (b) Rectangular   (c) Triangular
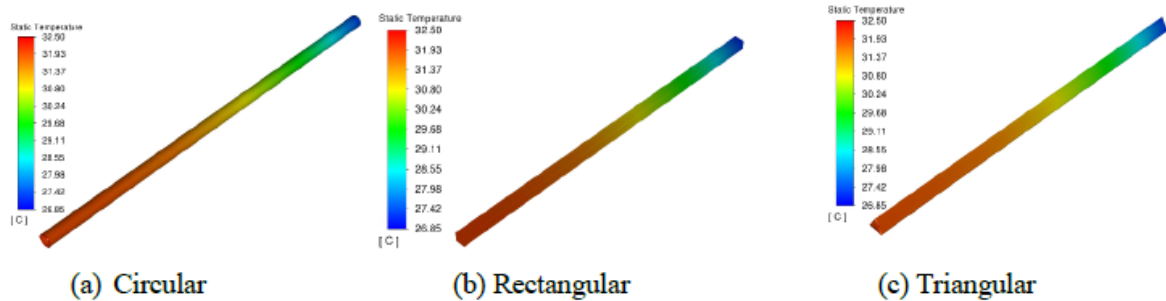
Figure 6.10: Temperature contour of the surface microchannel tube.

The fins also have the same temperature as the tube, due to the very high conductivity of aluminum, suggesting a similar thermal performance of all geometries.

6.1.3 Microchannel Analysis

Figure 6-11 shows the velocity, temperature, and pressure profile of the three microchannel geometries along their centerline. For circular microchannel, Fig. 6-11(a) reveals the centerline velocity increases and reaches to a fully developed condition with a constant velocity about twice the inlet velocity as expected after the flow travels about 10% of the pipe length. Other microchannels reach the developed condition at the same location. However, the central velocity is higher for triangular and smaller for rectangular microchannel compared to the circular microchannel.
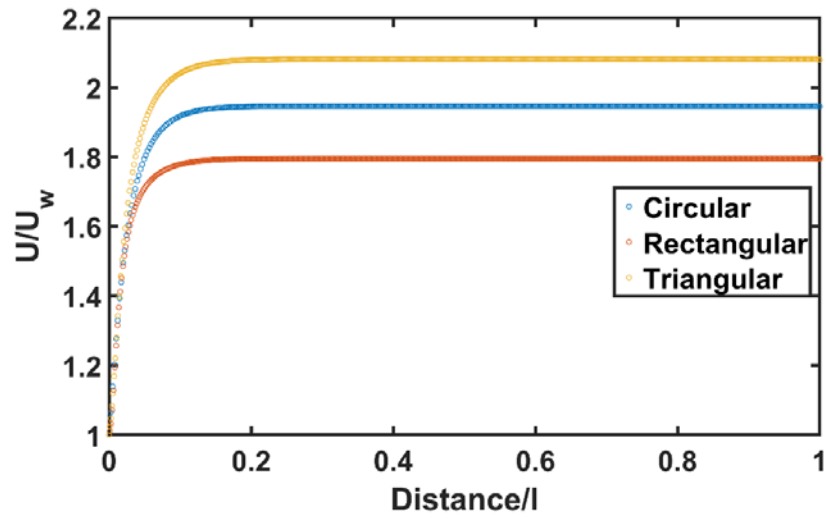
(a)Velocity profile
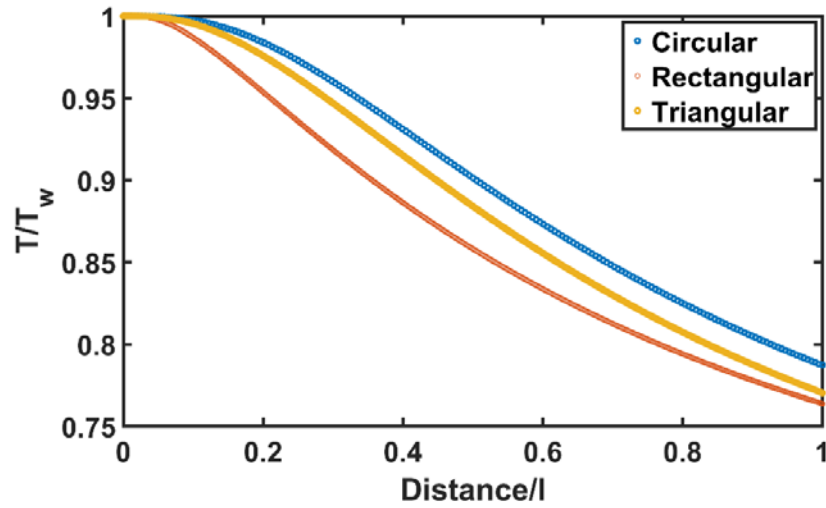
(b)Temperature profile
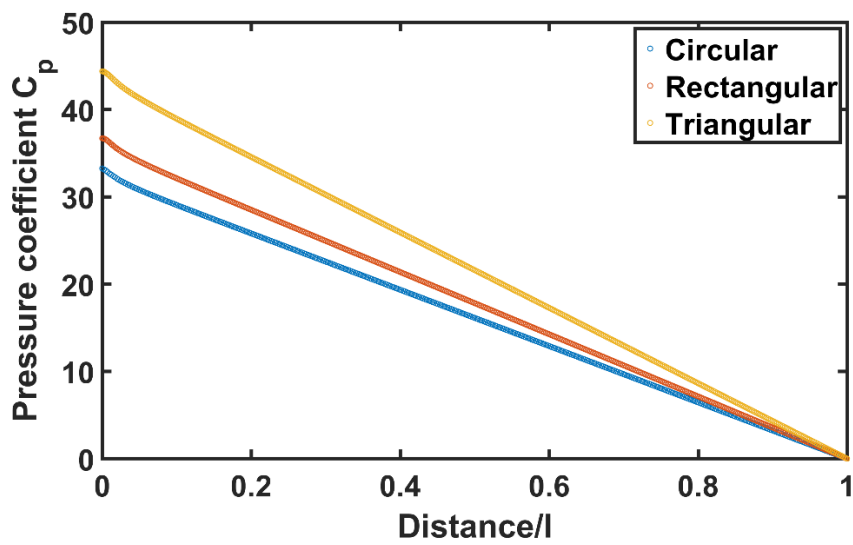
(c)Pressure profile

Figure 6.11: Velocity, temperature, and pressure distribution along centerline in the microchannel with different geometries.

It should be noted that all microchannels have the same cross-sectional area and the velocity change is purely due to the geometrical effects. Figure 6.11(b) reveals the temperature of the microchannel fluid drops by about 21-24% for all microchannels. The flow in the circular microchannel has a slightly higher temperature than other microchannels since it has a smaller surrounding surface. The pressure plotted in Figure 6.11(c) shows the highest drop for the triangular microchannel and the lowest for the circular microchannel, as expected.

Figure 6.12 shows the radial velocity, temperature, and pressure profile distribution for the three geometries. The temperature and velocity profile at the center of the midplane has the highest value and will decrease as moving from the center. However, the pressure profile remains the same, i.e., the pressure is uniform at each section of the microchannel.
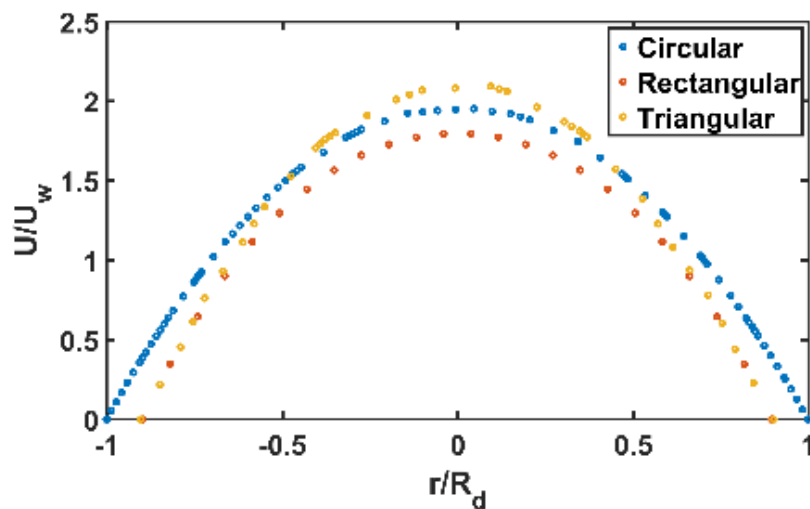
(a)Velocity Profile
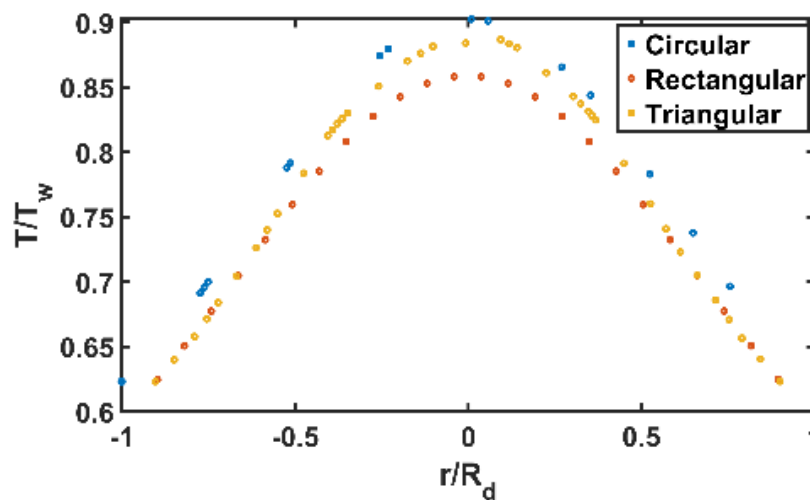
(b)Temperature Profile
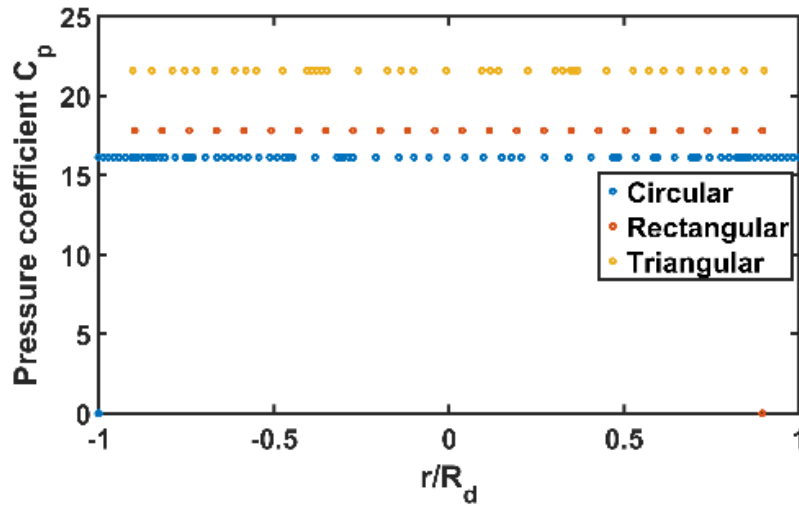
(c)Pressure Profile

Figure 6.12: Radial distribution of velocity, temperature, and pressure in microchannels with different geometries.

6.1.4   Effectiveness and Performance Index

Based on crossflow, solid domain, and microchannel analyses, the effectiveness and performance index for all geometries are computed using the below equations and results are listed in Table 6.1 computed from

$$\varepsilon_{circular\ channel} = \frac{q}{q_{max}} = \frac{C_h(T_{w,in}-T_{w,out})}{C_{min}(T_{w,in}-T_{a,in})} \qquad (6.1)$$

$$\eta = \frac{\varepsilon}{\Delta P} \qquad (6.2)$$

Table 6.1: Effectiveness and performance index of MCHE for different channel geometries

Microchannel Geometry	Effectiveness (ε)	Performance Index (η), ($\frac{m^2}{N}$)
Circular	0.467	6.91×10^{-4}
Triangular	0.497	5.79×10^{-4}
Rectangular	0.51	6.81×10^{-4}

Results show that the rectangular microchannel has the highest effectiveness and the circular microchannel has the lowest. On the other hand, the highest performance index value is observed for circular microchannel, while triangular microchannel has the lowest one.

6.2   Identification of Corrosion Hot Spots for Different Fin Geometries

This study considers three fin geometries (louver, step, and saw) with the same tube and circular shaped microchannel, identifies the corrosion hot spot, and thermal effectiveness. A predicted flow field also identifies crevices between fins and tube surfaces as critical corrosion hot spots often associated with low-velocity regions. The crevice volumes for the louver, step, and saw fin shapes are calculated.

Figure 6-13 illustrates the velocity contour of the whole computational domain. The flow separation occurs at the contact point between the crossflow (airflow) and the solid tube, so the solid tube is immersed in the separated flow region. Outside that region, the crossflow velocity increases by increasing the wake thickness until X=0.91 inch, then reducing the crossflow velocity. Figures 6.14 to 6.16 illustrates the velocity contour around the circular MCHE. At X=0.035 inch, zero or low velocity was observed in the boundary layer formed near the solid side tube. The boundary layer thickness varies along fin pitch such that a more extensive boundary layer is grew in region A trapped by each fin than in region B located in the gap between two consecutive fins. Due to the no-slip boundary condition, the solid and fin surface velocity is zero.
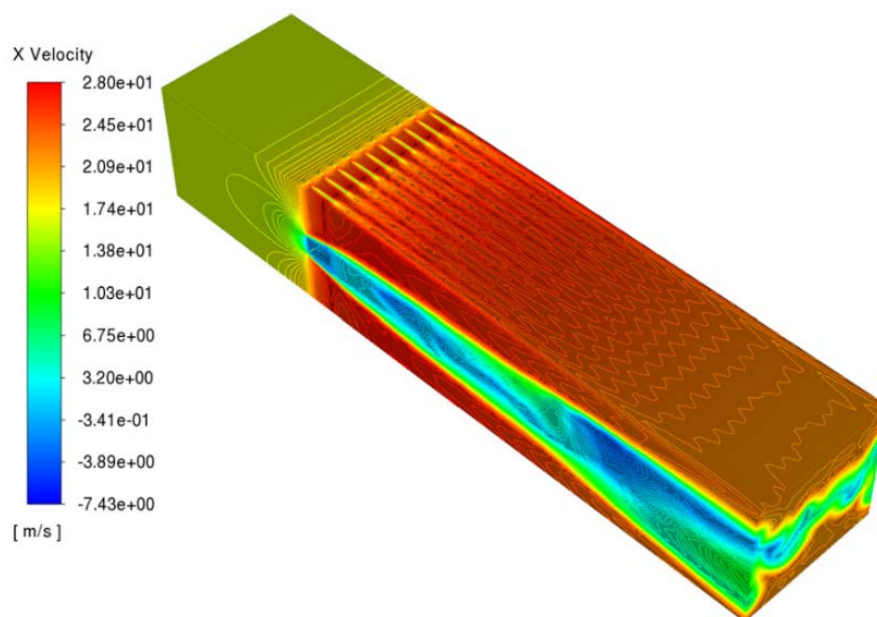
Figure 6.13: Velocity contour of the whole computational domain.
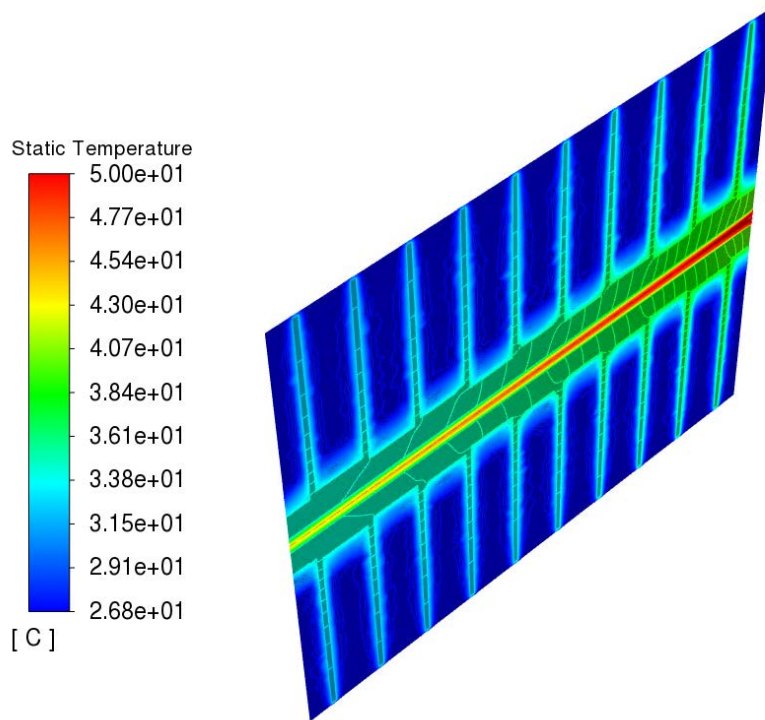
Figure 6.14: Temperature contour of the step shaped fin with circular microchannel.

Figure 6.15: Velocity contour of crossflow of the step shaped fin with circular MCHE at different X location (X=0.035 inch, X=0.4 inch and X=0.7 inch).
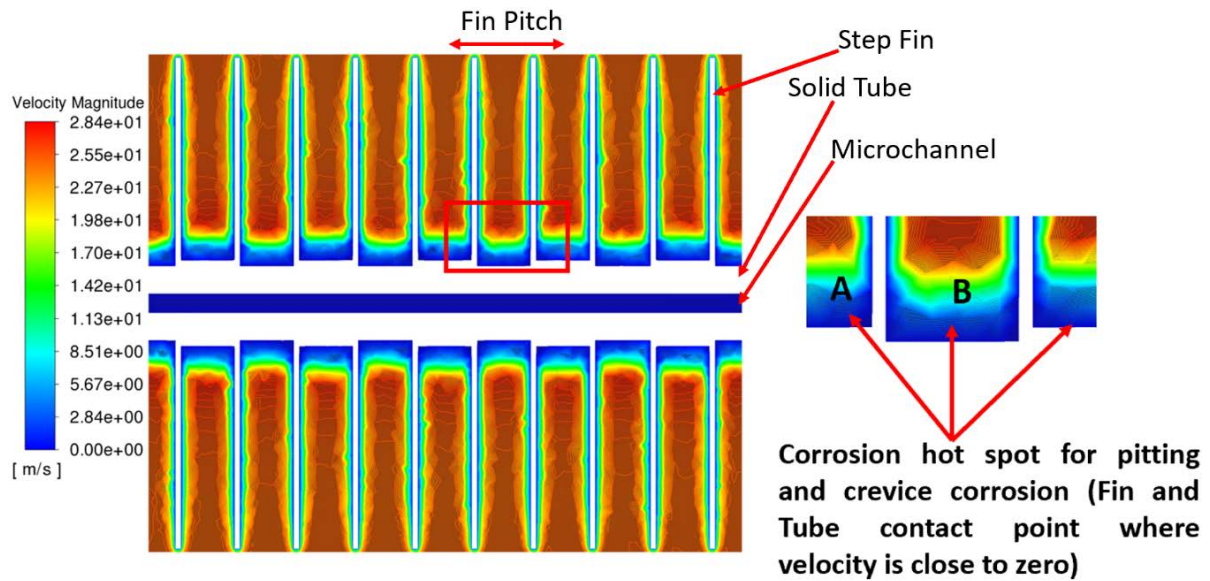
Figure 6.16: Stagnation region identification for step-shaped fin geometry at X=0.035 inch

As the crossflow travels far from the tube and fin, the velocity increases between the fin up to 28.4 m/s for Figure 6.15 and 6.17, and 28 m/s for Figure 6.18, which is around 70% higher than the inlet velocity. Table 6.3 describes the details of the boundary conditions. These low-velocity regions, A and B, is the hot spot for pitting and crevice corrosion.

Figure 6.14 shows the temperature contour of the step shaped fin with circular microchannel in the crossflow. Around the MCHE, the crossflow temperature increases near the solid surface due to hot water passing through the microchannel. Figure 6.15 shows the velocity contour in the crossflow at several x locations. As the flow travels over MCHE, a separated flow region forms on the tube.

Figure 6.17 and 6.18 illustrate the corrosion phenomena of the MCHE. Pitting and crevice corrosion are localized attacks that result in relatively rapid penetration at small discrete areas. The attack can often be controlled by ensuring that velocities are adequate to prevent stagnation or the accumulation of solids. Pitting corrosion is most likely to occur during shutdown periods when there is no flow, and the environment is most suitable for the buildup of concentration cells. From Figure 6.19, we observed that pitting corrosion occurs in the area near the fin and solid surface. Figure 6.19 shows the experimental work conducted in our lab,

which shows that crevice corrosion occurs at the junction between fin and solid surfaces. Scanning electron microscopy (SEM) was used to measure damaged areas in the corroded MCHE samples. After more than 104 days of exposure to a corrosive atmosphere within the corrosion chamber, MCHE samples were collected [119]. Figure 6.19 shows a corroded crevice area near the fin and solid junction. This condition contrasts with other types of failure like a vibration failure in which the metal is sharply cut without pits. Relatively zero velocity conditions must exist for crevice corrosion to occur. The attack can often be restrained by ensuring that velocities are sufficient to prevent stagnation.

Figure 6.16 to 6.18 highlights the fin pitch distance with a red box. Inside the red box, low velocity is observed at the contact point of the fin and solid tube surface. This low-velocity region is shown in the contour plot (Figure 6.14) as a blue color. The corrosion hot spot area can be determined by determining the area of this blue region for only fin pitch area within the red box in Figure 6.16. Our result shows that saw shaped fin has more hot spot volume on top surface of the solid which is $3.508 \times 10^{-3} inch^3$. The hot spot volume for the louver and step shape fin are $2.719 \times 10^{-5} inch^3$ and $3.297 \times 10^{-5} inch^3$.
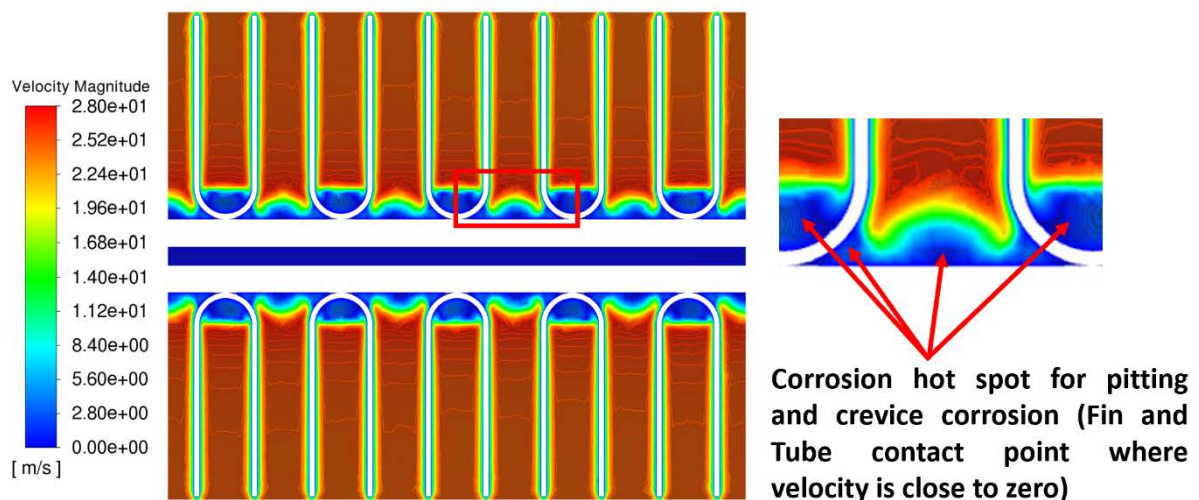
Figure 6.17: Stagnation region identification for louver shaped fin geometry at X=0.035 inch
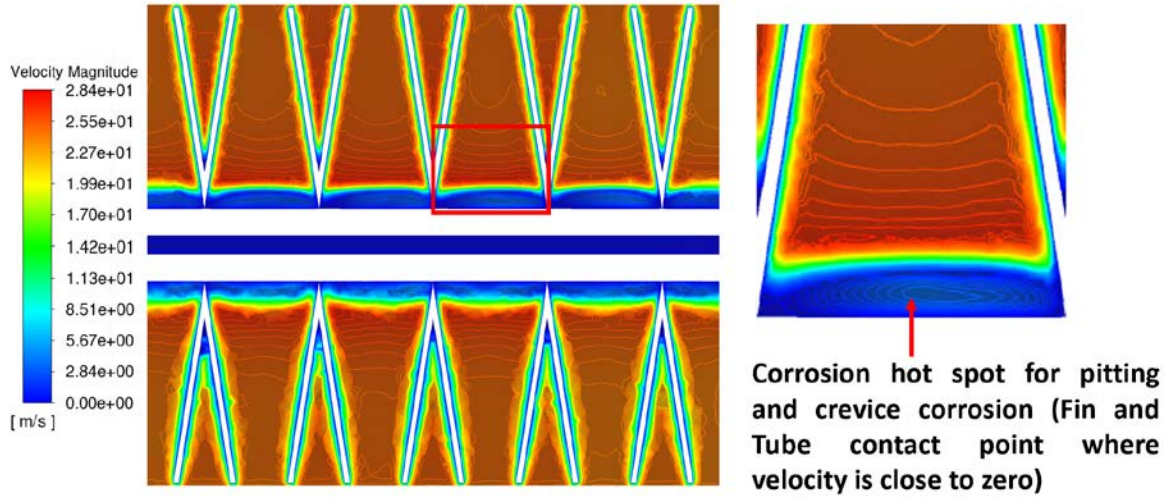
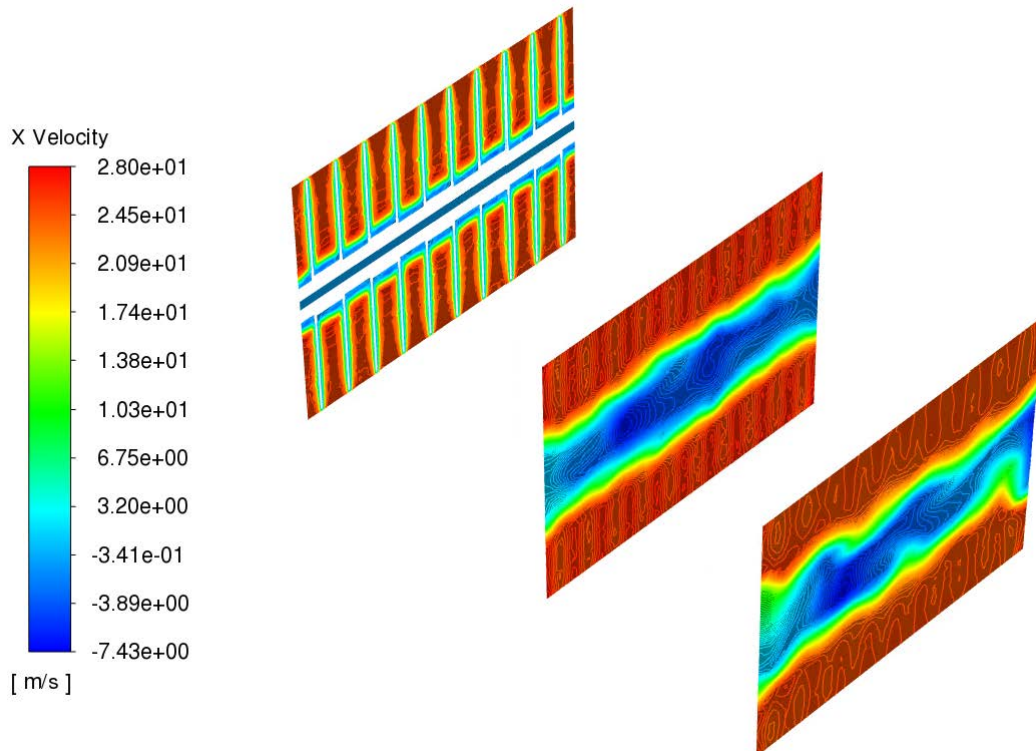**Figure 6.18: Stagnation region identification for Saw shaped fin geometry at X=0.035 inch.**
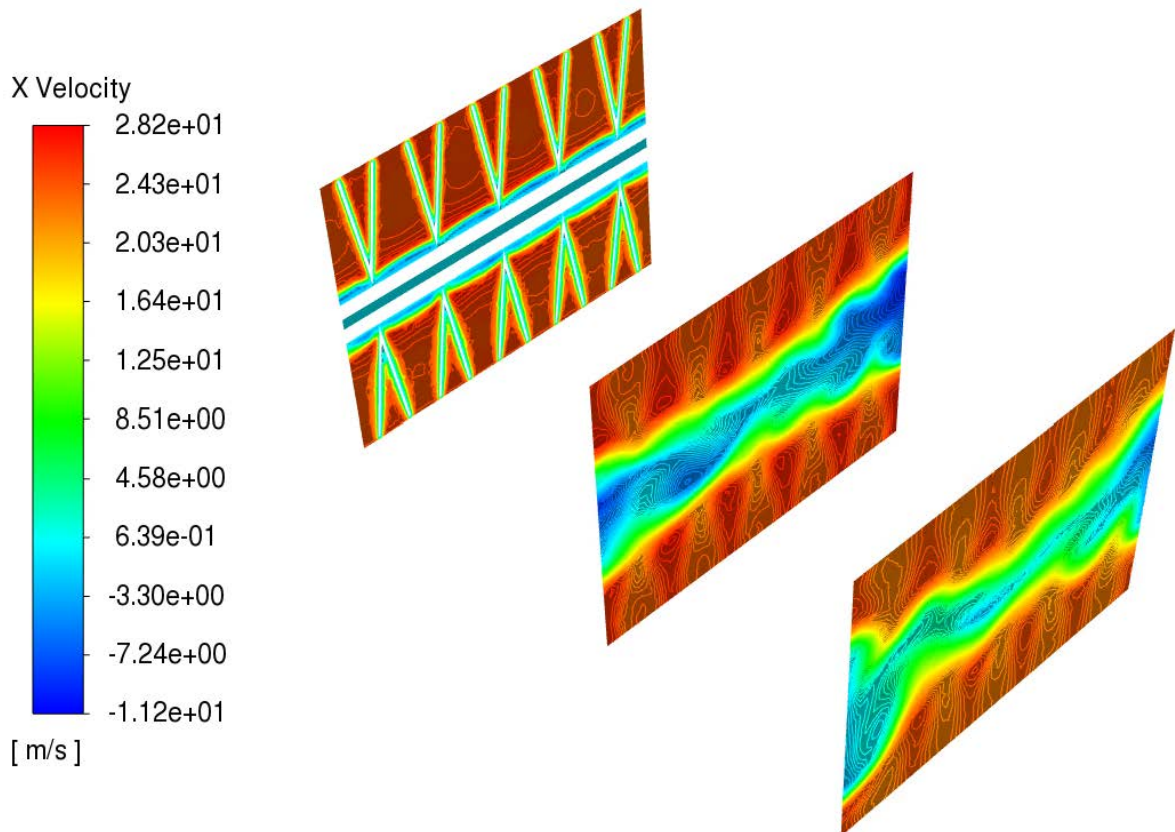
Figure 6.19: Velocity contour of crossflow of the saw shaped fin with circular MCHE at different X location (X=0.035 inch, X=0.4 inch and X=0.7 inch).

Figure 6.19 shows the velocity contour in the crossflow at several x locations for a saw shaped fin.

Figure 6.20 shows the velocity, Temperature, and pressure profile of fluid domain through the centerline of circular MCHE for different fin geometries. For a louver-shaped fin,

the microchannel has the highest temperature drop, about 7.8 ˚C, while all geometries have almost the same pressure drop, about 670 to 675 Pa, from upstream to downstream. The highest velocity value observed in step and saw fin geometries is 0.385 m/s. The value of the Reynolds number is around 78.9, and the hydrodynamic entry length is 0.049 inches. From the velocity profile of Figure 6-18, it is observed that after 0.049 inches, the flow is fully developed.
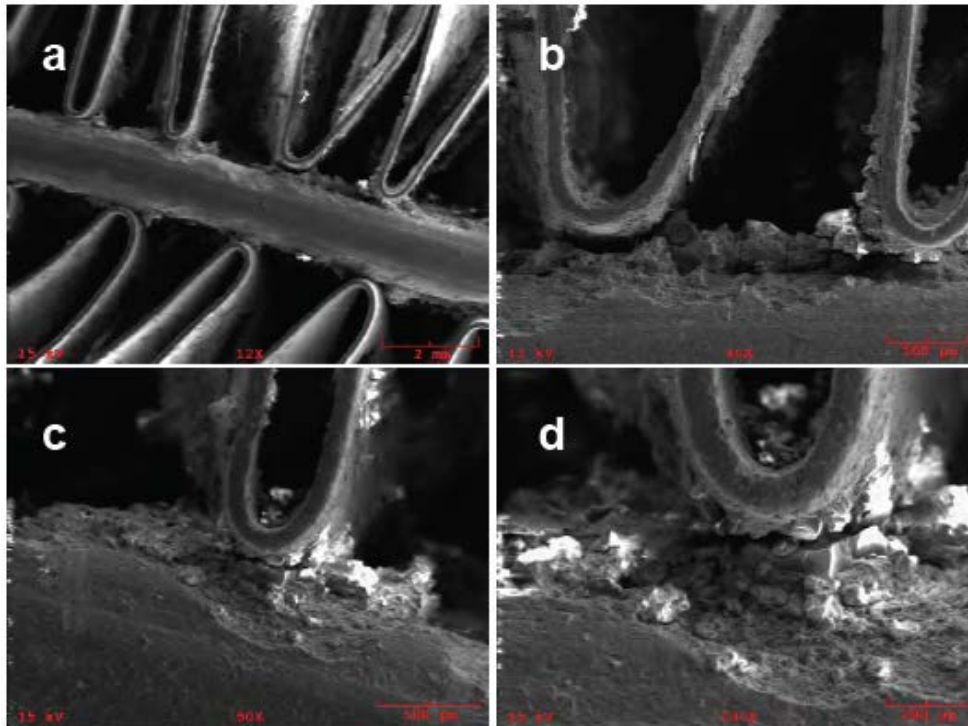
Figure 6.20: SEM micrographs of MCHE sample after around 104 days of exposure to corrosive electrolyte [119]

A circular microchannel is used in this work for three different fin geometries. Hot water is flowing through the microchannel. The density of the water is 998.2 kg/m^3 and specific heat $C_p = 4182 \frac{J}{kg\,k}$ is used in simulation.

Heat exchanger effectiveness is the proportion of actual heat transfer to the maximum possible heat that can be transferred. The value of $T_{h,out}$ can be calculated from Figure 6.21 (b).

$$\varepsilon_{circular\ channel} = \frac{q}{q_{max}}$$

$$= \frac{C_h(T_{w,in} - T_{w,out})}{C_{min}(T_{w,in} - T_{a,in})} \qquad (6.3)$$
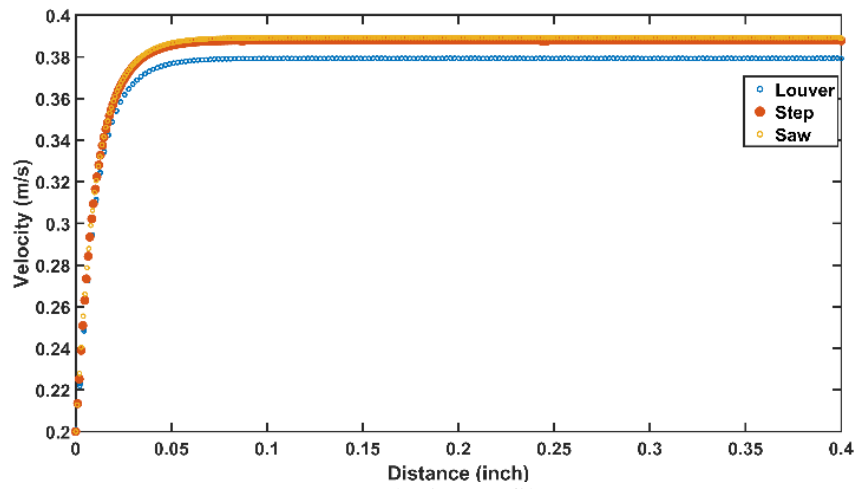
(a) Velocity Profile
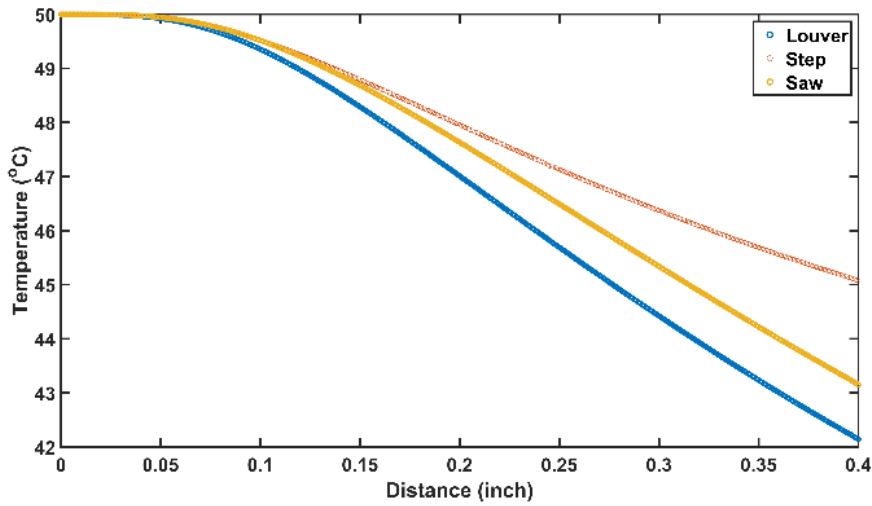
b) Temperature Profile
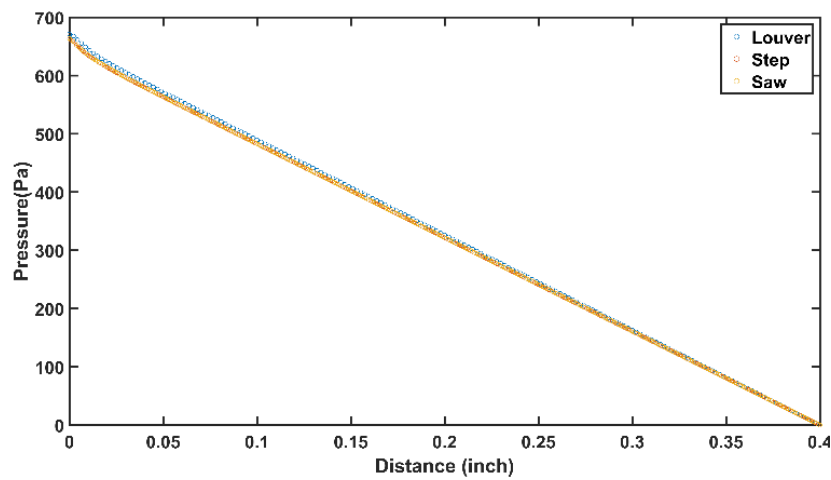
c) Pressure Profile

Figure 6.21: Velocity, Temperature, and pressure profile of fluid domain through the centerline of circular MCHE for different fin geometries.

Table 6.2 presents the thermal performance of tubes with fins of louver, step, and saw geometries indicating louver find with the highest and step geometry with the lowest thermal effectiveness.

Table 6.2: Effectiveness of MCHE for different fin geometries

Fin Geometry	Effectiveness (ε)
Louver	0.337
Step	0.20737
Saw	0.2895

CHAPTER 7

CONCLUSION AND FUTURE WORK

7.1   Conclusion

The present work mainly aimed to compare the compact heat exchangers with three different microchannel shapes (Circular, Triangular, and Square). A comparison of heat transfer effectiveness and pressure drops in single-phase heat transfer has been made. Unlike previous studies in the literature, the temperature or heat flux on the pipe wall is not assumed to be constant. The solid domain, microchannel flow, and crossflow field were tightly coupled to predict the temperature on the solid surfaces and the variation of the crossflow around the solid. Local flow field studies showed a significant variation of velocity and temperature in the crossflow. The temperature in the solid domain was non-uniform in the spanwise direction due to the change in the hot flow temperature in the microchannel. However, it was relatively uniform in each section due to the high conductivity of aluminum. The results showed that the circular MCHE achieves the best performance based on microchannel pressure drop, while a higher heat transfer effectiveness is shown for rectangular MCHE. A numerical investigation of the effects of corrosion to fin-and-tube All Aluminum MCHE with different fin geometries was performed in this study. This study considers the outside airflow to predict the corrosion hot spot and shows the pitting and crevice corrosion area. This study will help design a better fin shape in terms of corrosion aspect and thermal effectiveness. All three different fin geometries use the same boundary condition and the same internal microchannel geometry. This model also predicted the heat exchanger microchannel side pressure drop and the temperature and velocity profile. The result shows that a louver shape is the best option for a circular microchannel with less corrosion hot spots and higher thermal effectiveness. Crossflow shows higher temperatures near the boundary layer of the tube, which results in higher corrosion rates. A predicted flow field also identifies crevices between fins and tube surfaces

71

as critical corrosion hot spots often associated with low-velocity regions. The crevice volumes for the louver, step, and saw fin shapes are calculated as $2.719 \times 10^{-5}\ in^3$, $3.297 \times 10^{-5}\ in^3$ and $3.508 \times 10^{-4}\ in^3$ respectively.

Since EIS is a non-destructive test, there were no significant visual signs of corrosion on the tested sample. However, EIS measurements indicated significant physical changes within the Zn coating. Overall, the results are consistent with the idea that Zn coating systems protect aluminum alloys since Zn is anodic to aluminum on the galvanic series. In addition, the highest Rp value is observed on high chloride concentrations with lower pH. An inductive loop was observed at the low-frequency region for the SWAAT solution.

7.2   Future Work

The present study has produced results considering steady state, compressible flow, and certain boundary conditions. In the future, researchers can extend this work to the following cases:

- This work can be formed for turbulent, compressible flow and considering the effect of gravity. The numerical investigation for the turbulent model can be considered using Reynolds Stress Turbulence Model or other suitable models.

- The present work can be conducted for unsteady flow.

- Multiphase flow can be developed instead of single-phase flow through the microchannel.

- Add polymer-coated AA 3102 and do EIS testing to show that electrochemical testing can produce fast and reliable results/guide for future heat exchanger and coating system design. However, the balance between the protective coating and the alloy's thermal performance needs to be considered.

- Flat tubes are crucial in various technical applications like automotive radiators and HVAC systems. Flat tube heat exchangers are expected to have smaller air-side pressure drop

and improved air-side heat transfer coefficients than round tube heat exchangers. So, the optimum spacing with the maximum overall heat transfer rate and minimum pressure drop needs more focus and research in the future. In addition, more work is needed to develop the thermos-fluid correlations in tubes of this shape.

REFERENCES

[1]   C. S. Chen, W. J. Kuo, Heat transfer characteristics of gaseous flow in long mini-and microtubes, Numerical Heat Transfer, Part A: Appl. 46 (2004) 497-514. https://doi.org/10.1080/10407780490463773

[2]   G. Maranzana, I. Perry, D. Maillet, Modeling of conjugate heat transfer between parallel plates separated by a hydrodynamically developed laminar flow by the quadrupole method, Numer. Heat Transfer, Part A: Appl. 46 (2) (2004) 147-465.https://doi.org/10.1080/10407780490457572

[3]   H. S. M. Faghri, Effects of rarefaction and compressibility of gaseous flow in microchannel using DSMC, Numerical Heat Transfer: Part A: Appl. 38 (2) (2000) 153-168. https://doi.org/10.1080/10407780050135388

[4]   H. Sun, M. Faghri, Effect of surface roughness on nitrogen flow in a microchannel using the direct simulation Monte Carlo method, Numerical Heat Transfer: Part A: Appl. 43(1) (2003) 1-8. https://doi.org/10.1080/10407780307302

[5]   A. Beskok, Validation of a new velocity-slip model for separated gas microflow, Numer. Heat Transfer, Part B: Fundam. 40 (6) (2001) 451–471. https://doi.org/10.1080/104077901753306593

[6]   C. Yang, J. Wu, H. Chien, S. Lu, Friction characteristics of water, R- 134a, and air in small tubes, Microscale Thermophys. Eng. 7 (2003) 335–348. https://doi.org/10.1080/10893950390243608

[7]   H. W. Swidersky, Aluminium brazing with non-corrosive fluxes-state of the art and trends in NOCOLOK® flux technology, DVS BERICHTE 212 (2001) 164-169.

[8]   H. Zhao, S. Elbel, P. S. Hrnjak, Transport phenomena involved in controlled atmosphere brazing of microchannel aluminum heat exchanger, International Refrigeration and Air Conditioning Conference at Purdue (2010) 12-15.

[9]   H. M. Hasan, Numerical simulation of parallel flow microchannel heat exchanger with isosceles right triangular geometry, (2009) (Doctoral dissertation, MSc Thesis, Engineering Collage, University of Basrah).

[10]   K. A. Yasakau, M. L. Zheludkevich, M. G. S Ferreira, Role of intermetallic in corrosion of aluminum alloys, Smart corrosion protection, In: Mitra, R. (ed). Intermetallic Matrix Comp. (2018) 425-462. DOI: 10.1016/C2013-0-16230-7

[11]   H. Bohni, Localized corrosion of passive metals, Uhlig's Corrosion Handbook, (2011) 157-169. DOI: 10.1002/9780470872864.ch13

[12]   R. T. Foley, Localized corrosion of aluminum alloys—a review, Corr. 42 (1986) 277-28. DOI: 10.5006/1.3584905

[13]   A. Seyeux, V. Maurice, P. Marcus, Breakdown kinetics at nanostructure defects of passive films, Electrochem, Solid-State Lett. 12 (2009). DOI: 10.1149/1.3186644

[14]   H. H. Strehblow, Nucleation and repassivation of corrosion pits for pitting on iron and nickel, Materials and Corr. 27 (1976) 792-799. https://doi.org/10.1002/maco.19760271106

[15]   K. V. Akpanyung, R. T. Loto, Pitting corrosion evaluation: a review, Journal of Physics: Conference Series 1378 (2019) 022088. DOI: 10.1088/1742-6596/1378/2/022088

[16]   R. T. Loto, Pitting corrosion resistance and inhibition of lean austenitic stainless steel alloys, In Austenitic Stainless Steels-New Aspects. IntechOpen, (2017). DOI:10.5772/intechopen.70579

[17]   S. K. Kairy, P. A. Rometsch, K. Diao, J. F. Nie, Exploring the electrochemistry of 6xxx series aluminium alloys as a function of Si to Mg ratio, Cu content, ageing conditions and microstructure, Electrochimica Acta. 190 (2016). 92-103 DOI:10.1016/j.electacta.2015.12.098

[18]   A. Pardo, E. Otero, M. C. Merino, M. D. López, M. V. Utrilla, F. Moreno, Influence of pH and chloride concentration on the pitting and crevice corrosion behavior of high-alloy stainless steels, Corr. 56(04) (2000).

[19]   Z. Szklarska-Smialowska, Pitting corrosion of aluminum, Corrosion sci. 41(9) (1999) 1743-1767.

[20]   G. T. Burstein, C. Liu, R. M. Souto, S. P. Vines, Origins of pitting corrosion, Corrosion Engineering, Science and Technol. 39(1) (2004) 25-30. https://doi.org/10.1179/147842204225016859

[21]   D. E. Williams, C. Westcott, M. Fleischmann, Stochastic models of pitting corrosion of stainless steels: I. Modeling of the initiation and growth of pits at constant potential, Journal of the Electrochemical Societ. 132(8) (1985) 1796. DOI 10.1149/1.2114220

[22]   D. E. Williams, C. Westcott, M. Fleischmann, Stochastic models of pitting corrosion of stainless steels: II Measurement and interpretation of data at constant potential, Journal of the Electrochemical Society, 132 (1985) 1804. DOI 10.1149/1.2114221

[23]   P. C. Pistorius, G. T. Burstein, Growth of corrosion pits on stainless steel in chloride solution containing dilute sulphate, Corrosion sci. 33(1992) 1885-1897. https://doi.org/10.1016/0010-938X(92)90191-5

[24]   P. Forchhammer, H. J. Engell, Untersuchungen über den Lochfraß an passiven austenitischen Chrom-Nickel-Stählen in neutralen Chloridlösungen, Materials and Corr. 20 (1969) 1-12. https://doi.org/10.1002/maco.19690200103

[25]   G. S. Eklund, Initiation of pitting at sulfide inclusions in stainless steel, Journal of the Electrochemical Societ. 121 (1974) 467. DOI 10.1149/1.2401840

[26]   L. Stockert, H. Boehni, H. Susceptibility to crevice corrosion and metastable pitting of stainless steels, In Materials Science Foru. 44 (1989) 313-328. https://doi.org/10.4028/www.scientific.net/MSF.44-45.313

[27] W. Tian, N. Du, S. Li, S. Chen, Q. Wu, Metastable pitting corrosion of 304 stainless steel in 3.5% NaCl solution, Corrosion Sci. 85 (2014) 372-379. https://doi.org/10.1016/j.corsci.2014.04.033

[28] H.S. Isaacs, The localized breakdown and repair of passive surfaces during pitting, Corrosion Sci. 29 (1989) 313-323. https://doi.org/10.1016/0010-938X(89)90038-3

[29] P. C. Pistorius, G. T. Burstein, Metastable pitting corrosion of stainless steel and the transition to stability, Philosophical transactions of the royal society of London. Series A: Physical and Engineering Sci. 341(1992) 531-559. https://doi.org/10.1098/rsta.1992.0114

[30] G. T. Burstein, P.C. Pistorius, S.P. Mattin, The nucleation and growth of corrosion pits on stainless steel, Corrosion Sci. 35 (1993) 57-62. https://doi.org/10.1016/0010-938X(93)90133-2

[31] S. Nasrazadani, H. Vaughan, D. Ellerbrock, C. Martin-Callizo, Development of a new accelerated corrosion test for all-aluminum microchannel and tube and fin heat exchangers—part II: chamber study, ASHRAE Transact. 126 (2020) 572-580.

[32] P. R. Roberge, Handbook of corrosion engineering, McGraw-Hill (2019).

[33] R. G. Kelly, Crevice corrosion, Encyclopedia of Electrochemistry, 4 (2003) 275. https://doi.org/10.31399/asm.hb.v13a.a0003613

[34] J. T. Burns, J. M. Larsen, R. P. Gangloff, Driving forces for localized corrosion-to-fatigue crack transition in Al-Zn-Mg-Cu, Fatigue & Fracture of Engineering Materials & Struct. 34.10 (2011) 745-773. https://doi.org/10.1111/j.1460-2695.2011.01568.x

[35] N. Birbilis, M. K. Cavanaugh, R. G. Buchheit, Electrochemical behavior and localized corrosion associated with al"7cu"2fe particles in aluminum alloy 7075-T651, Corrosion Sci. 48.12 (2006) 4202-4215. https://doi.org/10.1016/j.corsci.2006.02.007

[36] G. Grundmeier, W. Schmidt, M. J. E. A. Stratmann, Corrosion protection by organic coatings: electrochemical mechanism and novel methods of investigation, Electrochimica Act. 45 (2000) 2515-2533. https://doi.org/10.1016/S0013-4686(00)00348-0

[37] P. Campestrini, G. Goeminne, H. Terryn, J. Vereecken, J. H. W. De Wit, Chromate conversion coating on aluminum alloys I formation mechanism, Journal-Electrochemical Societ. 151 (2004) B59. DOI 10.1149/1.1637355

[38] Q. Meng, G. S. Frankel, Characterization of chromate conversion coating on AA7075-T6 aluminum alloy, Surface and Interface Anal. 36.1 (2004) 30-42. https://doi.org/10.1002/sia.1643

[39] H.S. Isaacs, K. Sasaki, C. S. Jeffcoate, V. Laget, R. Buchheit, Formation of chromate conversion coatings on aluminum and its alloys, Journal of The Electrochemical Societ. 152.11 (2005) B441. DOI 10.1149/1.2041027

[40]   P. Campestrini, H. Terryn, J. Vereecken, J. H. W. De Wit, Chromate Conversion coating on aluminum alloys III corrosion protection, Journal-Electrochemical Societ. 151.6 (2004) B370. DOI 10.1149/1.1736683

[41]   R. W. Revie, Corrosion and corrosion control: an introduction to corrosion science and engineer, (2008).

[42]   V. E. Carter, Metallic coatings for corrosion control: corrosion control series. No. 1. Newnes, (2013).

[43]   J. Y. Chang, J. Y., S. M. You, Enhanced boiling heat transfer from microporous surfaces: effects of a coating composition and method, International Journal of Heat and Mass Transf. 40 (1997) 4449-4460. https://doi.org/10.1016/S0017-9310(97)00057-4

[44]   L. Fedrizzi, F. Andreatta, L. Paussa, F. Deflorian, S. Maschio, Heat exchangers corrosion protection by using organic coatings, Progr Org Coat. 63 (2008) 299–306. https://doi.org/10.1016/j.porgcoat.2008.01.009

[45]   K. I. M. Jong-Soon, K. A. N. G. Tae-Ho, K. I. M. In-Kwan, Surface treatment to improve corrosion resistance of Al plate heat exchangers, Trans Nonferrous Metals Soc China. 19 (2009) 28–31. https://doi.org/10.1016/S1003-6326(10)60240-3

[46]   C. C. Wang, C. T. Chang, Heat and mass transfer for plate fin-and-tube heat exchangers, with and without hydrophilic coating, International Journal of Heat Mass Transf. 41 (1998) 3109–3120. https://doi.org/10.1016/S0017-9310(98)00060-X

[47]   K. Hong, R. L. Webb, Wetting coatings for dehumidifying heat exchangers, HVAC&R Res. 6 (2000) 229–242.

[48]   V. S. Sinyavskii, V. V. Ulanova, V. D. Kalinin, On the mechanism of intergranular corrosion of aluminum alloys, Protection of metal. 40 (2004) 481-490.

[49]   T. Minoda, H. Yoshida, Effect of grain boundary characteristics on intergranular corrosion resistance of 6061 aluminum alloy extrusion, Metallurgical and Materials Transactions A. 33 (2002) 2891-2898.

[50]   S. H. Kim, U. Erb, K. T. Aust, G. Palumbo, Grain boundary character distribution and intergranular corrosion behavior in high purity aluminum, Scripta materia. 44 (2001) 835-839. https://doi.org/10.1016/S1359-6462(00)00682-5

[51]   D. Ifezue, F. H. Tobins, Corrosion failure of aluminum heat exchanger tubes, Journal of Failure Analysis and Prevent. 15 (2015) 541-547.

[52]   R. H. Brown, W. L. Fink, M. S. Hunter, Measurement of irreversible potentials as a metallurgical research tool. J. Trans. AIME 143 (1941) 115-122

[53]   Galvele, J.R. and de De Micheli, S.M., 1970. Mechanism of intergranular corrosion of Al-Cu alloys. Corrosion sci. 10(11), pp.795-807.

[54]   R. G. Buchheit, J. P. Moran, G. E. Stoner, Electrochemical behavior of the T1 (Al2CuLi) intermetallic compound and its role in localized corrosion of Al-2% Li-3% Cu alloys, Corr. 50 (1994) 120-130. https://doi.org/10.5006/1.3293500

[55]   K. Kowal, J. DeLuccia, J. Y. Josefowicz, C. Laird, A. G. Farrington, A.G., In situ atomic force microscopy observations of the corrosion behavior of aluminum-copper alloys, Journal of The Electrochemical Societ. 143 (1996) 2471. DOI 10.1149/1.1837033

[56]   H. G. Hedrick, Reviews: microbiologically influenced corrosion, Materials Protect. 9 (1970) 27-30.

[57]   A. F. Giacobone, S. A. Rodriguez, A. L. Burkart, R. A. Pizarro, R.A., Microbiological induced corrosion of AA 6061 nuclear alloy in highly diluted media by Bacillus cereus RE 10, International Biodeterioration & Biodegradat. 65 (2011) 1161-1168. https://doi.org/10.1016/j.ibiod.2011.08.012

[58]   J. S. de Andrade, M. R. S. Vieira, S. H. Oliveira, S. K. de Melo Santos, S. L. Urtiga Filho, Study of microbiologically induced corrosion of 5052 aluminum alloy by sulfate-reducing bacteria in seawater. Materials Chemistry and Phys. 241 (2020) 122296. https://doi.org/10.1016/j.matchemphys.2019.122296

[59]   S. S. Yang, J. Y. Lin, Y. T. Lin, Microbiologically induced corrosion of aluminum alloys in fuel-oil/aqueous system, Journal of Microbiology, Immunology, and Infection= Wei Mian yu gan ran za zhi. 31(1998) 151-164.

[60]   V. V. Nelson, O. T. Maria, S. V. Mamiè, P. C. Maritza, P.C., Microbiologically influenced corrosion in aluminium alloys 7075 and 2024, In Aluminium Alloys-Recent Trends in Processing, Characterization, Mechanical Behavior and Applica. IntechOpen (2017). DOI: 10.5772/intechopen.70735

[61]   P. X. Jiang, M. H. Fan, G. S. Si, Z. P. Ren, Thermal-hydraulic performance of small scale microchannel and porous-media heat exchangers, International Journal of Heat and Mass Transf. 44 (2001) 1039-1051. https://doi.org/10.1016/S0017-9310(00)00169-1

[62]   H. Al-bakhit, A. Fakheri, A hybrid approach for full numerical simulation of heat exchangers, In Heat Transfer Summer Confer. 47322 (2005) 839-846. https://doi.org/10.1115/HT2005-72745

[63]   H. Al-bakhit, A. Fakheri, Numerical simulation of heat transfer in simultaneously developing flows in parallel rectangular ducts, Applied Thermal Engineer. 26 (2006) 596-603. https://doi.org/10.1016/j.applthermaleng.2005.07.002

[64]   J. J. Brandner, E. Anurjew, L. Buhn, E. Hansjosten, T. Henning, U. Schygulla, A. Wenka, K. Schubert, Concept and realization of microstructure heat exchangers for enhanced heat transfer, Experimental Thermal and Fluid Science 30 (2006) 801–809.

[65]   M. I. Hasan, A. A. Rageb, M. Yaghoubi, H. Homayoni, Influence of channel geometry on the performance of a counter flow microchannel heat exchanger, International Journal of Thermal Sci. 48, no. 8 (2009): 1607-1618. https://doi.org/10.1016/j.ijthermalsci.2009.01.004

[66]   V. Glazar, B. Frankovic, A. Trp, Experimental and numerical study of the compact heat exchanger with different microchannel shapes, International Journal of Refrigerat. 51 (2015) 144-153. https://doi.org/10.1016/j.ijrefrig.2014.06.017

[67]   V. Glazar, A. Trp, K. Lenic, Optimization of air-water microchannel heat exchanger using response surface methodology, International Journal of Heat and Mass Transf. 157 (2020) 119887. https://doi.org/10.1016/j.ijheatmasstransfer.2020.119887

[68]   M. M. Lachowicz, M. B. Lachowicz, A. Gertruda, Role of microstructure in corrosion of microchannel heat exchangers, In˙zynieria Mater. Mater. Eng. 39 (2018) 94–99. DOI 0.15199/28.2018.3.1

[69]   L. Guo, J. Wang, W. Hu, D. Zhou, Corrosion process of multilayer aluminum brazed sheet by EIS and EN techniques, Surf. Rev. Lett. 26 (2018) 1850224. https://doi.org/10.1142/S0218625X18502037

[70]   Z. Yuan, F. Tao, J. Wen, Y. Tu, The dependence of microstructural evolution and corrosion resistance of a sandwich multi-layers brazing sheets on the homogenization annealing, IEEE Acc. 7 (2019) 121388–121394.

[71]   G. J. Marshall, R. K. Bolingbroke, A. Gray, Microstructural control in an aluminum core alloy for brazing sheet applications. Metall. Mater. Trans. A 24 (1993) 1935–1942.

[72]   Z. Yuan, Y. Tu, H. He, T. Yuan, Q. Zhang, X. Peng, Influence of final annealing temperature on the microstructural evolution and corrosion resistance of a Sandwich multi-layered aluminum sheet, Mater. Res. Expr. 6 (2019) 026536.

[73]   Y. S. Kim, I. J. Park, J. G. Kim, Simulation approach for cathodic protection prediction of aluminum fin-tube heat exchanger using boundary element method. Metal. 9 (2019) 376. https://doi.org/10.3390/met9030376

[74]   M. Ali, A. Ul-Hamid, L. M. Alhems, A. Saeed, Review of common failures in heat exchangers—Part I: Mechanical and elevated temperature failures. Eng. Fail. Anal. 109 (2020) 104396. https://doi.org/10.1016/j.engfailanal.2020.104396

[75]   W. Faes, S. Lecompte, Z. Ahmed, J. Van Bael, R. Salenbien, K. Verbeken, M. De Paepe, Corrosion and corrosion prevention in heat exchangers, Corrosion Rev. 37 (2019) 131–155. https://doi.org/10.1515/corrrev-2018-0054

[76]   M. Yoshino, S. Iwao, M. Edo, H. Chiba, Mechanism of intergranular corrosion of brazed Al–Mn–Cu alloys with various Si content, J. Jpn. Inst. Light Met. 67 (2017) 234–241. https://doi.org/10.2320/matertrans.L-M2017808

[77]   C. M. Liao, J. M. Olive, M. Gao, R. P. Wei, In-situ monitoring of pitting corrosion in aluminum alloy 2024, Corrosion 54 (1998): 451-458.

[78]   A. S. Mujumdar, Heat Exchanger Design Handbook, Drying Technol. 18 (2000) 2167-2168. https://doi.org/10.1080/07373930008917833

[79]   R. Baboian, Corrosion tests and standards: application and interpretation, Baltimore M D: ASTM (2005).

[80]   M. Poelman, M. Olivier, N. Gayarre, J. Petitjean, Electrochemical study of different ageing tests for the evaluation of a cataphoretic epoxy primer on aluminum, Progress in Organic coat. 54 (2005) 55-62. https://doi.org/10.1016/j.porgcoat.2005.04.004

[81]   R. G. Hu, S. Zhang, J. F. Bu, C. J. Lin, G. L. Song, Recent progress in corrosion protection of magnesium alloys by organic coatings, Progress in Organic coat. 73 (2012) 129-141. https://doi.org/10.1016/j.porgcoat.2011.10.011

[82]   F. Mansfeld, A correlation between salt spray and electrochemical impedance spectroscopy test results for conversion-coated aluminum alloys, Corrosion sci. 54 (1998) 595 -597. https://doi.org/10.5006/1.3284829

[83]   S. Vantadori, A. Carpinteri, V. Di Cocco, G. Fortese, F. Iacoviello, S. Natali, S., A. Zanichelli, Novel zinc-based alloys used to improve the corrosion protection of metallic substrates, Engineering Failure Analy. 82 (2017) 327-339. https://doi.org/10.1016/j.engfailanal.2017.05.043

[84]   F. Mansfeld, J. V. Kenkel, Laboratory studies of galvanic corrosion of aluminium alloys, galvanic and pitting corrosion—field and laboratory Studies, ASTM STP   576 (1976) 20-47.

[85]   X. G. Zhang, Corrosion and electrochemistry of zinc, Springer Science & Business Media (1996).

[86]   D. P. Schmidt, B. A. Shaw, E. Sikora, W. W. Shaw, L. H. Laliberte, Corrosion protection assessment of sacrificial coating systems as a function of exposure time in a marine environment, Progress in Organic Coat. 57 (2006) 352-364. https://doi.org/10.1016/j.porgcoat.2006.09.021

[87]   M. E. McMahon, R. J. Santucci Jr, C. F. Glover, B. Kannan, Z. R. Walsh, J. R. Scully, A review of modern assessment methods for metal and metal-oxide based primers for substrate corrosion protection, Frontiers in Material. 6 (2019) 190. https://doi.org/10.3389/fmats.2019.00190

[88]   F. Chang, M. Levy, B. Jackman, W. B. Nowak, Assessment of corrosion   resistant coatings for a depleted U-0.75 Ti alloy, Surface and Coatings Technol. 39 (1989) 721-731. https://doi.org/10.1016/S0257-8972(89)80034-9

[89]   M. Mouanga, P. Berçot, Comparison of corrosion behaviour of zinc in NaCl and in NaOH solutions; Part II: electrochemical analyses, Corrosion Sci. 52 (2010) 3993-4000. https://doi.org/10.1016/j.corsci.2010.08.003

[90]   K. Al-Muhanna, K. Habib, Corrosion behavior of different alloys exposed to continuous flowing seawater by electrochemical impedance spectroscopy (EIS). Desalinat. 250 (2010) 404-407. https://doi.org/10.1016/j.desal.2009.09.065

[91]   M. Vázquez-Nambo, J. A. Gutiérrez-Gnecchi, E. Reyes-Archundia, W. Yang, M. A. Rodriguez-Frias, J. C. Olivares-Rojas, D. Lorias-Espinoza, Experimental study of electrical properties of pharmaceutical materials by electrical impedance spectroscopy, Applied Sci. 10 (2020) 6576. https://doi.org/10.3390/app10186576

[92]   V. F. Lvovich, Electrochemical impedance spectroscopy (EIS) applications to sensors and diagnostics, In Encyclopedia of Applied Electrochem. (2014) 485–507.

[93]   H. S. Magar, R. Y. Hassan, A. Mulchandani, Electrochemical impedance spectroscopy (EIS): Principles, construction, and biosensing applications, Sensor. 21 (2021) 6578. https://doi.org/10.3390/s21196578

[94]   M. Carminati, G. Ferrari, D. Bianchi, M. Sampietro, Impedance spectroscopy for biosensing: circuits and applications, In Handbook of Biochips: Integrated Circuits and Systems for Biology and Medicine, Springer: New York, NY, USA (2015) 1–24.

[95]   R. A. Cottis, S. Turgoose, R. Neuman, Corrosion testing made easy: impedance and noise analy. 2 (1999) 9-39.

[96]   M. E. Orazem, B. Tribollet, Electrochemical impedance spectroscopy, The Electrochemical Society Series, ed. ECS. 9 (2008) 155.

[97]   R. Hirayama, S. Haruyama, Electrochemical impedance for degraded coated steel having pores, Corr. 47 (1991) 952-958. https://doi.org/10.5006/1.3585208

[98]   E. P. M. V. Westing, G.M. Ferrari, J.H.D. Wit, The determination of coating performance with impedance measurements - III in situ determination of loss of adhesion, Corrosion Sci. 36 (1994) 979-994. https://doi.org/10.1016/0010-938X(94)90198-8

[99]   P. L. Bonora, F. Deflorian, L. Fedrizzi, Electrochemical impedance spectroscopy as a tool for investigating underpaint corrosion, Electrochemical Acta. 41 (1996) 1073-1082. https://doi.org/10.1016/0013-4686(95)00440-8

[100]   F. Gambina, Corrosion resistance characterization of coating systems used to protect aluminum alloys using electrochemical impedance spectroscopy and artificial neural networks, Diss. The Ohio State University, (2010).

[101]   C. H. Hsu, F. Mansfeld, Technical note: concerning the conversion of the constant phase element parameter Y0 into a capacitance. Corr. 57 (2001) 747-748.

[102]   G. J. Brug, The analysis of electrode impedance complicated by the presence of a constant phase element, Journal of Electroanalytical Chem.176 (1984) 275-295. https://doi.org/10.1016/S0022-0728(84)80324-1

[103]   D. E. Jones, Principles and prevention of corrosion, Second edition. Upper Saddle River, New Jersey, United states of America. Prentice hall (1996).

[104]   S. Lillard, Corrosion and compatibility, Comprehensive Nuclear Materials. Amsterdam, Netherlands: Elsevier Science. (2012). DOI: 10.1016/B978-0-08-056033-5.00024-0

[105]   M. Dorreyatim, Cyclic Polarization of AA 3102 in Corrosive Electrolytes Containing Sodium Chloride and Ammonium Sulfate, (2016).

[106]   H. Lomax, T. H. Pullium, D. W. Zingg, Fundamentals of computational fluid dynamics", Handbook, August 26 (1999).

[107] T. Petrila, D. Trif, Basics of fluid mechanics and introduction to computational fluid dynamics, Springer, (2004).

[108] Fluent, A. N. S. Y. S. "Ansys fluent theory guide." Ansys Inc., USA 15317 (2021).

[109] L. Li, Study of corrosion and corrosion inhibition of chromate and chromate-free primers, Electronic Thesis or Dissertation. Ohio State University, (2012)

[110] O. A. Lopez-Garrity, Corrosion inhibition mechanisms of aluminum alloy 2024-T3 by selected non-chromate inhibitors, (2013).

[111] S. Nasrazadani, Development of new accelerated corrosion test(s) for all-aluminum microchannel and tube and fin heat exchangers—part I: comprehensive literature review, ASHRAE Transact. 126 (2020) 870-882.

[112] G. Bierwagen, R. Brown, D. Battocchi, S. Hayes, Active metal-based corrosion protective coating systems for aircraft requiring no-chromate pretreatment, Progress in Organic Coat. 67 (2010) 195-208. https://doi.org/10.1016/j.porgcoat.2009.10.009

[113] D. P. Schmidt, B. A. Shaw, E. Sikora, W. W. Shaw, L. H. Laliberte, Corrosion protection assessment of sacrificial coating systems as a function of exposure time in a marine environment, Progress in Organic Coatings 57 (2006) 352-364. https://doi.org/10.1016/j.porgcoat.2006.09.021

[114] M. E. McMahon, R. J. Santucci Jr, C. F. Glover, B. Kannan, Z. R. Walsh, J. R. Scully, A review of modern assessment methods for metal and metal-oxide based primers for substrate corrosion protection, Frontiers in Materials 6 (2019) 190. https://doi.org/10.3389/fmats.2019.00190

[115] F. Chang, M. Levy, B. Jackman, W. B. Nowak, (1989). Assessment of corrosion resistant coatings for a depleted U-0.75 Ti alloy, Surface and Coatings Technol. 39 (1989) 721-731. https://doi.org/10.1016/S0257-8972(89)80034-9

[116] M. Mouanga, P. Berçot, Comparison of corrosion behaviour of zinc in NaCl and in NaOH solutions; Part II: Electrochemical analyses, Corrosion Sci. 52 (2010) 3993-4000. https://doi.org/10.1016/j.corsci.2010.08.018

[117] K. Al-Muhanna, K. Habib, Corrosion behavior of different alloys exposed to continuous flowing seawater by electrochemical impedance spectroscopy (EIS), Desalinat. 250 (2010) 404-407. https://doi.org/10.1016/j.desal.2009.09.065

[118] A. Davoodi, J. Pan, C. Leygraf, S. Norgren, Integrated AFM and SECM for in situ studies of localized corrosion of Al alloys, Electrochimica Acta. 52 (2007) 7697–7705. https://doi.org/10.1016/j.electacta.2006.12.073

[119] S. Nasrazadani, H. Vaughan, D. Ellerbrock, C. Martin-Callizo, Development of a new accelerated corrosion test for all-aluminum microchannel and tube and fin heat exchangers—part II: chamber study, ASHRAE Transact. 126 (2020).